[UCI]I804:24011-200000292872

2020년 2월
박사학위논문

In-situ 추진제 생산 및 금속 연료 점화 기술 개발

조선대학교 대학원

항공우주공학과

박 길 수

In-situ 추진제 생산 및 금속 연료 점화 기술 개발

- Development of In-situ Propellant Production and Metal Fuel Ignition Technology -

2019년 12 월 27 일

조 선 대 학 교 대 학 원

항 공 우 주 공 학 과

박 길 수

In-situ 추진제 생산 및 금속 연료 점화 기술 개발

지도교수 김 태 규

이 논문을 공학 박사학위신청 논문으로 제출함.

2019 년 12 월

조 선 대 학 교 대 학 원

항 공 우 주 공 학 과

박 길 수

박길수의 박사학위 논문을 인준함

위원장	한국기계연구원 책임연구원	이 대 훈	인
위원	조선대학교 교수	이 현 재	인
위원	조선대학교 교수	이 창 열	인
위원	조선대학교 교수	김 태 규	인
위원	한국기계연구원 선임연구원	조 성 권	인

2019 년 12 월

조 선 대 학 교 대 학 원

CONTENTS

LIST OF FIGURES

LIST OF TABLES

NOMENCLATURE

Al	Aluminum
Ar	Argon
BET	Brunauer-Emmiett-teller
CaO	Calcium oxide
Ce	Cerium
CO	Carbon monoxide
CO_2	Carbon dioxide
d	distance of discharge gap
DBD	Dielectric barrier discharge
DRIFTS	Diffuse reflectance infrared Fourier transform spectroscopy
E	Electric field
EDL	Entry, descent, landing
FTIR	Fourier transform infrared spectroscopy
GA	Gliding arc
H_2	Hydrogen
He	Helium
Isp	Specific impulse
ISPP	In-situ propellant production
MAV	Mars ascent vehicle
Mg	Magnesium
MSR	Mars sample return
MW	Microwave
$NaBH_4$	Sodium borohydride
n_e	Number density
NTP	Non-thermal plasma
O_2	Oxygen
p	Pressure
SEI	Specific energy input

SRL	Sample retrieval and launch
SRO	Sample return orbiter
T_e	Electron temperature
T_d	Townsend
T_i	Ion temperature
T_r	Rotational temperature
T_v	Vibrational temperature
T_0	Particle temperature
TPD	Temperature programmed desorption
V_b	Breakdown voltage
X_{CO_2}	CO_2 conversion
XRD	X-ray diffraction
ZnSe	Zinc Selenide

ABSTRACT

Development of in-situ propellant production and Metal Fuel Ignition Technology

Park Kil Su
Advisor : Prof. Kim Tae-gyu, Ph.D.
Department of Aerospace Engineering
Graduate School of Chosun University

화성은 태양계의 4번째 행성으로 생명체 생존 가능성이 제기되면서 태양계에서 인류의 가장 많은 관심을 받고 있는 행성이다. 1960년 소련에서 인류의 첫 화성 탐사선 Mars 1M을 발사했지만 대기권에서 산화되어 실패했다. 소련의 실패 이후 1965년 미국의 Mariner 4호가 인류 최초로 화성에 접근해 화성 표면을 촬영하여 지구로 보내왔다. 이후 미국과 소련은 경쟁적으로 화성 탐사선을 발사했으며, 최근에는 미국, 러시아, 유럽 등의 국가에서 화성으로 탐사선을 보내 화성의 대기 및 지질 정보를 지구로 보내왔다. 지금까지의 화성 탐사는 로버를 이용해 원격으로 탐사가 이루어져 왔지만 다음 단계의 화성 탐사는 보다 정확한 분석을 위해 화성의 샘플을 지구로 가져오는 MSR (Mars sample return) 임무의 필요성이 제기되고 있다. 하지만 화성 표면에서 지질 샘플을 지구로 반환하려면 화성의 중력을 벗어나기 위한 높은 추력의 추진 시스템이 필요하다. 결과적으로 상당한 양의 추진제가 필요하게 된다. 기술적으로 지구에서 화성으로 돌아오기 위한 모든 추진제를 가져오는 것은 비현실적이고 비효율적이다. 이에 화성에서 추진제를 생산하는 In-situ 추진제 생산 (ISPP) 기술이 관심을 받으면서 NASA 등에서 활발한 연구가 진행되고 있다. 지금까지 화성탐사를 통해 얻은 정보에 따르면 화성은 대기의 95%가 이산화탄소 (CO_2)로 이루어져 있다. 이산화탄소를 분해해 일산화탄소 (CO)와 산소 (O_2)를 얻을 수 있다. O_2는 연소에 필요한 산화제로 사용할 수 있으며, CO는 추진제 및 연료로 사용 가능하다. 또한 화성의 토양에는 5±2.5%의 마그네슘

(Mg)과 3.0±0.9%의 알루미늄(Al)이 함유되어 있다. 마그네슘과 알루미늄은 금속 추진제로 높은 비추력을 가지고 있어 비추력을 높이기 위한 첨가제로 많이 사용되고 있다. 특히 알루미늄은 15.485kJ/g의 높은 에너지 밀도를 가지고 있으며, 무독성 연료 생성물로 화성 상승선 (Mars ascent vehicle, MSR)의 연료로 사용하게 적합하다. 본 연구에서는 이러한 화성의 자원을 활용하여 현장에서 추진제 생산을 위한 기술에 대해서 다음과 같은 연구를 수행하였다.

첫 번째로 플라즈마와 산화칼슘 (CaO)을 이용한 이산화탄소 포집에 관한 연구를 수행하였다. 산화칼슘을 이용한 Calcium looping (CaL) 공정은 재생 가능한 특성으로 저비용으로 운용 가능해 CO_2 포집을 위한 우수한 흡착제로 주목받고 있다. 하지만 일반적인 CaL 공정은 650℃에서 CO_2가 흡착되고 역반응은 950℃ 이상의 높은 온도에서 수행되기 때문에 에너지 효율의 문제는 개선되어야 하는 단점이 있다. 이를 해결하기 위해 본 연구에서는 플라즈마를 이용해 CO_2 흡착률을 높이는 연구를 수행하였다. 플라즈마 여기된 CO_2는 CaO 표면에 훨씬 더 흡착이 잘 되는 것을 확인하였으며, 플라즈마 여기된 CO_2와 CaO 표면에서의 흡착 메커니즘 및 특성을 XRD, TPD 그리고 in-situ DRIFTS 분광법을 통해 규명하였다.

두 번째로는 저장된 CO_2를 자원으로 활용하기 위해 CO_2를 CO와 O_2로 분해하는 연구를 수행하였다. CO_2는 매운 안정적인 분자이기 때문에 2000℃ 이상의 온도에서 분해된다. 최근에는 높은 에너지 효율을 위해 플라즈마를 활용한 CO_2 분해 연구가 진행되고 있다. 플라즈마는 적은 에너지로 고온의 에너지를 발생하며, 화학적으로 활성화시켜 반응성을 높일 수 있다. 특히 플라즈마와 촉매를 결합하면 여러 시너지 효과를 기대 할 수 있어 전환율과 에너지 효율을 상당히 개선할 수 있다. 하지만 이러한 성능 향상의 원인과 정확한 메커니즘은 아직까지 명확하게 밝혀지지 않고 있다. 본 연구에서는 Al_2O_3와 Ce/Al_2O_3 촉매가 CO_2 전환율 및 에너지 효율에 미치는 영향을 분석하였다. 또한 in-situ DRIFTS 분광법을 이용해 플라즈마 여기된 CO_2가 촉매 표면에서 어떠한 작용이 일어나는지에 대한 분석을 수행하여 촉매가 결합된 플라즈마에서 CO_2 분해 메커니즘을 분석하였다.

마지막으로 화성 토양의 3% 이상을 차지하고 있는 알루미늄을 화성 상승선의 연료

로 사용하기 위한 금속 연료 점화 시스템에 관한 연구를 수행하였다. 알루미늄은 산화피막인 알루미나로 둘러 싸여있는데, 이 산화피막은 2200℃ 이상의 온도에서 용융되기 시작한다. 알루미늄 산화피막의 높은 용융점으로 인해 초기 점화를 위해 많은 에너지를 필요로 하고, 이로 인해 전체 추진 시스템의 효율이 떨어지게 된다. 본 연구에서는 고체 화학수소화물인 $NaBH_4$를 이용한 자동 수소점화 시스템을 설계하였다. $NaBH_4$는 500℃에서 열분해 되어 수소를 발생하며, 이 때 발생한 수소는 NaBH4의 열분해 온도에 의해 자동 발화된다. 수소 화염의 온도는 3200℃ 이상으로 알루미늄을 점화하기에 충분히 높은 온도이다. 산화제 공급 유량에 따른 $NaBH_4$ 열분해 특성을 분석하였으며, $NaBH_4$ 열분해 부산물의 가수분해 실험을 통해 분해율을 분석하였다. 30g의 $NaBH_4$는 최대 110초간 수소 화염을 발생시켰다. 또한, $NaBH_4$ 자동 수소 점화 시스템으로 알루미늄 점화 실험을 통해 성능을 검증하였으며, 광검출기를 이용해 알루미늄 연소 시 가장 지배적으로 발생하는 AlO가 검출을 통해 알루미늄이 점화되었음을 확인했다.

Ⅰ. Introduction

1.1 Motivation

Mars has long been the subject of human concern as the most Earth-like planet in the solar system. A lot of research on Mars, the fourth planet in the solar system, has been performed in the United States, Russia, China, Japan, and Europe to explore Mars. The first attempt of the Mars exploration mission was tried by the Soviet Union in 1960. The Mars 1M to explore Mars was launched in 1960, but the mission was failed due to the destruction at the launch [1]. After the first launch, the Soviet Union launched eight probes for the exploration of Mars between 1960 and 1969. However, they all failed [1].

NASA's Mariner 3 was launched on November 5, 1964, but the mission was failed due to the unopened shroud encasing the spacecraft atop of its rocket [2, 3]. The first success of reaching Mars was achieved by Mariner 4 launched on November 28, 1964. Mariner 4 provided the first close-up photographs of Mars (Fig. 1) [4, 5].

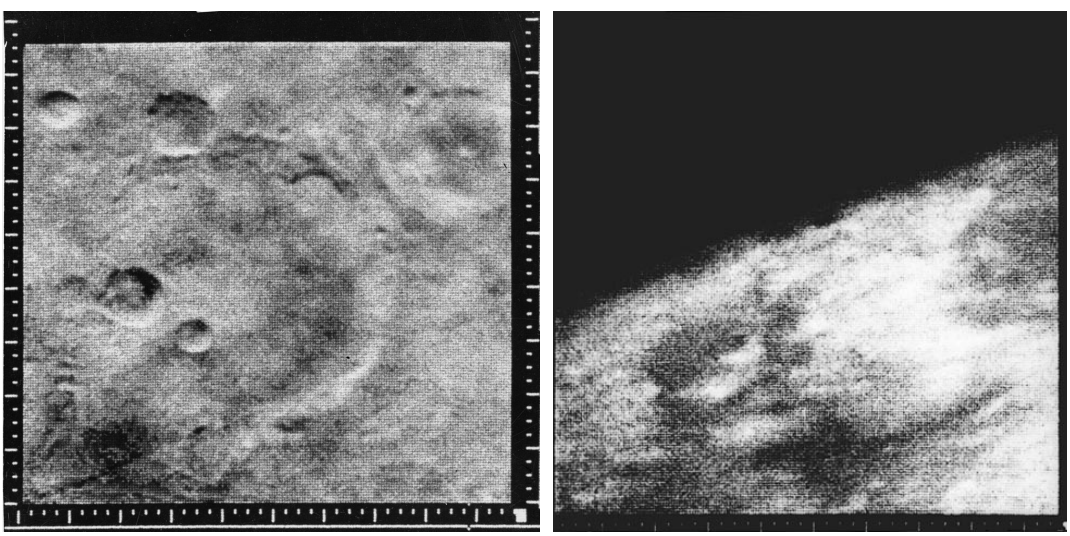

Fig. 1 The first close-up images taken of Mars in 1965 from Mariner 4.

The pictures showed impact craters and provided data about the planet, by which a surface atmospheric pressure of about 1% of Earth's and daytime temperatures of −100°C

were estimated [3, 4]. The received data from Mariner 4 implied that it is difficult surviving there than previously anticipated, so the planned Martian landers should be redesigned.

NASA has continued the Mariner program, and they were successful to send a Mariner 6 and 7 to Mars in 1969 [6, 7]. After the failure of Mariner 8 due to a launch vehicle problem, Mariner 9 was successfully launched on May 30, 1971, becoming the first spacecraft to enter the orbit of Mars [8, 9]. During the 349 days in orbit, Mariner 9 sent 73,249 images to Earth, accounting for 85% of the surface of Mars such as river beds, craters, massive extinct volcanoes, canyons, evidence of wind and water erosion and deposition, weather fronts, fogs, and more [9]. The result of the Mariner 9 mission underpinned the Viking program. The Viking 1 and Viking 2 which were launched in 1975 were the first spacecraft to land and operate on Mars successfully [10, 11].

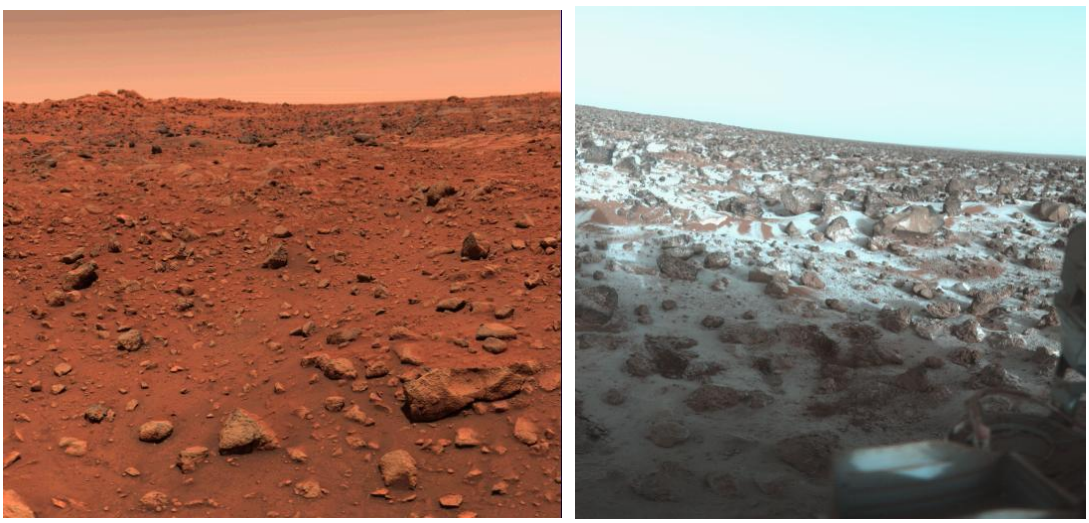

Fig. 2 Viking 1 lander site (left) and frost at Viking 2 site (right) [11].

The Mars Pathfinder was the first spacecraft to land on Mars in 20 years since the Viking program in 1976 and was landed Mars Ares Vallis on December 4, 1996 [12, 13]. Pathfinder included the first-ever robotic rover Sojourner for analysis of Martian soil. It had an Alpha Proton X-ray Spectrometer (APXS), which was used to investigate the components of the soil and rocks. In addition, the Sojourner including the two black and

white cameras and a color one could investigate the geology of the Martian surface, magnetic properties of the dust, the geochemistry and evolutionary history of the rocks and surface, atmosphere and the rotational and orbital dynamics [13]. Sojourner sent over 500 images of the Mars topography to Earth and analyzed 16 samples of rocks. Most of the artifacts Ares Vallis, the landing site of the Pathfinder, were found to be volcanic [14]. Above all, a rock named Yogi, given by its smooth surface, suggested the past existence of water in the region. The Fig. 3 shows Sojourner rover on Mars on sol 22 and Sojourner rover taking Yogi's Alpha Proton X-ray Spectrometer measurement.

Fig. 3 Sojourner rover on Mars on sol 22 (left) and Sojourner rover taking Yogi's Alpha Proton X-ray Spectrometer measurement (right) [14].

The NASA's twin Mars exploration rovers named Spirit (MER-A) and Opportunity (MER-B), landed on Mars on January 2004, also sent images which confidence of the water existence [15-18]. These two rovers have exceeded their mission duration. Notably, the Opportunity had continued exploration activities for 15 years until the communication failure by a dust storm. NASA's rover, landed on August 6, 2012, was bigger than Opportunity rovers, mounted a nuclear battery, not a solar battery [19]. Therefore, unlike conventional rovers equipped with solar cells, it could operate for a long time even when

there is no sunlight due to sandstorms. The communication with Opportunity has been cut off since June 10, 2018, due to an encircling dust storm on Mars. NASA was reported to the end of the rover mission on Feb. 13, 2019 [20, 21].

NASA's Curiosity landed on Aeolis Palus inside Gale on Mars on August 6, 2012, is continually sending an important investigation data as Martian climate, geology, environmental conditions favorable for microbial life and investigation of the role of water [22]. Also, Curiosity detected methane (CH_4) in the atmosphere of Mars. It is one of Curiosity's most notable discoveries about the possible presence of life on Mars in the past [22, 23].

The InSight, the eighth U.S. spacecraft which landed on Mars on May 5, 2018, is performing a different mission than previous ones [24, 25]. Previous Mars rovers had the main task of examining the atmosphere and surface of Mars and finding traces of life, but the InSight aims to explore inside, including the planet's lipids. The InSight does not move but performs exploration at the point where it lands. Using a robotic arm mounted on its main body, it sets up a seismograph and penetrates the Martian's surface to measure the rate of heat flow from the interior, estimate the size of Mars'core and whether the core is liquid or solid [25].

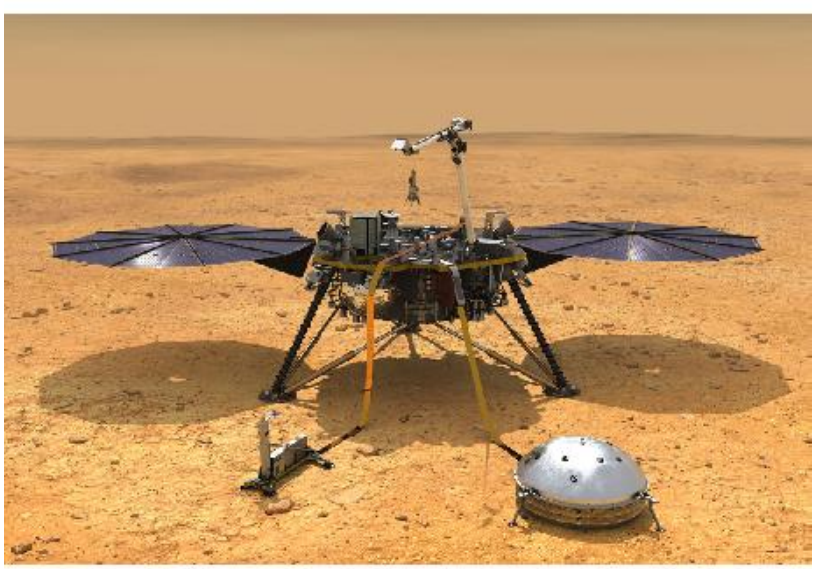

Fig. 4 NASA's InSight [24].

1.2 Aim of research

Until now, all Mars investigation had been performed remotely using the unmanned reconnaissance robots because the propellant could not been loaded for return to Earth. Until now, the next step of Mars exploration is to bring samples to Earth for a particular analysis. If the next Mars investigation is performed by the two-way mission, it will enable tremendous scientific discoveries.

Mars Sample Return (MSR) campaign is performed by three missions as illustrated in Fig. 5. However, returning a sample of Martian will require a significant amount of propellant due to the relatively deep Martian gravity. It is impractical and grossly inefficient that bringing the propellant from Earth.

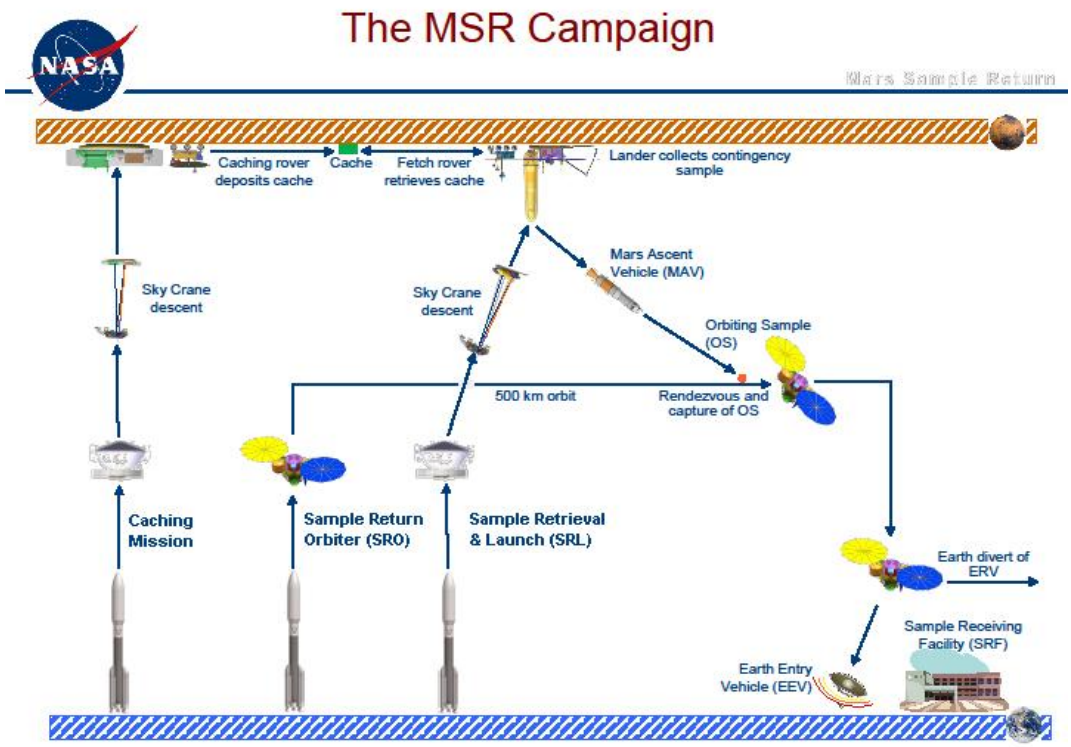

Fig. 5 NASA's Mars Sample Return Campaign Overview [26].

In-situ propellant production (ISPP) technology can be a very elegant solution to solve the problem of the return to Earth for the MSR campaign. Producing propellants directly on Mars can reduce mission costs, risks and entry, descent and landing (EDL) challenges.

ISPP requires two major technologies. First, we have to develop the CO_2 decomposition to obtain oxygen from the Martian atmosphere. The in-situ resource utilization (ISRU) on Mars is shown in Fig. 6. The atmosphere of Mars is composed almost of CO_2 above 95%. However, thermodynamically, CO_2 is a very stable molecule. So, CO_2 splitting must require a large amount of energy. The thermal decomposition ratio of CO_2 is about 0.2% at 1,400°C, which is too low. Therefore, researches on the direct thermolysis of CO_2 have been performed above 2,000°C [27, 28]. Thus, we need CO_2 decomposition techniques with a high energy efficiency for the ISPP technique on Mars. The CO_2 conversion into CO and O_2 using plasma is a promising approach. In the plasma state, molecules and atoms are partially ionized by the exciting energy. When the energy higher than ionization energy is applied to gas atoms, atoms (molecules) are separated into electrons and ions, and become the plasma state. Plasma can generate a diverse range of temperatures that significantly exceed those of conventional chemical processes. In addition, plasma is able to create a very high concentration of excited and chemically active species. Thus, in chemistry and related disciplines, plasma offers some advantages such as increasing the intensity and rate of chemical reaction, which would be unachievable in conventional chemistry technologies. In this study, we investigate the effect of Al_2O_3 and CaO catalyst for CO_2 dissociation under plasma, to obtain the best condition for CO_2 conversion and high energy efficiency.

Futhermore, the Martian soil contained a lot of metals such as Mg and Al. In particular, it is well-known that Al is used as additives to the fuel to increase the specific energy of combustion, and it has a high energy density of 15.485 kJ/g [29, 30]. However, when almost metals come into contact with oxygen in the atmosphere, an oxide layer is formed on the surface of their particles. Particularly, aluminum oxide (Al_2O_3) has a melting point of >2,000°C and its structure is too dense for the oxidizing agent to contact with aluminum in the oxide layer [31]. In the present study, the ignition of aluminum powders using the hydrogen combustor based on the solid sodium borohydride ($NaBH_4$) thermal decomposition was carried out. Characteristics of the hydrogen combustor were investigated

by evaluating the hydrogen generation rate through the thermal decomposition of $NaBH_4$ as the air supply rate was varied. From the results, the optimum condition for the ignition of aluminum powders was determined. Based on the characteristics of $NaBH_4$ thermal decomposition, the aluminum ignition was carried out to verify the applicability of the proposed method for the ignition system of aluminum powders.

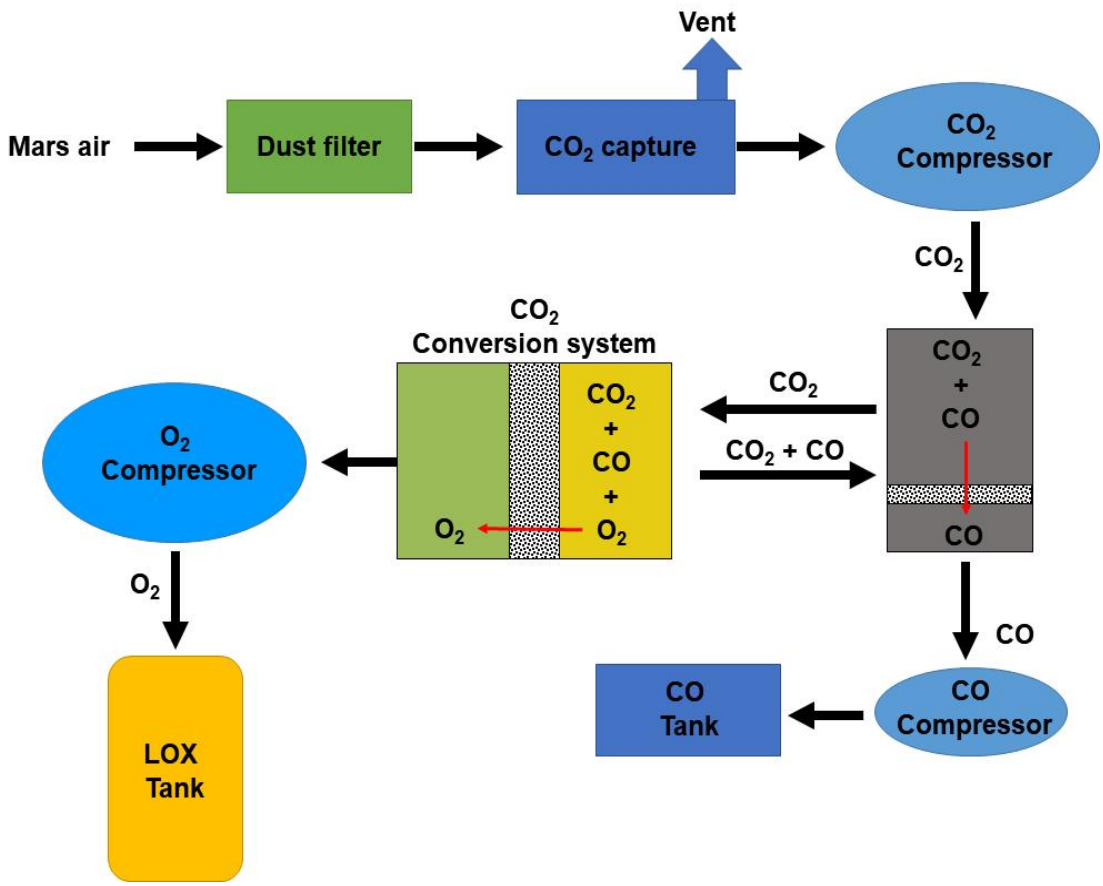

Fig. 6 Schematic of the in-situ resource utilization (ISRU) on Mars.

Table 1. Resources on Mars [2].

Atmosphere	Abundance
CO_2	95.32%
N_2	2.7%
Ar	1.6%
O_2	0.13%
CO	0.07%
H_2O	0.03%

Soil	Percent by mass
Mg	5.0±2.5
Al	3.0±0.9
Si	20.9±2.5
S	3.1±0.5
Cl	0.7±0.3
K	<0.25
Ca	4.0±0.8
Ti	0.5±0.2
Fe	12.7±2.0
L*	50.1±4.3
X**	8.4±7.8

* L is the sum of all elements not directly determined

** If the detected elements are all present as their common oxides(Cl expected), then X is the sum of component not directly detected, including H_2O, NaO, CO_2 and NOx

Ⅱ. Plasma system

2.1. Introduction to plasma

Plasma is referred to as the 'fourth state of matter' and simply defined as ionized gas [32]. In the plasma state, molecules and atoms are partially ionized by the exciting energy. When the energy higher than ionization energy is applied to gas atoms, atoms (molecules) are separated into electrons and ions, and become the plasma state, as shown in Fig. 7.

Plasma can occur naturally, e.g., auroras, lightning, and solar flares, but also can be generated artificially in the laboratory in various conditions [32, 34]. Plasma can generate a diverse range of temperatures that significantly exceed those of conventional chemical processes. In addition, plasma is able to create a very high concentration of excited and chemically active species. Thus, in chemistry and related disciplines, plasma offers some advantages such as increasing the intensity and rate of chemical reaction, which would be unachievable in conventional chemistry technologies [32-35].

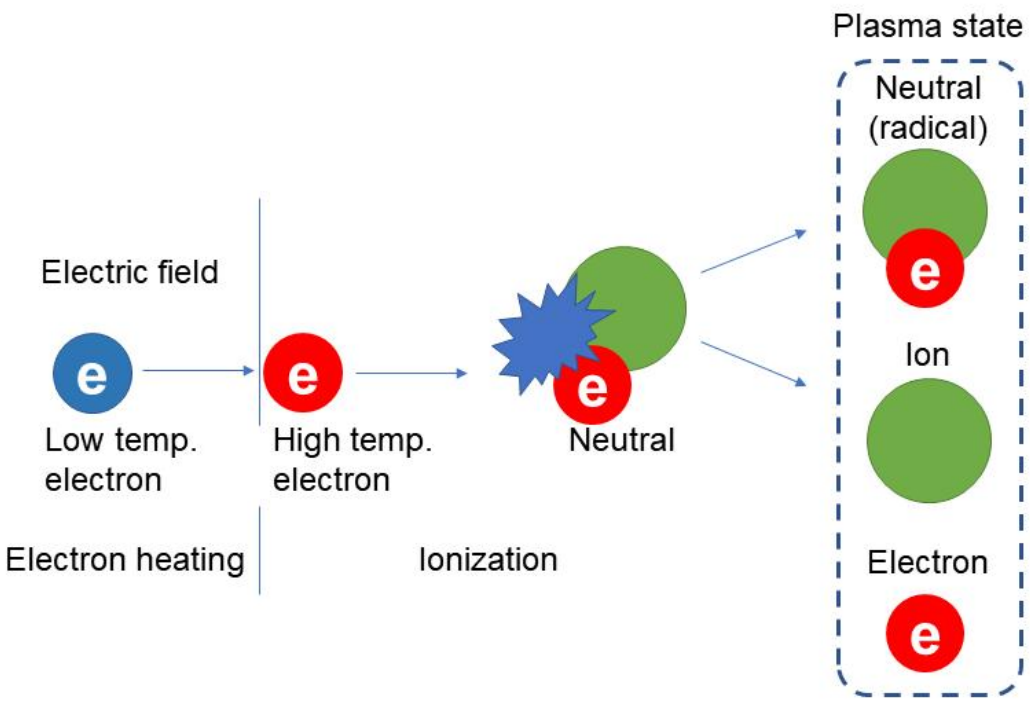

Fig. 7 The process of generation plasma.

2.2. Plasma temperatures

2.2.1 Thermal plasma

The condition in which the electron temperature (T_e) reached the heavy particle translational temperature (T_0) is defined as a thermal plasma, and the temperature of the thermal plasma is 4,000-20,000 K depending on the degree of ionization [32-34]. The weakly ionized plasma due to Joule heating can lead to the temperatures changing to reach equilibrium between the electrons and heavy neutral particles' temperature. At high pressure, more collisions occur due to the mean free path becomes smaller, which leads to more efficient energy exchange between the electrons and the heavy particles. Thus, the plasma is conventionally proportional to the square of the ratio of the electric field (E) to the pressure (p) [32].

Thermal plasma has many advantages, compared to traditional thermal technologies, because of their interesting characteristics including high temperature, high intensity non-ionizing radiation, and high energy density [34]. As mentioned above, the thermal plasma can reach 20,000 K or higher, which cannot be achieved by other technologies such as burning fossil fuels. So, the thermal plasma has been widely used for fine powder synthesis, coating technology and the treatment of hazardous waste resources.

2.2.2 Non-thermal plasma

Non-thermal plasma (NTP) is a non-equilibrium system characterized by the electron temperature (T_e) that significantly exceeds heavy particle temperature (T_0). For many non-thermal plasmas, the temperature relation is as follows: $T_e > T_v > T_r \approx T_i \approx T_0$ [34]. The electron temperature remains the highest followed by the vibrational temperature (T_v), both being higher than the rotational temperature (T_r) which is considered close in value to the ion temperature (T_i) and neutral heavy particle temperature [32, 34]. In these types of discharges, the electron temperature is usually close to unity measured in units of eV (equivalent to 11,600 K) with the gas temperature (T_0) close to room temperature. This high electron temperature can be easily accelerated by the applied electromagnetic fields because of the small mass of the electrons, but the heavy particles are not easily accelerated. In addition, during elastic collisions with heavy particles, the electrons lose less

energy. Thus they can easily remain their high energy gained from the electric field.

NTP is gaining the increased interest in recent years due to the solution to the effective CO_2 conversion into valuable chemicals and fuels. The gas temperature in NTP can be as low as room temperature but the electrons accelerated by the applied electric field have energies of 1-10 eV, which is high enough for CO_2 splitting [33-34, 36].

Table 2 Classification of plasma [34].

Plasma	State	Example
High temperature plasma (Thermal equilibrium)	$T_e \approx T_i \approx T_g$, $T_p = 10^6$-10^8K $n_e \geq 10^{20} m^{-3}$	Laser fusion plasma
Low temperature plasma (Quasi-equilibrium)	$T_e \approx T_i \approx T_g \leq 2 \times 10^4$K $n_e \geq 10^{20} m^{-3}$	Arc plasma, Plasma torches, RF inductively coupled discharges
Non-thermal plasma (Non-equilibrium)	$T_e >> T_i \approx T_g = 300$-$10^3$K $n_e \geq 10^{10} m^{-3}$	glow, corona, DBD

T_e=electron temperature, T_i=ion temperature, T_g=gas temperature, T_r=rotational temperature, T_v=vibrational, and n_e=number density

2.3. Different types of Plasma

2.3.1 Dielectric barrier discharge (DBD)

The DBD consists of two plane-parallel or coaxial metal electrodes and contains dielectric barriers between the electrodes such as glass, quartz, ceramic material, and polymer [37-39]. The role of the dielectric barrier is to limit the current to prevent the formation of sparks or arcs [40]. As shown in Fig. 8, DBD has a straightforward configuration. Typically, the DBD operates at atmospheric pressure, and an alternating voltage with an amplitude of 1-100 kV is applied between both electrodes [40].

To initiate the DBD, the electric field should be applied that is high enough to cause a breakdown of the gas. This breakdown voltage (V_b) is a function of the pressure (p) and the distance of the discharge gap (d), and it can be determined by Paschen's law.

$$V_b = \frac{D \cdot pd}{\ln\left(\frac{C \cdot pd}{\ln(1/\gamma)}\right)} \tag{1}$$

Where C, D and γ are the gas (or mixture) specific parameter. Among the plasma system for CO_2 decomposition, DBD has been most extensively studied because its temperature can be as low as room temperature and it is easy to operate.

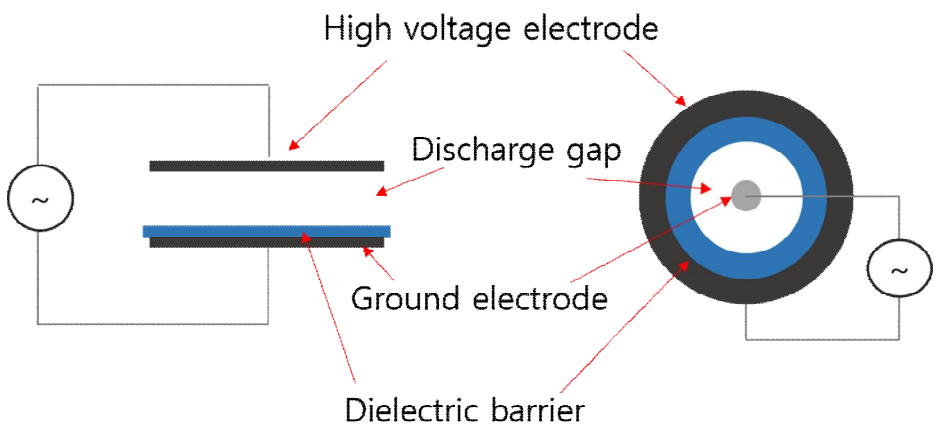

Fig. 8 Basic planer (left) and cylindrical (right) dielectric barrier discharge configurations.

2.3.2 Gliding arc discharge (GA)

A gliding arc (GA) discharge is a transient type of arc discharge. In general, the GA is an auto-oscillating periodic discharge between two diverging electrodes submerged in a gas flow (see Fig. 9). The arc is self-started at the shortest electrode distance and pushed by the gas flow into the diverging electrode region. The arc length increases until the applied voltage is insufficient to maintain the extended arc length or until another arc is initiated at the shortest electrode distance [41, 42]. When GA operates at low current and high frequency, this transition to non-local thermal equilibrium (LTE) phases can occur in nanoseconds. For currents of a few amperes, the initial arc is close to LTE state while the arc close to extinction is far from LTE. The generated arc at very low current as 100 mA and below can have the characteristics of a glow discharge even at atmospheric pressure [41-44]. The glow-arc transition is caused by the rise of current, and the value of the transition depends on the discharge condition and the type of gas. GA discharge can be powered by slightly different electrical methods, but they are all relatively inexpensive and easy to set up, making them very attractive for industrial applications.

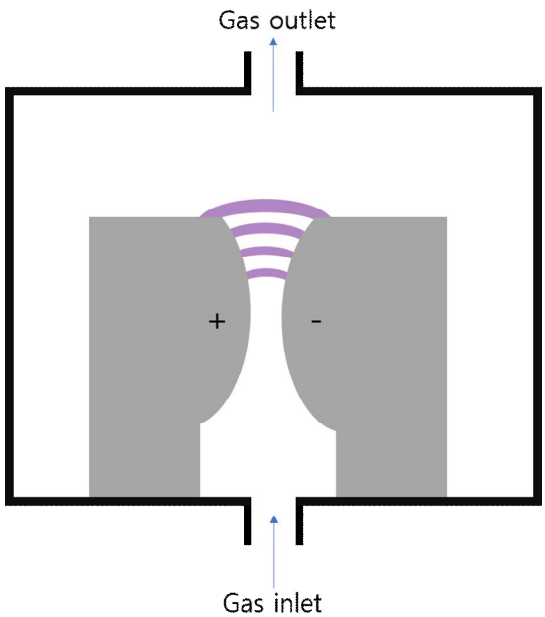

Fig. 9. Schematic of the classical GA configuration.

2.3.3 Microwave discharge (MW)

Unlike DBD and GA, microwave (MW) discharge is electrode-less, and electric power is supplied as a microwave in the frequency range of 300 MHz to 10 GHz [45, 46]. The MW discharge, so-called surface-wave discharge, the gas flows through a quartz tube cross a waveguide, where the discharge is initiated as shown in Fig. 10 [47]. The gas temperature of MW in non-equilibrium conditions is in the order of 1,000-2,000 K and its electron temperature is much higher as 3,000 up to 8,000 K [45]. However, when the gas temperature becomes thermal equilibrium as the increase of pressure, the temperature increases rapidly up to 14,000 K, and low values of energy efficiency are observed [45, 47-49]. The MW system for CO_2 conversion can achieve the high energy efficiency as above 60%, because of the combination of relatively high electron density and low field decay [45, 48]. However, it must be operated at the low pressure (50-200 torr) in order to reach non-equilibrium conditions, making it difficult to use in industry.

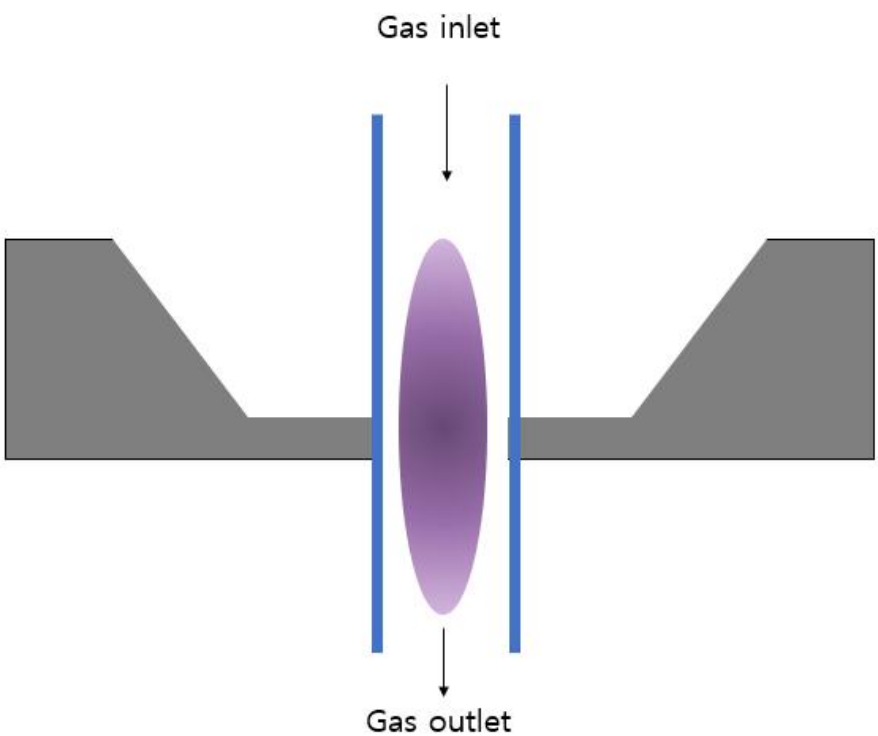

Fig. 10. Schematic (left) and image of a MW discharge.

2.4 Plasma-assisted catalytic system

2.4.1 plasma-catalyst

The plasma-assisted catalytic system provides can improve the process performance in terms of conversion, yield, selectivity and energy efficiency. As illustrated in Fig. 11, for plasma-catalytic synergy effect, the plasma-catalyst system can be classified as two configurations. The major difference between two configurations is the location of the catalyst. In the single-stage configuration, the catalyst is located inside the discharge zone, so plasma and catalyst could interact directly with each other. For the two-stage type, the catalyst is placed after the plasma discharge region. In microwave (MW) and gliding arc (GA) discharge, the temperature of the discharge zone is above 1,000 K, so the catalyst is located at the downstream of the plasma region due to the durability problems of the catalyst [45].

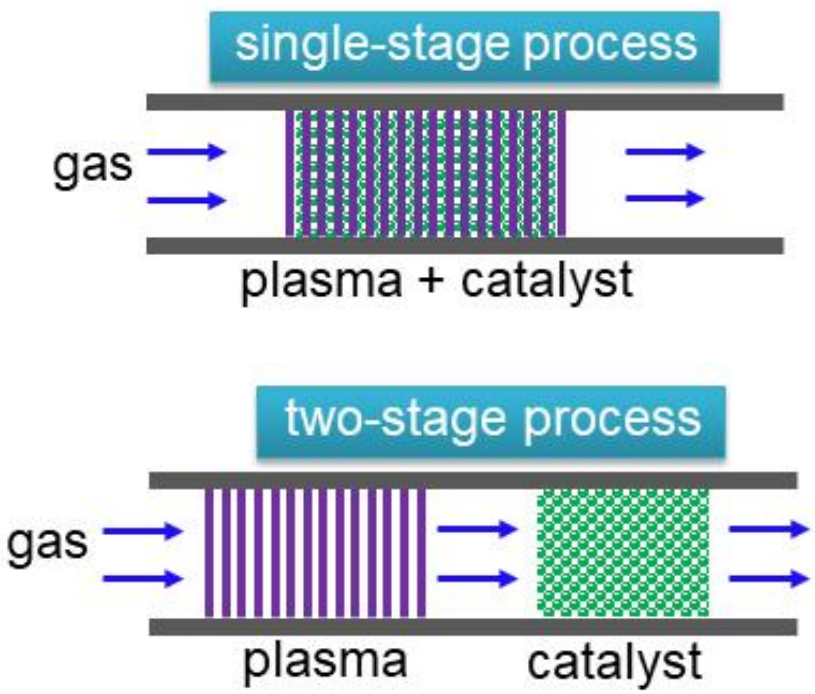

Fig. 11. Schematic of the different plasma-catalyst configuration

2.4.2 Synergy effect in plasma-catalytic system

The reaction process of the plasma-catalytic system was presented in Fig. 12. The plasma- catalytic reaction condition is quite different from conventional catalysis. It could be mostly attributed to synergistic effects based on the complicated interaction between the plasma species and the surface of catalysts. These interactions can be distinguished by physical and chemical effects. Generally, the effect of the catalyst on the plasma is considered as physical effects as follows [45, 50] :

ⅰ) enhancement of the electric field due to the surface roughness and geometric distortion.
ⅱ) formation of micro-discharges inside the pore of the catalyst, which leads to different characteristics compared to the bulk discharge since the powerful electric field inside the pores.
ⅲ) the presence of insulating surfaces which accelerate the evolution of surface discharges, so the discharge type is changed.
ⅳ) extension of the reaction time due to the species adsorption on the catalyst surface, which affects concentration and conversion.

Conversely, the effects of the plasma on the catalyst are considered as not only physical effects but also chemical effects as follows [45, 50] :

ⅰ) change of physicochemical characteristics such as a higher surface area of catalysts, improvement of the adsorption on the catalyst surface, change of the catalyst oxidation state, and increased reducibility of metal oxide.
ⅱ) hot spots on the surface, which leads to the formation as the strong micro-discharge.
ⅲ) higher possibility of non-adiabatic barrier because the excited plasma is vibrationally more reactive.
ⅳ) change of the reaction pathway because of the many kinds of active species.

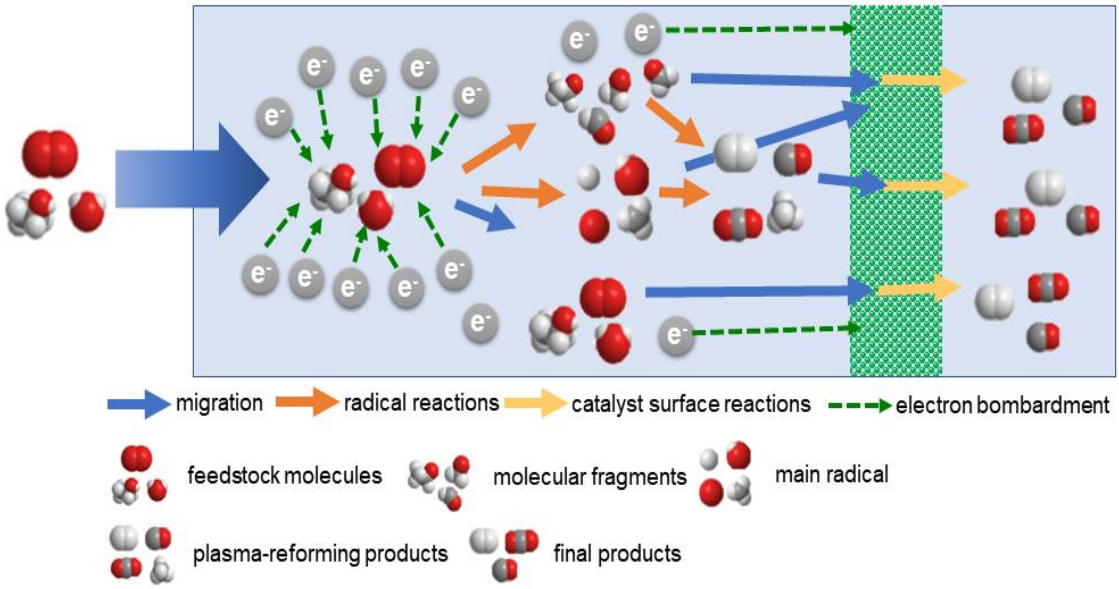

Fig. 12. The schematic of the plasma-catalytic system reaction process.

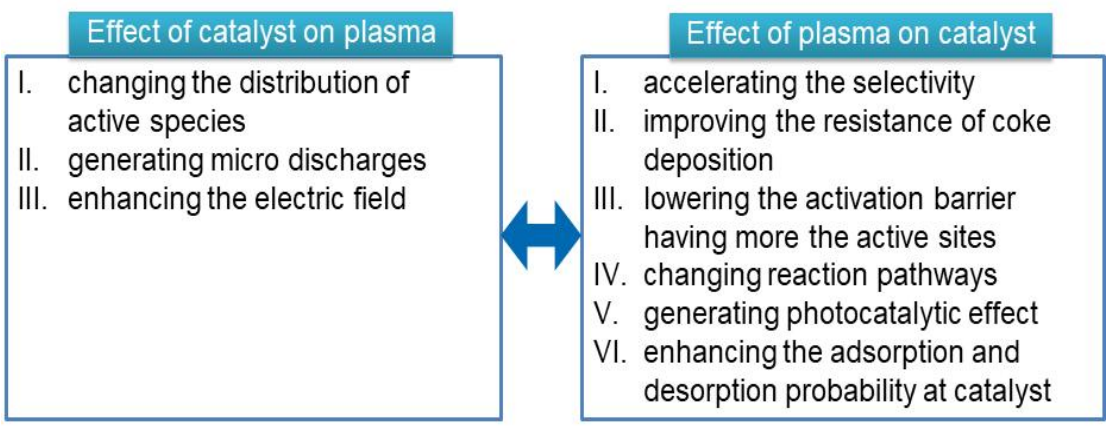

Fig. 13. Possible plasma-catalyst synergy effect.

Ⅲ. Plasma-assisted catalytic system for CO_2 conversion

3.1 Overview

Plasma offers one of the possible solutions to convert the CO_2 into useful compounds in many fields such as gas purification and energy conversion. In addition, plasma is attractive for chemical and order industrial applications because it can generate a significantly high temperature using lower energy than traditional chemical processes. Furthermore, plasma can improve the strength and efficiency of chemical reactions because it can make a chemically active species and a significant concentration of excited species [45-48, 51]. Indeed, non-thermal plasma (NTP) generates high energy electrons (1-10 eV), which is high enough for CO_2 dissociation [51]. Notably, the plasma-assisted catalytic system provides the improved process performance in terms of conversion, yield, selectivity, and energy efficiency.

3.2 DBD plasmas for CO_2 conversion

Among the plasma system for CO_2 decomposition, dielectric barrier discharge (DBD) has been most extensively studied because its temperature is as low as room temperature and it is easy to operate. To improve the performance, we can change the configuration of the reactor, diluent gas, flow rate of the input gas, packing material, input power and so on.

3.2.1 Influence of discharge length and discharge gap

Increasing the discharge length extends the residence time of CO_2 gas in the discharge region, which enhances the conversion because of the increased probability of CO_2 molecules colliding with high energy electrons and reactive species. However, at a fixed SEI, varying the discharge length has no considerable effect on the discharge characteristics, conversion, and energy efficiency [52]. On the other hand, the larger discharge gap shows the lower conversion and energy efficiency since it causes the reduced electric field strength [45, 52]. The low electron density leads to the decrease of CO_2 conversion due to the reduction of the electron impact reaction rates.

3.2.2 Influence of discharge power on CO_2 conversion and energy efficiency

The discharge power is a critical factor that affects CO_2 conversion and energy efficiency because it determines whether the energy is applied enough to activate the dissociation the CO_2 molecules. Increasing the discharge power leads to the improvement of CO_2 conversion but, tends to decrease the energy efficiency. The higher discharge power means that the more energy are supplied into the DBD plasma system. Thus it can improve the CO_2 activation and produce more reactive products [45, 52-54]. However, when the power beyond a certain value is provided, the CO_2 conversion reaches saturation so that it should be investigated a suitable range of the discharge power for high energy efficiency.

3.2.3 Influence of diluent gas on CO_2 conversion and energy efficiency

Adding diluent gases such as Ar, He and N_2 makes the plasma generated more easily and stable. Moreover, it has several effects on the conversion, energy efficiency, and discharge characteristics. The addition of Ar, He and N_2 causes an increase in CO_2 conversion and energy efficiency. The order of energy efficiency is well-known as Ar > He > N_2. Ramakers et al. [55] reported that at the diluent gas mixture up to 70%, both He and Ar have the same effect, but at a higher gas concentration, Ar was more effective than He. However, the effective conversion decreases because there is less CO_2 presence in the diluent gas, and the slightly increased conversion is not sufficient to respond to this drop in the CO_2 fraction. Besides, adding the N_2 causes the formation of unwanted by-products such as N_2O and NO_x.

3.2.4 Influence of packing materials and beads size

To obtain a high CO_2 conversion and energy efficiency, we need to choose a suitable bead size. A. Zhou et al. [57] reported that decreasing the bead size provides the increased discharge surface area, and it reinforced the surface discharge, which accelerates the CO_2 dissociation rate. Therefore, the smaller bead size is more beneficial for CO_2 conversion.

The introduction of packing materials might be the most decisive factor affecting the discharge characteristics. Zhou et al. [57] observed that the packing of ZrO_2 or glass beads into the discharge zone generates a typical packed-bed effect. It causes the transition in the discharge behavior from a combination of surface discharge and filament discharge into the

filament discharge due to the reduction of a spike in the discharge signal. Ozkan et al. [58] reported that a thicker dielectric leads to a higher conversion and energy efficiency. Notably, ZrO_2 and $BaTiO_3$ exhibited a significant effect on the CO_2 conversion and energy efficiency compared with the result of the unpacked DBD reactor. Table 3 shows the CO_2 conversion and energy efficiency in different packed DBD plasma reactors.

Table 3 Summary of the CO_2 conversion and energy efficiency in DBD discharge.

Catalyst	Conversion (%)	SEI (J/mL)	Energy efficiency (%)	Reference
ZrO_2	52.1	-	7.0	[57]
$BaTiO_3$	28	60	7.1	[59]
$CaTiO_3$	20.5	52.95	4.8	[60]

3.3 MW discharge for CO_2 conversion

As mentioned in Chapter 2, microwave discharges can achieve high energy efficiency of CO_2 dissociation due to a combination of their relatively high electron density and low reduced electric field. These conditions prefer the excitation of the asymmetric mode vibration level of CO_2. In MW discharge, CO_2 molecules are usually excited at the lowest vibration level and are followed by vibrational-vibrational collisions, which gradually fills the higher vibration level, thus leading to the dissociation of the CO_2 molecules [48, 61]. In several studies, it is attempted that changing the applied power, gas flow rate, reactor geometry, a and diluent gas to obtain high CO_2 conversion and energy efficiency.

In the 1970-1980s, it was reported that MW discharges provided the high energy efficiency for CO_2 splitting, due to a combination of their relatively high electron density and low reduced electric field (70-80 Td). Fig. 14 shows a plot of energy efficiency as a function of acquired the specific energy input in different discharge systems through

experiments and simulations. Curves 1 and 2 show non-equilibrium calculation in one- and two- approximations. Curves 3 and 4 show the non-equilibrium calculations in supersonic flows as M = 5, and 3.5, respectively. ○, ◆, Δ, and × indicate the experimental results in different microwave discharges. ● represent experimental data in supersonic microwave discharges. In many experimental results, microwave discharge can be attaining the high energy efficiency for CO_2 conversion, which occurs at the conditions of $E_v \approx$ 0.3-1.0 eV/mol [32, 33].

However, recent studies suggest that the values applied to the reduced electric field, i.e., 70-80 Td, were too high, so future studies should be directed towards values around 20-50 Td while maintaining the temperature in the discharge as low as possible [62]. Therefore, it might not be advantageous for high-throughput industrial applications so that the experiments were performed at reduced pressures in despite of the high flow rates of up to 75 SLPM. Indeed, increasing the pressure leads to a significant decrease in the energy efficiency, which is nevertheless still a factor twice higher than that obtained by the DBD [45].

Britun et al. [63] reported that the adjustment of the microwave power led to rather promising results for CO_2 conversion. The input power is an important impact factor on the thermal equilibrium as the different electron-molecule collision frequencies under different power densities [48]. The power density linearly depends on the electron density. The electronic energy distribution function provides a significantly increased average electronic energy with more microwave power to the plasma. In addition, the enhanced power led to the expansion of the plasma region, extending the retention time of the reactants [64].

Chen et al. [65] performed the dissociation of CO_2 in a MW with TiO_2 supported NiO catalyst at 1330 Pa (10 torr), which investigated the effect of the catalyst on the CO_2 conversion and energy efficiency. The CO_2 conversion and energy efficiency increased almost twice compared to those without the catalyst from 23% to 42% and 9.6% to 17.2%, respectively.

Bongers et al. [49] reported that energy efficiency in the supersonic expansion experiments was only 15%, but by additionally quenching the plasma, the energy efficiency of up to 47% was observed at a plasma pressure of 200 mbar.

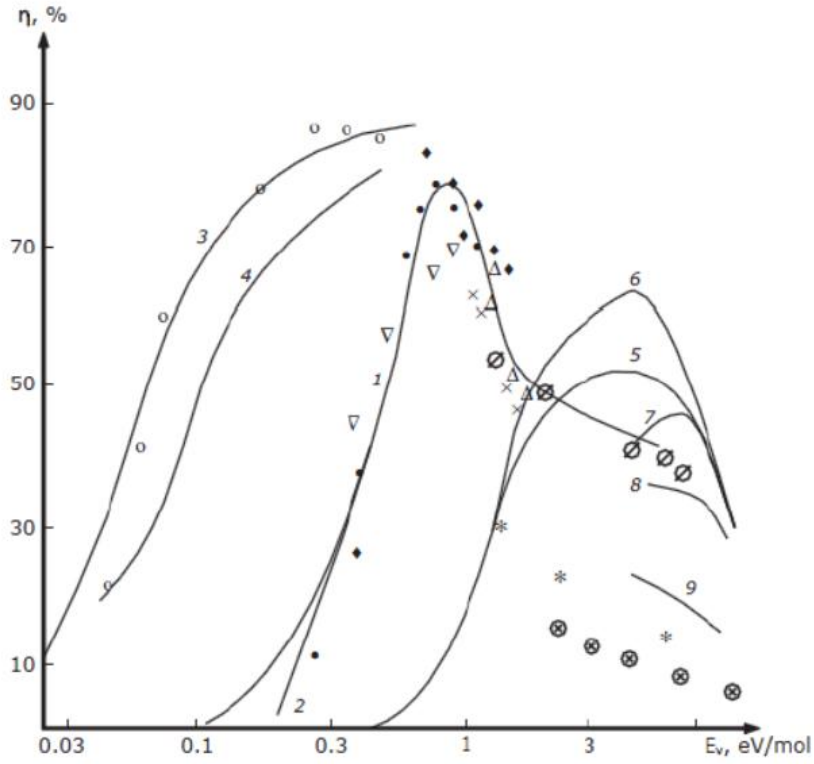

Fig. 14 Energy efficiency of CO_2 dissociation in different discharge systems [32].

3.4 GA plasma for CO_2 conversion

A gliding arc (GA) discharge is an attractive technology for gas conversion because it has advantages of both thermal and non-thermal plasma. Thermal arc discharge can be generated between two electrodes in atmospheric pressure and the low external circuit resistance. Notably, the GA plasma is seen as the most energy-efficient way to dissociate CO_2 molecules than other types of plasmas because it can reach a strong non-equilibrium enough to stimulate the most efficient decomposition process through vibrational excitations [45, 66].

The traditional flat gliding arc reactor consists of two divergent electrodes. However, this configuration has very low conversion efficiency because the flow rate is more limited and the residence time in the plasma is very short. Indeed, the gas flow processed by the discharge is only about 20% depending on the actual geometry. As a result, the theoretical maximum conversion is about 20% in GA [67, 68]. To solve these problems, rotating

gliding arc (RGA) discharge is proposed, in which the flow is processed by the discharge co-driven by a magnetic field and tangential flow [69]. The RGA configuration consists of cylindrical electrodes and the gas follows a vortex flow pattern, which makes possible longer residence times in the discharge zone, even at high flow rates [45]. It can be processed about 40% of the gas flow and the theoretical maximum conversion is double compared to the traditional GA configuration. Table 5 shows the CO_2 conversion and energy efficiency in GA discharge.

W. Wang et al. [70] confirmed that for CO_2 conversion using the GA the dissociation of vibrationally excited states of CO_2 upon collision with O atoms is the most important process for CO_2 conversion, which the CO_2 vibrational levels significantly contribute to the CO_2 decomposition. Furthermore, they have found how to inhibit the reverse reaction to improve the CO_2 conversion through the 2D-modeling, and achieved a high energy efficiency of 47%. However, CO_2 conversion is too low at 4.0%.

H. Zhang et al. [67] investigated the influence of the mixture gas (N_2 or Ar) on the reaction performance in the rotating gliding arc (RGA). Increasing N_2 or Ar concentration, enhances the CO_2 conversion due to the formation of more reaction routes for CO_2 conversion, however, energy efficiency decreased at a concentration of N_2 or Ar above 30%. In terms of conversion and energy efficiency, N_2 is more favorable compared to Ar due to the formation of more reaction routes. However, the addition of N_2 can lead to the production of unwanted harmful compounds, as N_2O and NO_x compounds.

Table 5 Summary of the CO_2 conversion and energy efficiency in GA discharge

Configuration	Conversion (%)	SEI (J/mL)	Energy efficiency (%)	Reference
RGA	4.0-4.4	3.5	16-17	[67]
RGA	5.1	33	35	[68]
GA	2.64	1.0	41.1	[70]
GA	17.4	15.4	14.1	[71]

3.5 In-situ DRIFTS spectroscopy for investigation of the plasma-catalytic reaction mechanism

3.5.1 Infrared spectroscopy

Infrared (IR) spectroscopy uses to analyze the IR radiation of which the fraction of the incident radiation is absorbed in a particular wavelength. It deals with a variety of technologies, mainly based on the absorption spectrometry. IR spectroscopy is a very powerful technique for qualitative and quantitative analysis and can yield the analysis and verification of molecular information.

Generally, the IR of electromagnetic spectrum is divided into near-infrared, mid-infrared, and far-infrared (as shown in Fig. 15). In order to identify and characterize matters, almost all types of electromagnetic radiation are used for spectroscopy [72, 73].

- ▶ Near-infrared (12820-4000 cm^{-1}) : poor in specific absorptions, can excite overtone or harmonic vibrations.
- ▶ Mid-infrared (4000-400 cm^{-1}) : provides fundamental vibrations and the associated rotational-vibrational structure for most organic molecules.

▶ Far-infrared (400-33 cm^{-1}) : adjacent to the microwave region, has low energy and may be used for rotational spectroscopy.

Typically, low energies generated in the IR region are not enough to cause electronic, but they are sufficient to cause changes in the frequency and amplitude of molecular vibrations. In the IR spectroscopy, polychromic radiation passes through the sample and molecular vibration is excited by absorption of light with matching frequencies [73]. These molecular vibrations are IR-active when the moment of molecular dipole moment changes during the bond oscillation.

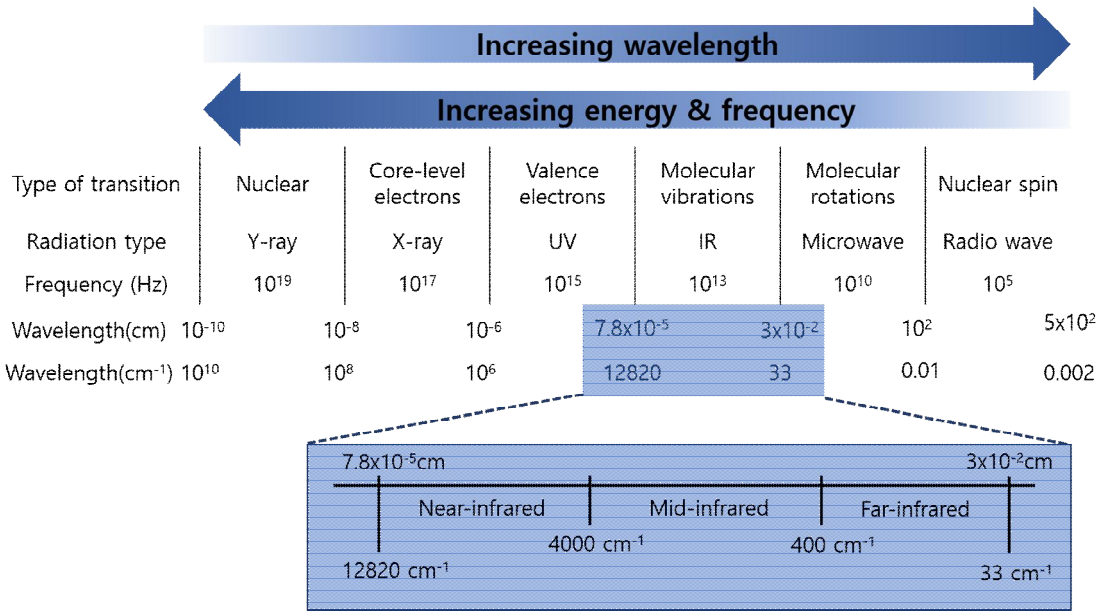

Fig 15. The electromagnetic spectrum and the infrared region [73].

3.5.2 Vibrational spectroscopy

The atoms of molecules are linked to each other by chemical bonds, which are not rigid, and vibrate around the equilibrium point at their natural frequency. Molecular vibration can be excited due to the absorption of quantum energy (E) corresponding to its vibrational frequency (ν ´). The vibrational frequency of a chemical bond depends on the electronic structure of the molecule, the bond strength, and the atomic mass [72]. The

molecule can absorb the radiation when a bond in a molecule vibrates at the same frequency as the incident electromagnetic radiation ($\nu = \nu'$). As shown in Fig. 16, the frequencies of molecular covalent bond vibrations are in the infrared region, which can absorb the IR radiation. Vibration spectroscopy can provide information about the molecular structure of a substance because the frequency of a molecule's vibration has a specific wavelength depending on the mass of the atom, the strength of the bond, the stiffness, and the type of bonds [72, 74]. Fig. 16 shows the possible vibrational modes of molecules.

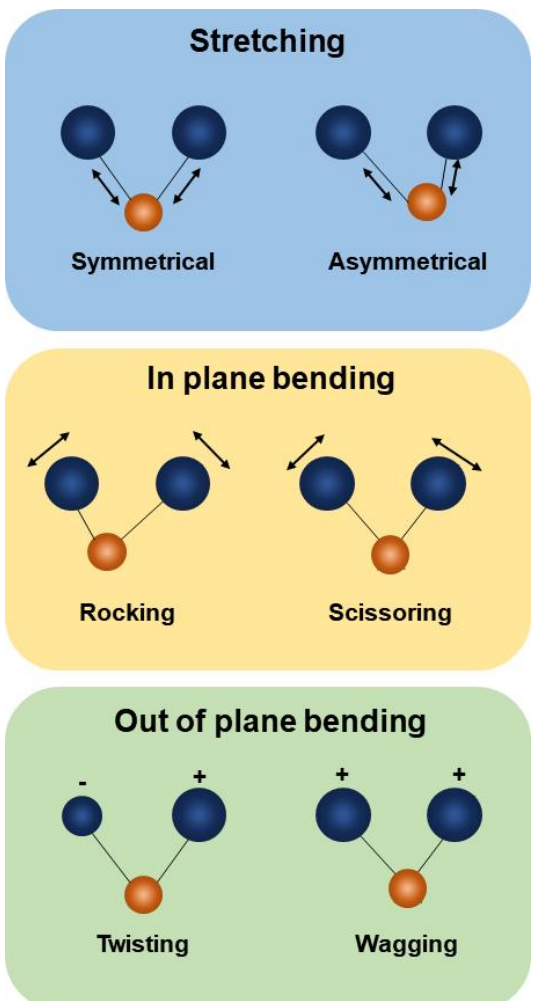

Fig. 16. Possible vibrational modes of molecules.

3.5.3 Fourier-transform infrared (FTIR) spectroscopy

Fourier-transform infrared (FTIR) spectroscopy is a technique used to obtain an IR spectrum of absorption and emission of a solid, liquid or gas [73, 74]. FTIR converts the raw wavelength data collected by a detector into the spectra using a Fourier transform (FT) algorithm. The FTIR spectroscopy enables the real-time measurement of response trends and profiles, and provides very specific information about the effects of response variables on dynamics, mechanisms, reaction paths. FTIR provides important information as it researches, develops, and optimizes chemical compounds, synthetic pathways, and chemical processes because it directly tracks the changes that occur during the reaction process of reactants, reagents, intermediate products, products and byproducts [73].

As reported in the literature before, the resulting interactions when combining a plasma with a catalyst often provide the improved performance in terms of conversion, selectivity, yield, and energy efficiency. However, the reason and the exact mechanism of these performance improvements are still not clear. Therefore, the plasma-catalyst interaction phenomena and synergy mechanism was investigated via in-situ diffuse reflectance infrared Fourier transform spectroscopy (DRIFTS) in this study.

Ⅳ. In-situ resource utilization by plasma-assisted catalytic system

4.1 CO_2 extraction

As mentioned in chapter 1, regarding the return of the Martian sample, it is required that the propulsion system with a comparatively large velocity change capability due to the relatively deep Martian gravity. Therefore, the significant amount of propellant will be required but bringing the propellant from Earth would be impractical and grossly inefficient. In-situ propellant production using the martian resource would be more practical. As well known, the composition of the Martian surface atmosphere is composed almost entirely of CO_2 (95.32% by mole). It is enough amount to produce the propellant on Mars.

4.1.1 Objectives

The CO_2 for the ISPP system needs to be extracted from the atmosphere and then compressed for storage. The extraction of CO_2 can be performed by adsorbent microporous materials that can trap vapors and gas molecules within their pores. Calcium-based materials have attracted attention as an excellent sorbent for cyclic CO_2 capture processes due to its potential regeneration. Notably, calcium oxide (CaO) can capture and release CO_2 through the reversible carbonate looping cycle at atmospheric pressure. Fig. 17 shown the schematic representation of a conventional calcium looping cycle. The CO_2 gas supplied to the calcium looping reactor is reacted with calcium oxide at 650°C. The reverse reaction (calcination) is generally carried out at above 950°C under atmospheric pressure. However, this process is very inefficient to use on Mars because it must be required a large amount of energy. Specifically, the problem of energy efficiency associated with high-temperature calcination is drawbacks, which should be addressed and improved. In this thesis, we performed that the plasma-assisted CO_2 adsorption with CaO using a low current plasma under 100 mA for high energy efficiency. In addition, the mechanism of plasma-assisted CO_2 adsorption was investigated by in-situ DRIFTS spectroscopy.

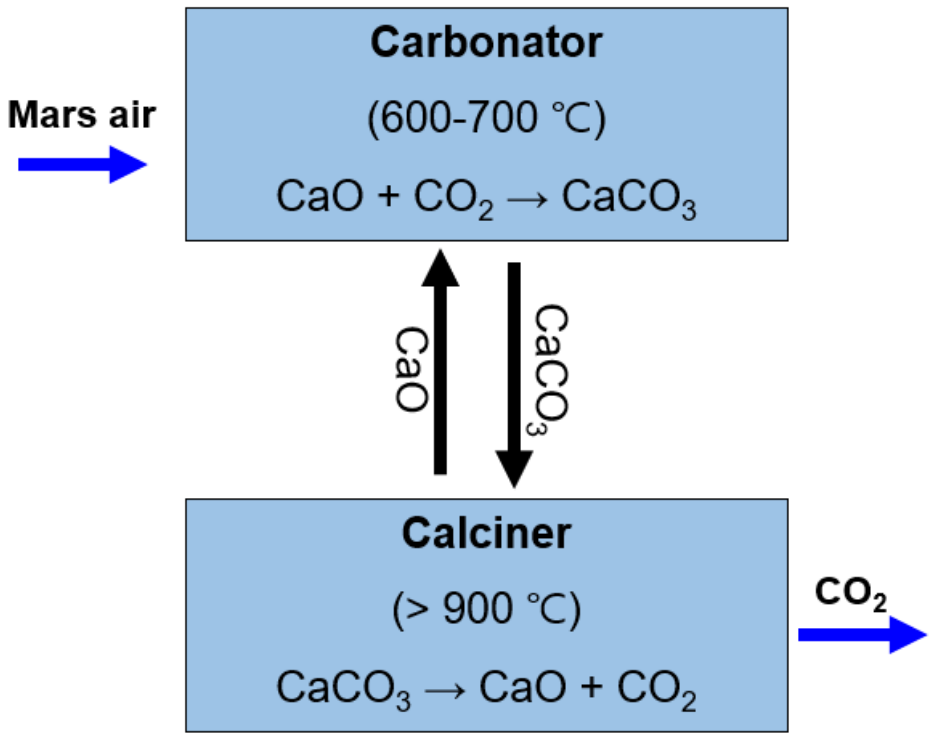

Fig. 17 Thermochemical calcium looping cycle of calcium oxide

4.1.2 Experimental setup and plasma-assisted catalytic CO_2 adsorption

The CaO was characterization by XRD. The performance of CO_2 adsorption on the CaO under plasma excitation was analyzed by temperature programmed desorption (TPD). In addition, the mechanism of CO_2 adsorption under the plasma was investigated by in-situ DRIFTS spectroscopy.

X-ray diffraction (XRD): XRD patterns of the sample before and after the plasma-excited CO_2 adsorption were recorded in a Empyrean (PANalytical) with Cu-Kα radiation (λ =0.1542 nm, 60 kV, 55 mA) in the 2θ scanning range between 5° and 90° with a scan rate of 5° min^{-1} and a step size of 0.02°.

In-situ DRIFTS spectroscopy: In-situ FTIR spectrum of absorbed species on CaO under the CO_2-excited plasma was recorded in the diffuse reflectance infrared Fourier transform

spectroscopy (DRIFTS) using the MB3000 (ABB) FTIR spectrometer (Fig. 18) equipped with the SelectorTM Accessory P/N GS19000 (Fig. 19) at a resolution of 16 cm^{-1}. The diffusion reflectance is based on the collection of diffusely scattered radiation from the sample. Fig 20 (a) shows an IR beam pass in the designed reactor for in-situ FTIR analysis. DRIFTS accessory was set-up in a closed system made of acrylic. The IR beam through the ZnSe window is directed to the M1 mirror and onto the M2 mirror. The IR beam is then projected to an input ellipsoid mirror (M3) which then focuses the light onto the surface area of a sample held in a cup that is positioned on the top of the sample post. A scattered IR beam at the sample surface is collected by the ellipsoid mirror (M4), reflected through the mirror M5 and M6, and finally directed to the detector through the ZnSe window. Fig. 20 (b) shows a homemade reactor with a ZnSe window. The catalyst was filled in the sample cup with powders without any pre-processing. Then, the inside of the reactor was evacuated in the vacuum condition to 50 mbar and then He was injected until the ambient pressure was formed. The reference spectrum was recorded under this condition. After setting the reference condition, CO_2 and He were introduced as 50 mL/min, and 500 mL/min, respectively. Subsequently, a plasma jet was generated at a discharge power of 20 W. The powder samples were filled in the sample cup on which a heater was attached. The change of spectrum according to the temperature of sample was observed.

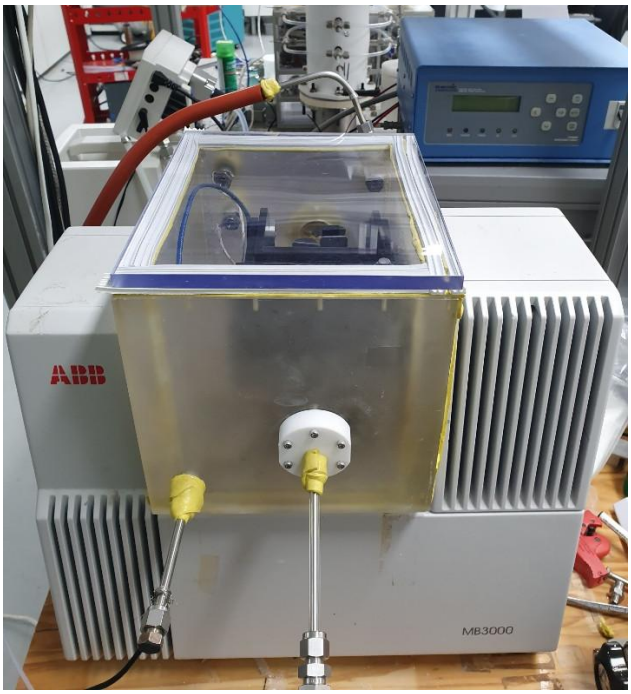

Fig. 18. FTIR spectrometer

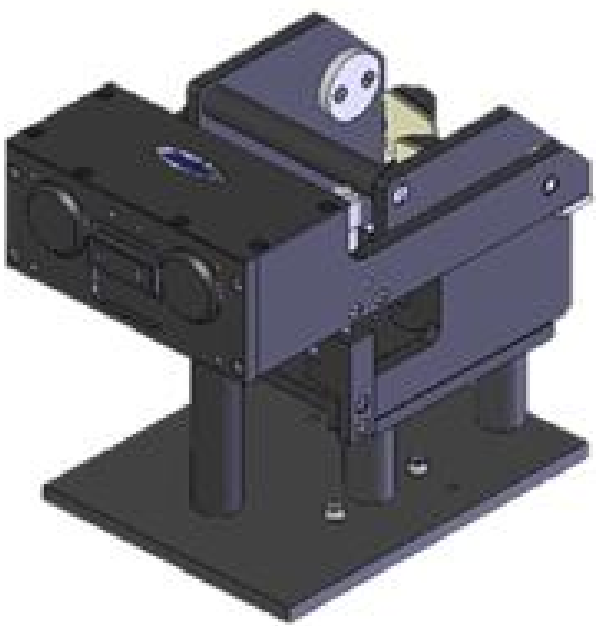

Fig. 19. DRIFTS accessory (Space, SelectorTM Accessory P/N GS19000)

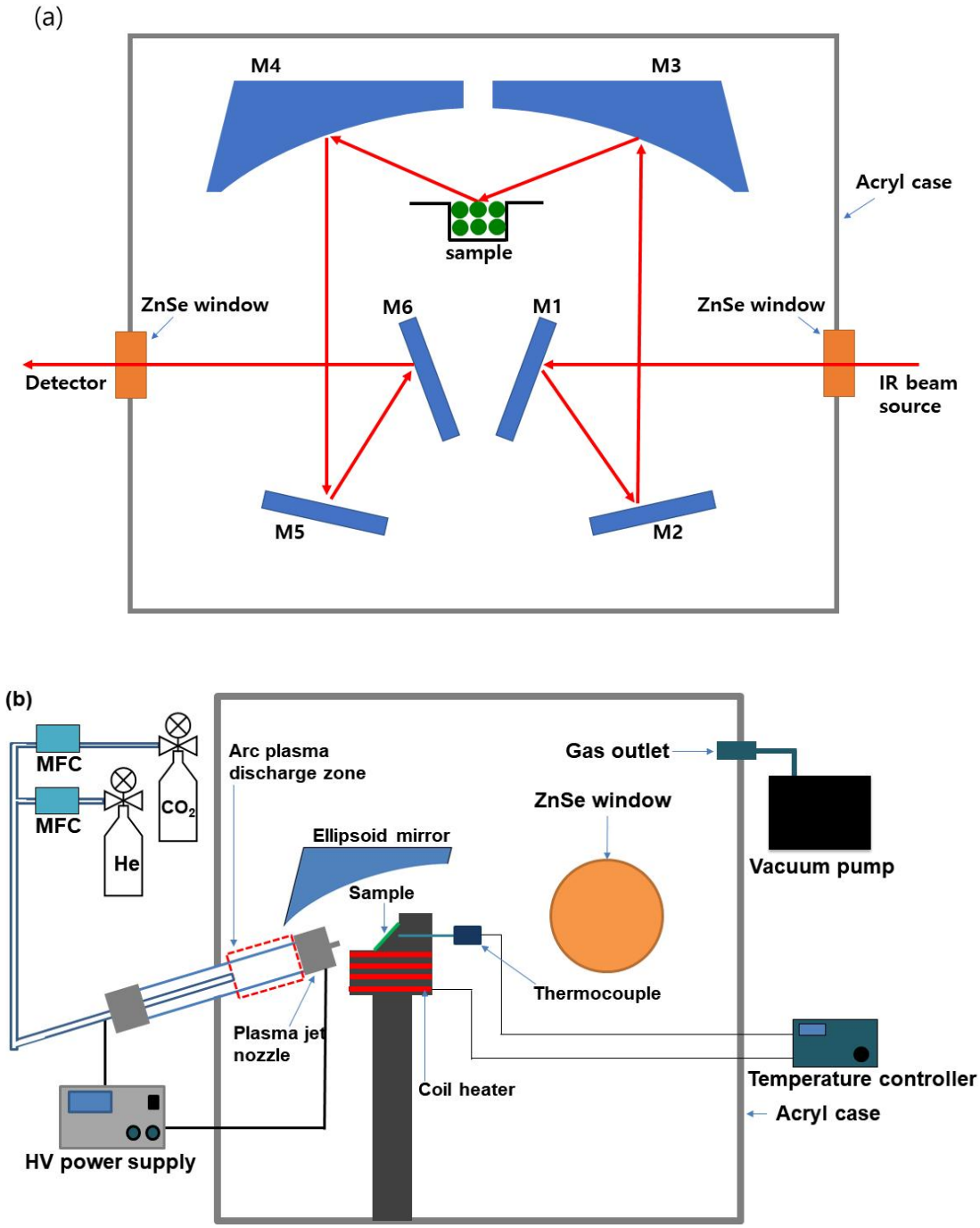

Fig. 20 Schematics of DRIFTS configuration, (a) optical components and sample and (b) schematics of in-situ FTIR spectroscopy reactor.

Temperature programmed desorption (TPD): The schematic diagram of the experimental setup is shown in Fig. 21. The CaO was reduced in 2 vol.% H_2/He for 4 hours at 400°C after calcined in He flow at 700°C until the baseline of FTIR became stable. After cooling down to room temperature, the adsorption of plasma-excited CO_2 was performed at the discharge power of 20 W for 1 hour. CO_2 adsorption under the plasma was performed in a low-current arc plasma (LCAP) reactor made of quartz with an outer diameter of 26 mm and a wall thickness of 1 mm. The plasma was powered by a 1 kW AC power supply (APAP-01KH, ATU). The high-voltage (HV) electrode was made of SUS and the distance between two electrodes was 25 mm. In the present work, the current was fixed under 0.1 A, and the temperature of the discharge area was measured by an IR image camera. The gas flow rate was controlled by MFC (F201CL, Bronkhorst). The CO_2 diluted with He was injected from the top of the reactor through the mixing chamber. After passing through the reactor, gaseous products were analyzed in real-time using FTIR (MB3000, ABB). These experiments were carried out at room temperature and atmospheric pressure. After then, the CaO was treated with He until the baseline of FTIR signal was stable. Next, the desorbed CO_2 was detected using FTIR in He flow with increasing the temperature from 30°C to 700°C (5°C/min).

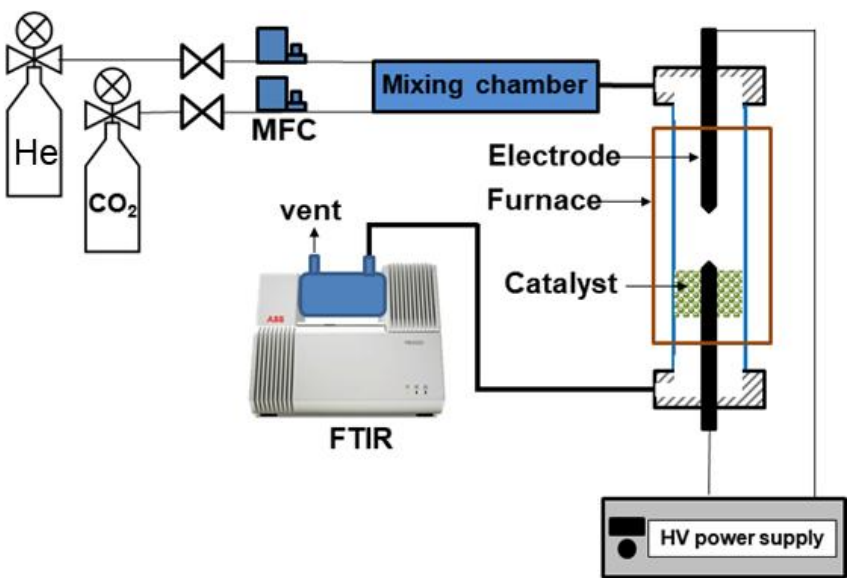

Fig. 21 Schematic diagram of the TPD experimental setup.

4.1.3 Results and discussion

XRD patterns of the CaO before and after the plasma-excited CO_2 reaction are demonstrated in Fig. 22. The maximum temperature of the reactor with CaO catalyst was 466°C when the plasma was applied. After the plasma-excited CO_2 reaction, the CaO peaks intensity were reduced at 2Θ of 32.25°, 37.40°, 53.92°, 64.21°, 67.44°, 79.72°, and 88.59°, while the $CaCO_3$ peak intensity increased at 2Θ of 29.43°. The CaO was reacted with CO_2 to produce the calcium carbonate ($CaCO_3$) at ~650°C [75, 76]. In addition, the calcium hydroxide ($Ca(OH)_2$) peaks were almost disappeared at 2Θ of 34.14°, 42.22°, and 50.85°.

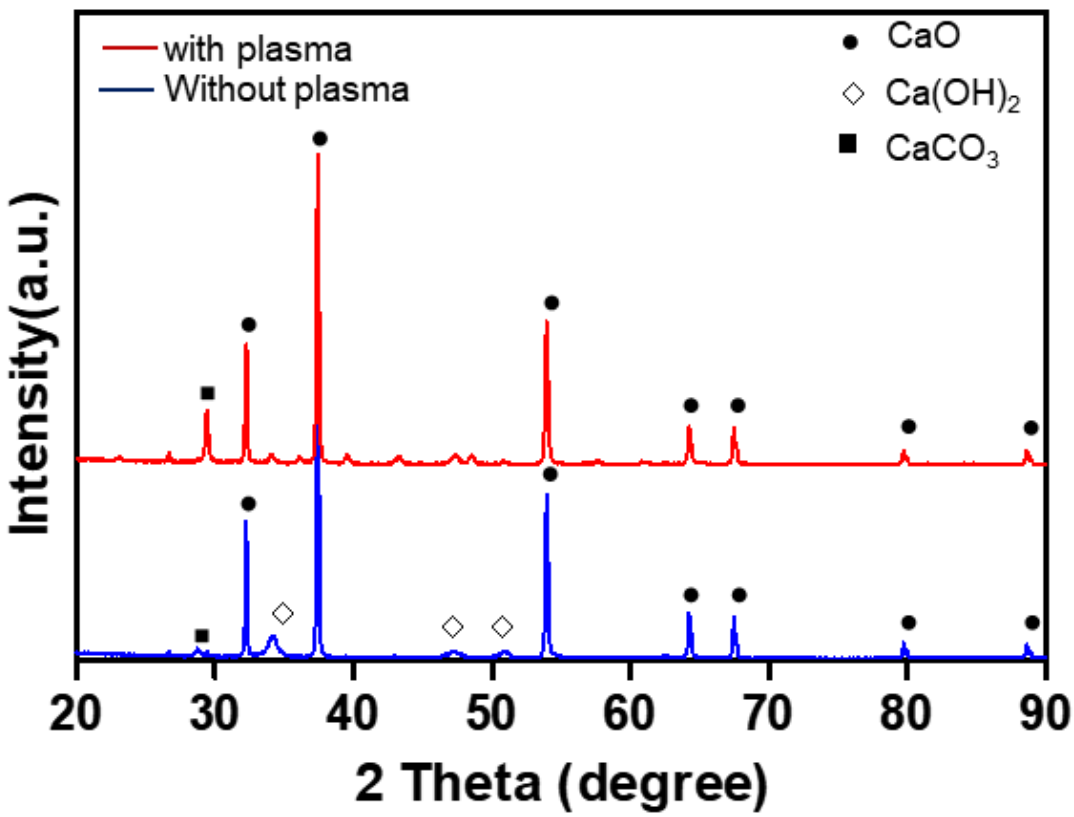

Fig. 22. XRD patterns of CaO with/without plasma.

As shown in Fig. 23, the ground state of CO_2 can be characterized into three modes of vibration including the symmetric stretching (ν_1), bending (ν_2), and asymmetric stretching (ν_3) [74]. The IR bands of reactants and products of CO_2 dissociation in the gas phase were indicated in Fig. 24 and Table 6. The IR bands at 3726 and 3626 cm^{-1} are assigned to the v_1+v_3 and $2v_2+v_3$ as a combination band, respectively. The IR band at 2338 cm^{-1} corresponds to the asymmetric stretching. The IR band corresponding to CO appears at 2176 and 2106 cm^{-1}.

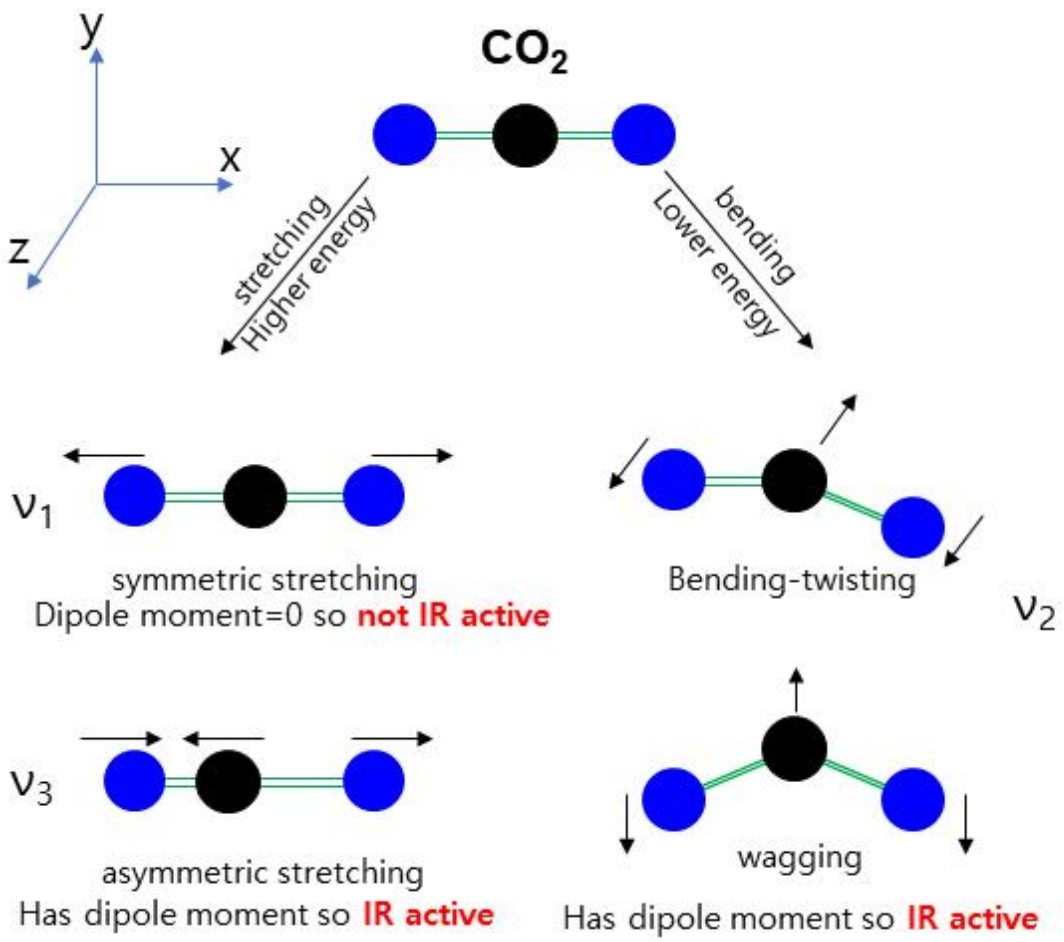

Fig. 23 Vibrational modes of CO_2, a triatomic linear molecule, and their IR activities.

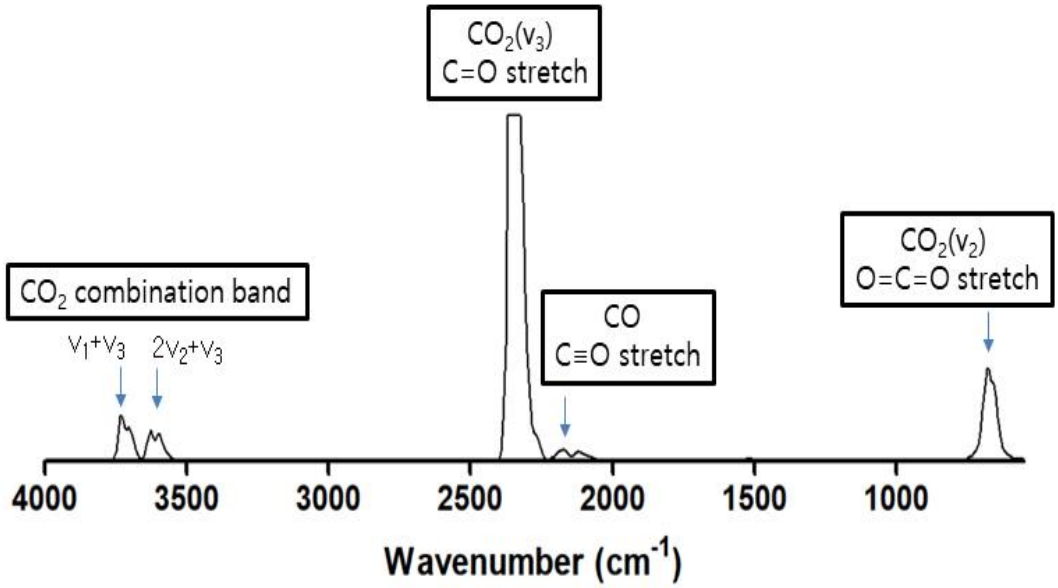

Fig. 24 IR bands of CO_2 and CO in the gas phase.

Table 6. IR band assignment of CO_2 dissociation reactants and products in the gas phase.

Molecule	Mode	Band position (cm^{-1})
CO_2	Combination band (v_1 + v_3)	3726
	Combination band ($2v_2$ + v_3)	3626
	Asymmetric stretch (v_3)	2338
CO	Stretch	2176
		2106

The FTIR spectrum change of the CaO before and after the calcination at 900°C is shown in Fig. 25. The sharp band at 3641 cm^{-1} was associated with OH stretching vibration mode of water physisorbed on the surface of the CaO [77]. This was related to OH in $Ca(OH)_2$ as shown in the XRD pattern. Similarly, the broad band centered at 3294 cm^{-1} was also assigned to the OH stretching modes. The broad band from 1258 cm^{-1} to 1427 cm^{-1} corresponded to the v_3 asymmetric stretching of the CO_3 group. The peak at 1089 cm^{-1} was detected due to the v_1 symmetric stretching mode of the CO_3 group, which implied the formation of calcite. The sharp peak at 864 cm^{-1} corresponded to the v_2 symmetric deformation of the CO_3 group. The peak at 731 cm^{-1} was due to the v_4 bending vibration [78, 79]. After calcination at 900°C, the mostly absorbed water from the CaO surface was removal.

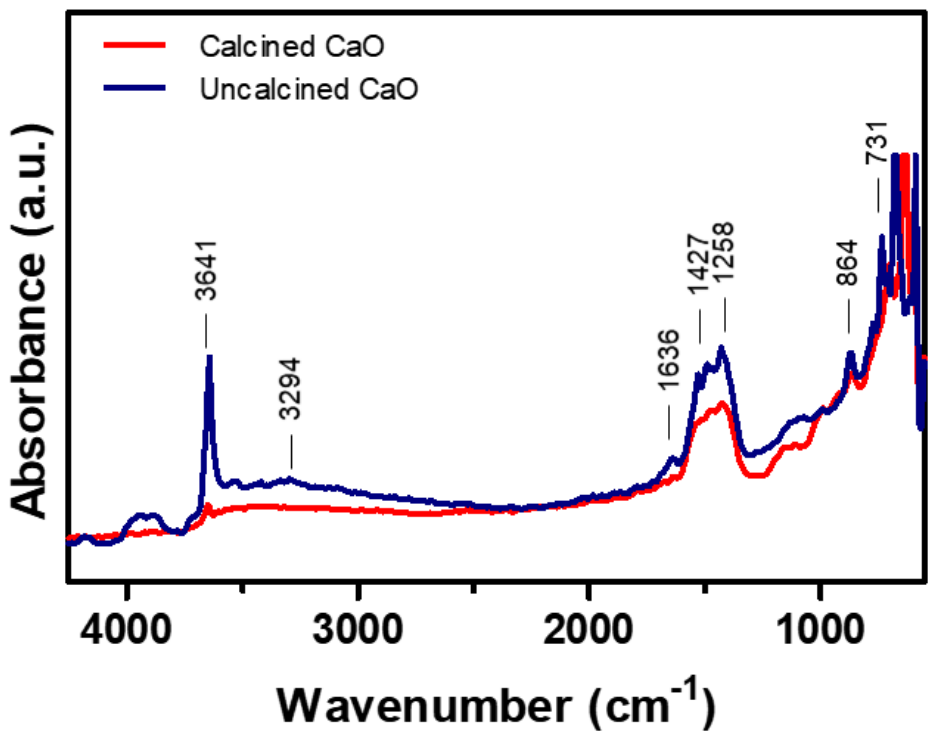

Fig. 25 The FTIR spectrum change of the CaO before and after the calcination at 900°C.

The temperature of the sample was not affected by the plasma as shown in Fig. 26. Thus, the sample temperature could be only controlled by the heater. The difference of the FTIR spectrum according to the temperature without plasma is shown in Fig. 27. As the temperature increased in the CO_2 atmosphere, the intensity of the stretching band of OH groups was not only reduced but also absorption peaks in the range 1504-1404 cm^{-1} markedly increased because of CO_3^{2-} ion, which implied the increase of the carbonate content. At the above 300°C, the peaks at 2500 and 1790 cm^{-1} were appeared due to the adsorption of the atmospheric CO_2 and C=O stretching, respectively [80]. Indeed, the intensities of corresponded CO_2 bands at 3726 and 3626 cm^{-1} were reduced as the temperature increased, and they decreased by 8.11% and 18.75% at 500°C, respectively. Especially, the band from 1504 to 1404 cm^{-1}, and 872 cm^{-1} corresponding to the v_3 and v_2 of the CO_3 group were conspicuously increased at above 300°C.

Fig. 26 The temperature of plasma nozzle and sample in the DRIFTS apparatus.

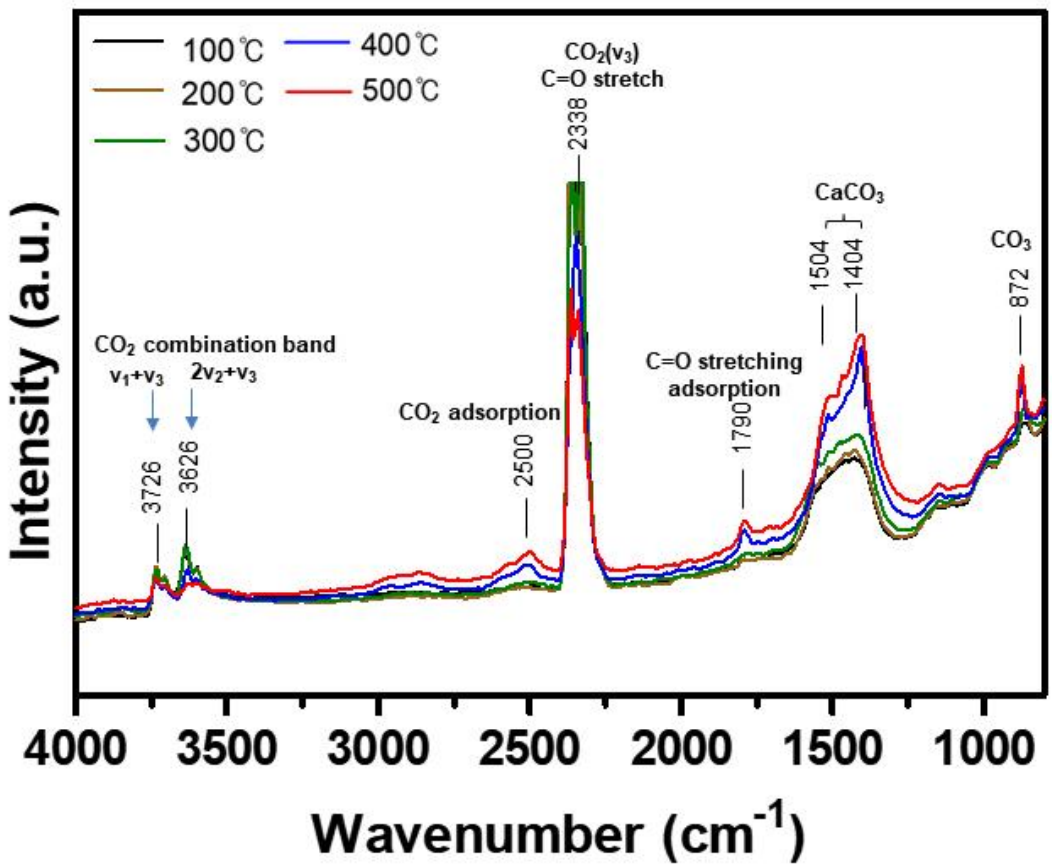

Fig. 27 The difference of the FTIR spectrum according to the temperature without plasma.

The IR intensities change on the surface of CaO accoridng to the temperature in the presence of plasma was depicted in Fig. 28. As a result, introducing the plasma seemed to improve the CO_2 adsorption on CaO. After the plasma was applied, the CO_2 band at 3726 and 3626 cm^{-1} were significantly reduced at 400°C, and notably decreased by 28.09% and 33.33% at 500°C, respectively. The adsorption of CO_2 on CaO was improved greater than a factor of 3 compared to results without plasma at 500°C. In addition, the interesting result was the appearance of the IR peak of 1636 cm^{-1} at 200°C and 300°C. The reaction of CaO with CO_2 is thermodynamically more favorable than that of $Ca(OH)_2$, [77].

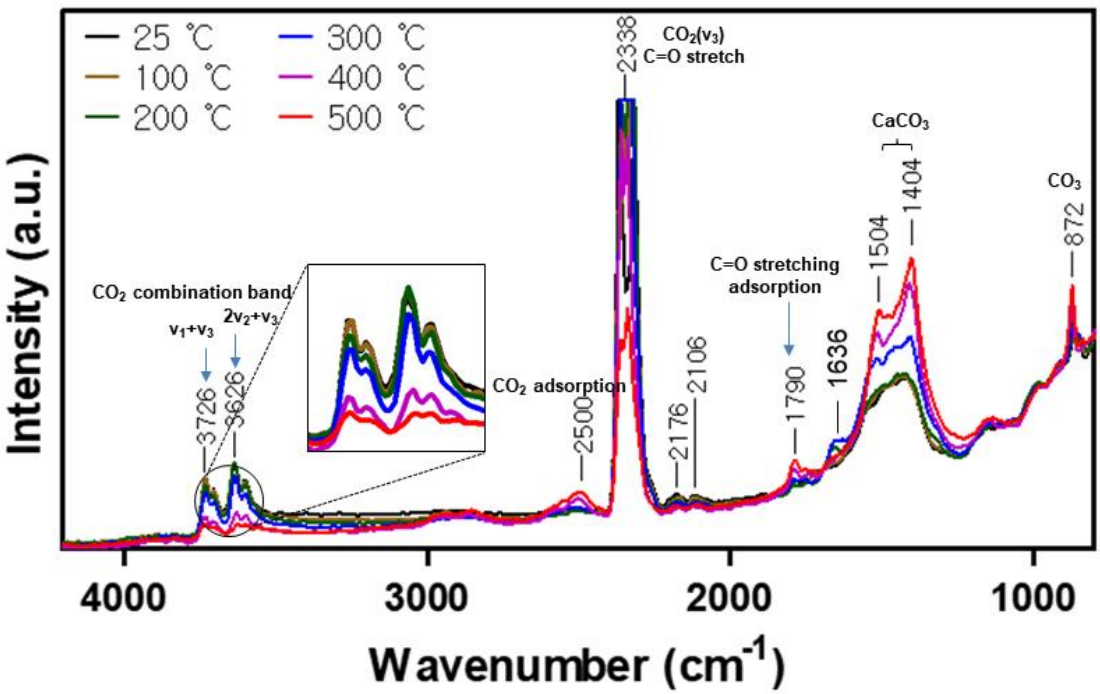

Fig. 28 The IR intensities change on the surface of CaO according to the temperature in the presence of plasma

However, we confirmed that $Ca(OH)_2$ and CO_2 were reacted at higher than 200°C, of which the evidence was the appearance of 1636 cm^{-1} peak at 200°C and 300°C.

$$CaO + CO_2 = CaCO_3 \text{ (calcite)}, \ \Delta_r G°(298.15K) = -143.1 \pm 1.3 \text{ kJ/mol} \quad (2)$$

$$Ca(OH)_2 + CO_2 = CaCO_3 + H_2O(l), \ \Delta_r G°(298.15K) = -74.1 \pm 1.3 \text{ kJ/mol} \quad (3)$$

The reaction of $Ca(OH)_2$ with CO_2 in the presence of moisture led to the formation of a carbonate crust on the surface of $Ca(OH)_2$. Then, the calcium bicarbonate ($Ca(HCO_3)_2$) was formed as expressed in Eq. 4. It was verified through the appearance of band at 1504 cm^{-1} [77, 78, 80]. The $Ca(HCO_3)_2$ band appeared at higher than 300°C after the presence of moisture peak at 1636 cm^{-1}.

$$CaCO_3 + CO_2 + H_2O = Ca(HCO_3)_2 \quad (4)$$

As mentioned in Fig. 25, most of the OH groups disappeared after the calcination, so the effect of them on CO_2 adsorption through the reactions of Eq. 3 and 4 would be insignificant. Nevertheless, the plasma changed the reaction pathway on the CaO surface, which could promote the reactions of Eq. 3 and 4, resulting in the improvement of CO_2 adsorption.

The intensity changes of CO_2, $CaCO_3$, and CO_3 with and without plasma are shown in Fig. 29 and 30, respectively. The intensity change of the $CaCO_3$ and CO_3 band with and without plasma was not observed, while the intensity of CO_2 bands at 3726 and 3626 cm^{-1} was notably reduced in the presence of plasma. Consequently, it means that the adsorption of plasma-excited CO_2 on CaO was based on physisorption, not chemisorption.

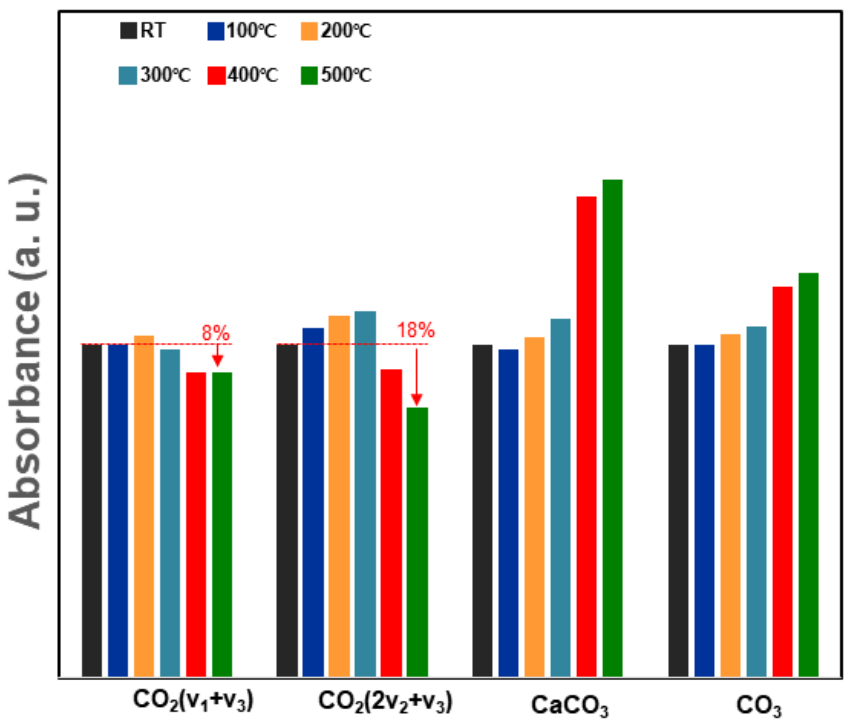

Fig. 29 The change of intensity of CaO according to the temperature in the absence of plasma.

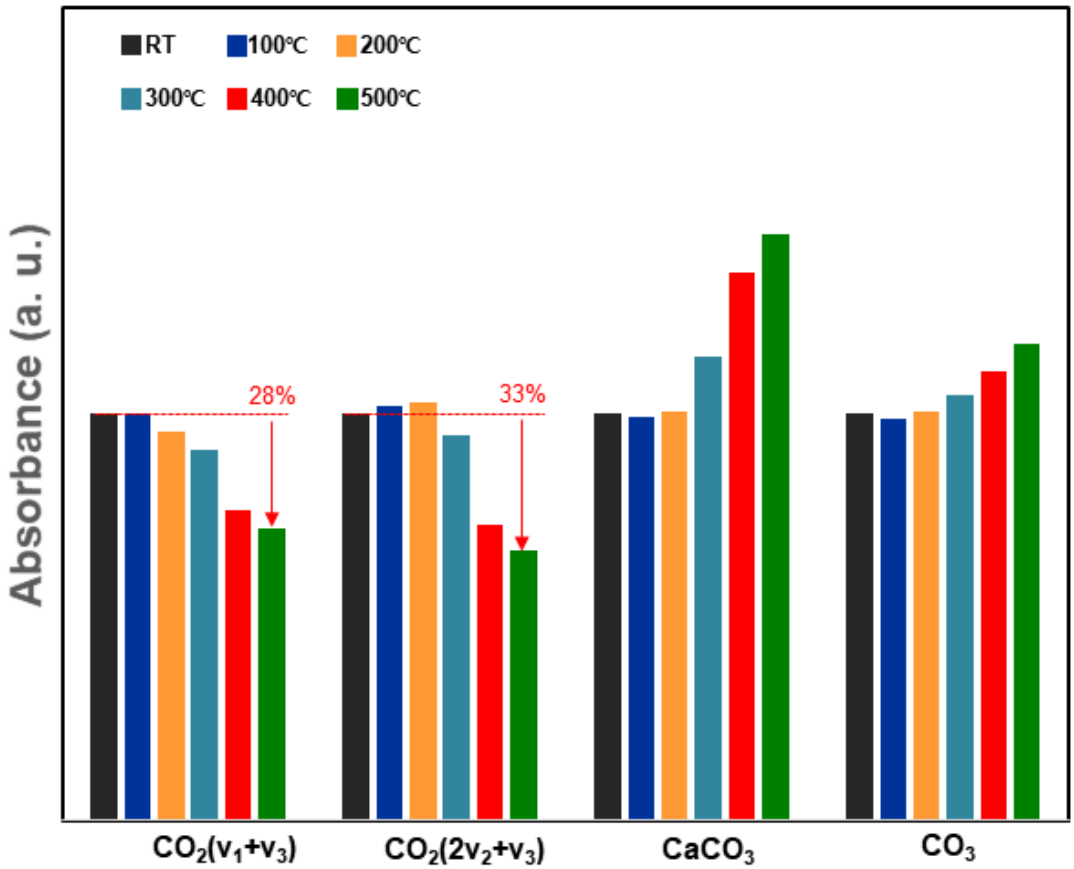

Fig. 30 The change of intensity of CaO according to the temperature in the presence of plasma.

Plasma-assisted CO_2 adsorption performance was characterized by TPD. The adsorption performance of CaO was compared with that of Al_2O_3. When the plasma was applied, the temperature of CaO is indicated in Fig. 31. The desorption characteristics between Al_2O_3 and CaO was clearly different as shown in Fig. 32. After performing the absorbance of the plasma-excited CO_2 on Al_2O_3 and CaO, the desorbed CO_2 was measured as increasing the temperature from 30 to 700°C (5°C/min) for every 1 min using FTIR. In the result of Al_2O_3, the CO_2 peak appeared at the temperature around 130°C. On the other hand, the CO_2 desorption peak of the CaO was mainly observed at 400-500°C. The CO_2 desorption temperature of CaO was higher than Al_2O_3, implying that the higher energy was needed to

desorb CO_2 from CaO than Al_2O_3. However, the amount of desorbed CO_2 on CaO was much higher than Al_2O_3, which can be attributed to the presence of CaO being highly active for CO_2 activation.

Typically, the CO_2 calcium looping cycle has been performed in the temperature range of 850-950°C. It was the main drawback of the cycle due to the energy penalty associated with the elevated temperature for both the capture and release components of the cycle. In this study, plasma was proposed as an attractive technology offering one of the possible solutions for CO_2 storage and extraction with CaO. This study proved that the plasma can improve the adsorption of CO_2 and also the physisorbed CO_2 on the surface of CaO was strongly adsorbed enough not to be desorbed under 300°C. Moreover, it was more efficient than the general calcium looping cycle because most CO_2 was desorbed under 600°C.

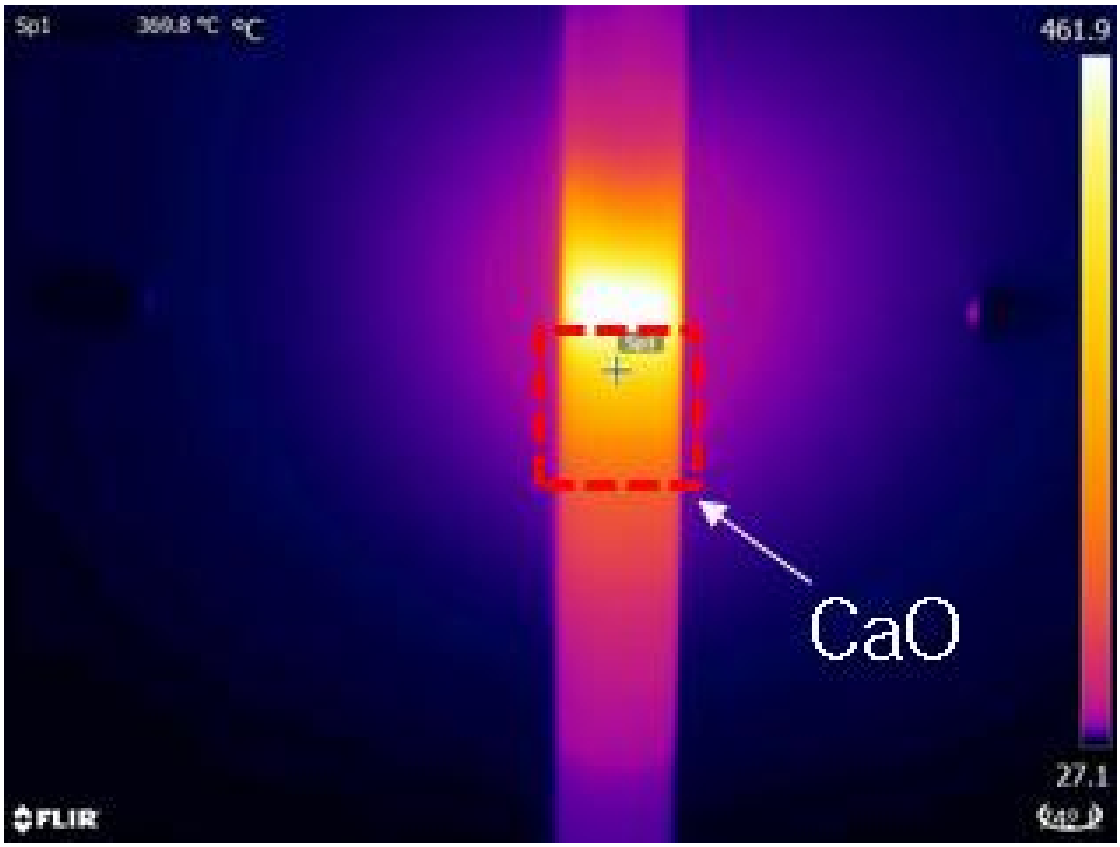

Fig. 31. The temperature of CaO when the plasma was applied.

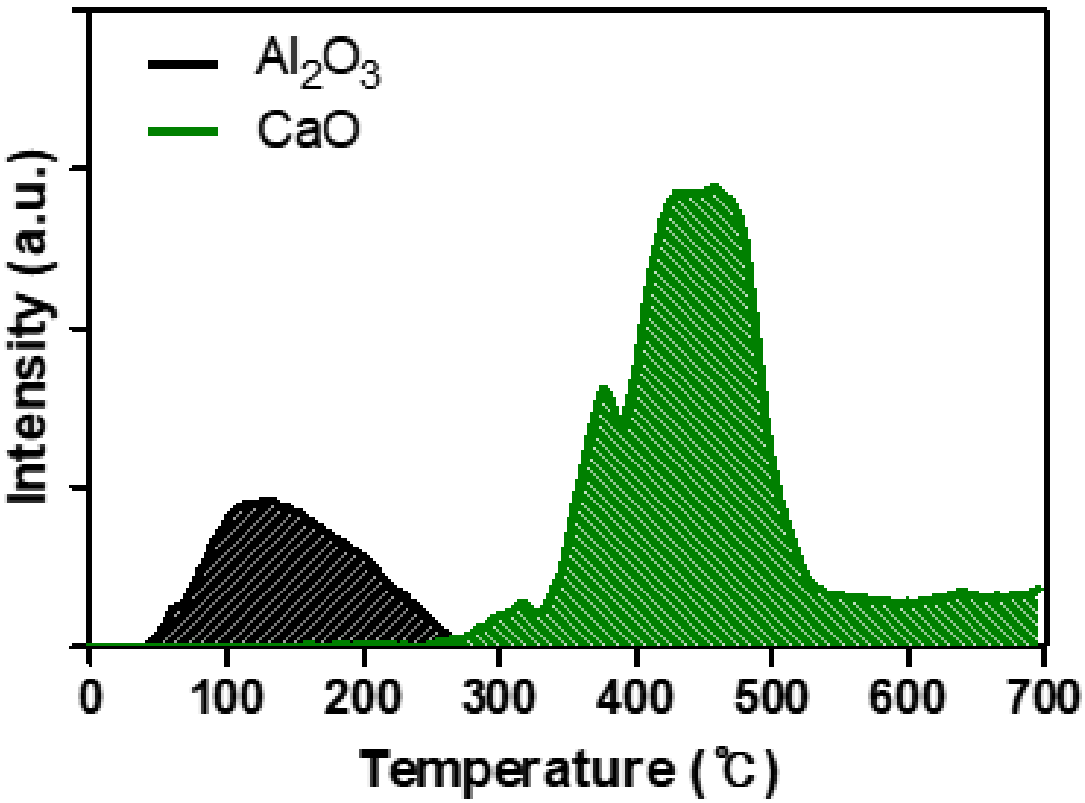

Fig. 32. Plasma-excited CO_2 TPD result of Al_2O_3 and CaO

4.2 In-situ decomposition of CO_2

Frisbee et al. [80] studied the CO_2 decomposition system using the zirconia (ZrO_2) membrane, which selectively captures, transports and extracts oxygen ions when the voltage was applied as shown in Fig. 33. In this system, CO_2 was chemically thermal-decomposed into CO and O_2 through the vicinity of the zirconia cell. Then the O_2 was extracted by the cell from the CO_2-O_2-CO mixture gas. The extracted O_2 was reduced and entered the membrane as an ion, and then was recombined as dioxygen after oxidation on the other side. This system could produce the oxygen of 0.325 g/hr at 800°C, but the low system efficiency was still problematic due to its high operating temperature.

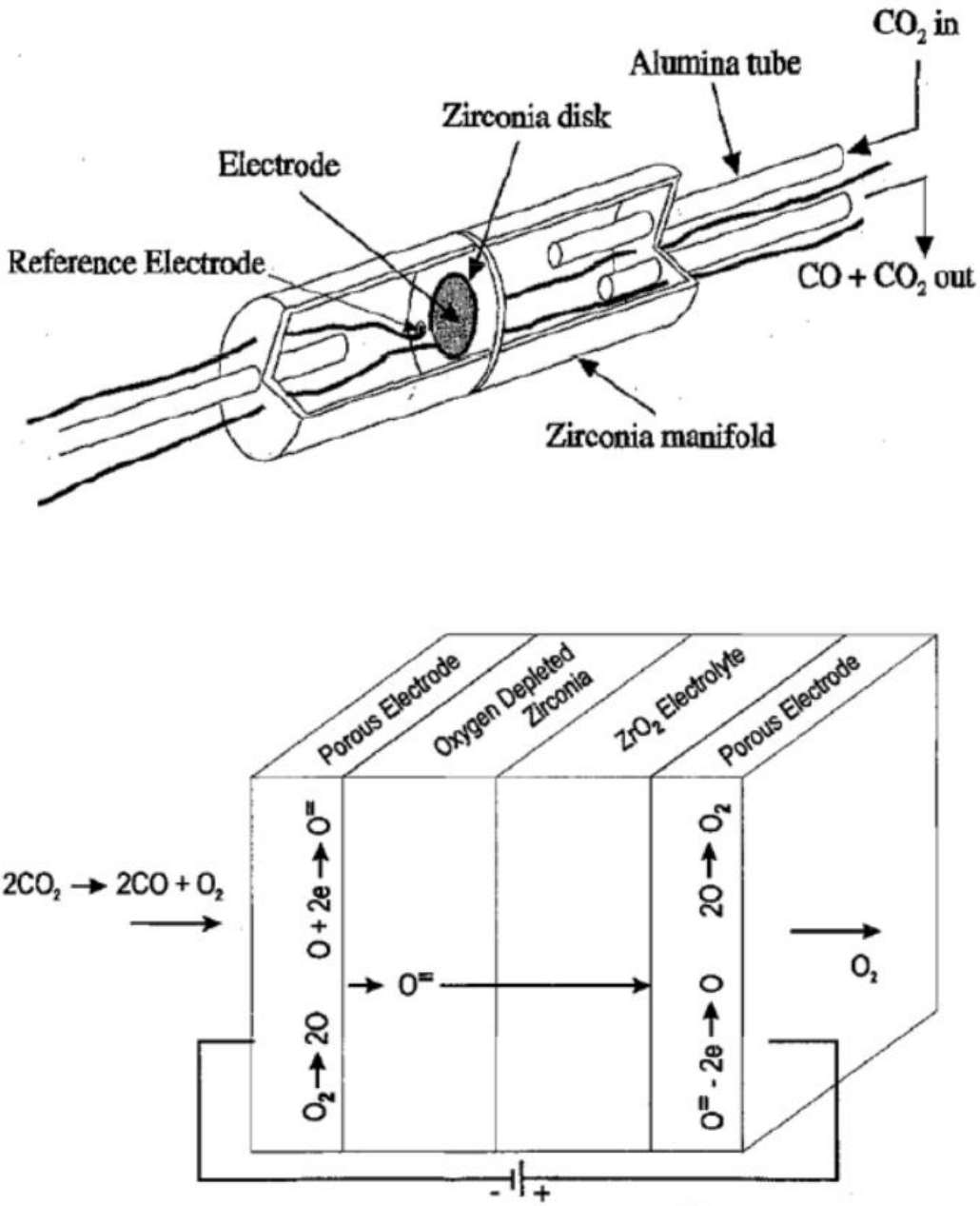

Fig. 33 Schematics of CO_2 decomposition system using zirconia membrane and electrochemical mechanism [27].

Generally, significantly high energy is required for CO_2 dissociation because CO_2 is a very stable molecule. The thermal decomposition ratio of CO_2 is known as approximately 0.2% at 1400°C, which is too low to be commercialized. Thus, researches on the direct thermolysis of CO_2 to improve the CO_2 dissociation has been performed at 2,000°C [45]. On the other hand, G. Chen et al. [50] reported that vibrational excitation was the most effective for CO_2 dissociation because the ideally minimal energy was required to perform the process.

The recent literatures have suggested that plasma can improve the strength and efficiency of chemical reactions because chemically active species and the significant concentration of excited molecules can be generated. For instance, non-thermal plasma (NTP) generates high energy electrons of 1-10 eV, which is high enough for CO_2 dissociation. Notably, the plasma-assisted catalytic system provides the improved performance in terms of conversion, yield, selectivity and energy efficiency. In addition, the plasma can be combined with various packing materials and catalysts to enhance the performance such as conversion, selectivity, and energy efficiency.

In this chapter, the catalysts were evaluated for CO_2 dissociation in the plasma-catalysis system consisted of two-stage processes under the low-current arc plasma. The γ-Al_2O_3, and Ce/Al_2O_3 catalysts were prepared in this study. The effect of adding catalysts in plasma on CO_2 conversion and energy efficiency were evaluated. In addition, the mechanism of CO_2 dissociation in the plasma-catalytic system was investigated by in-situ DRIFTS spectroscopy. From this study, the effect of metal oxide catalyst was verified for the plasma-assisted catalytic CO_2 activation and the plasma can be a new alternative for CO_2 decomposition as a high conversion rate and energy efficiency were achieved.

4.2.1 Plasma-assisted catalytic CO_2 conversion experiment

Catalyst preparation: The catalysts were synthesized by a wet impregnation method. The γ-Al_2O_3 was used as support. The Ce was loaded on γ-Al_2O_3 using the wet impregnation method. The Ce was loaded with 10 wt.% of the total weight of the catalyst support. In detail, $CeCl_3$-$7H_2O$ was added to deionized water and was stirred at room temperature for 1 hour. Then, the precipitates were dried at 70°C for 20 hours, and subsequently calcined at 400°C for 4 hours (0.5°C/min).

Characterization of catalyst: The prepared catalysts were characterized by in-situ DRIFTS spectroscopy. In-situ FTIR spectrum of absorbed species on catalysts under the CO_2-excited plasma was recorded using the same equipment with Chapter 4.1 and the experiment was carried out in the same condition.

Evaluation of plasma-catalytic performance: The plasma-assisted catalytic CO_2 conversion was performed in an arc plasma reactor as depicted in Fig. 34. The CO_2 conversion was evaluated according to the temperature up to 200°C. The CO_2 and He were injected by 800 ml/min and 2,500 ml/min, respectively. The catalysts of 4.3 g were packed in the plasma reactor. To evaluate the performance of the low current arc plasma, CO_2 conversion (X_{CO_2}), SEI and energy efficiency (η) were defined as follows [45]:

$$X_{CO_2}(\%) = \frac{CO_2\,decomposed\,(mol/\min)}{CO_2\,produced\,(mol/\min)} \times 100 \quad (5)$$

$$SEI(kJ/L) = \frac{Discharge\,power(kW)}{Flow\,rate(L/\min)} \times 60(s/\min) \quad (6)$$

$$\eta(\%) = \frac{CO_2\,flow\,rate(mol/\min) \times X_{CO_2}(\%) \times \triangle H^{\circ}{}_{298K}(kJ/mol)}{Discharge\,power(kW) \times 60} \quad (7)$$

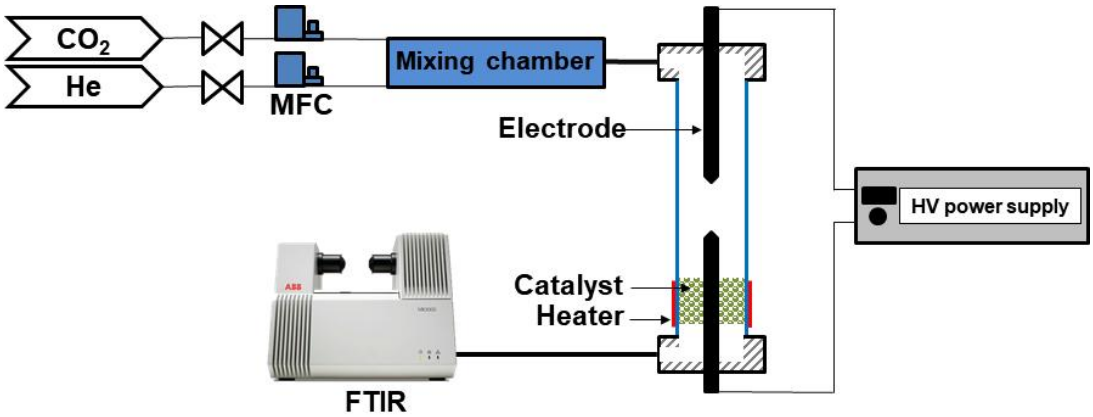

Fig. 34 Schematic diagram of experimental setup for the CO_2 conversion.

4.2.2 Results and discussion

In-situ DRIFTS spectroscopy was performed to investigate the interaction of CO_2 with the γ-Al_2O_3 under plasma in detail. In addition, the effect of the presence of the active catalytic component (i.e., Ce) on CO_2 conversion was investigated. First, it was observed that the effect of temperature on the interaction of CO_2 with the γ-Al_2O_3 without plasma. All catalysts were reduced at 400°C in 2 vol.% H_2/He flow of 100 mL/min for 2 hours on the above apparatus. After cooling down to room temperature, the catalysts were heated up to 400°C with 5°C/min in 9 vol.% CO_2/He flow of 550 mL/min, and then IR spectrum was collected at 25°C, 100°C, 200°C, 300°C and 400°C, respectively. The IR spectra of γ -Al_2O_3 in the absence of plasma is shown in Fig. 35. The band corresponding to CO_2 was observed at 3726 (v_1+v_3), 3626 ($2v_2$+v_3) and 2338 (v_3) cm^{-1}.

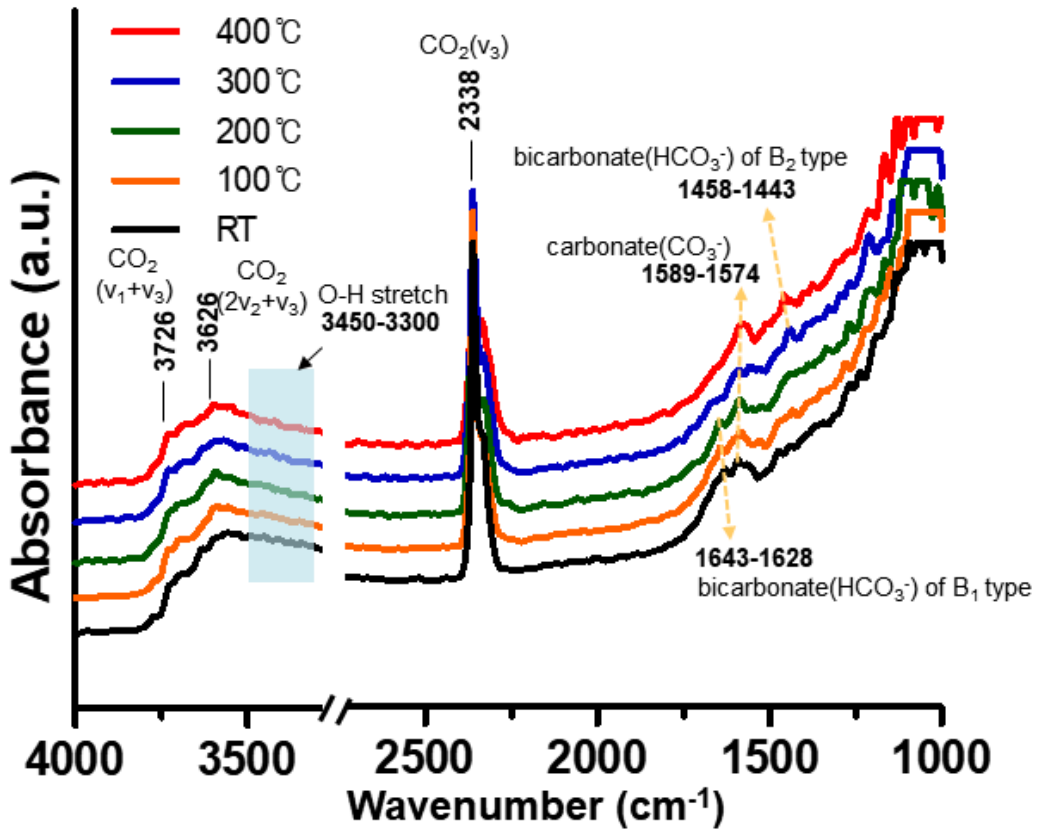

Fig. 35 IR spectra of γ-Al_2O_3 in the absence of plasma.

As well known, the carbonate formation requires a high temperature higher than 200°C. However, although the species can be formed as various structures such as carbonates and bicarbonates, the apparent identification of these species is not simple because they have similar IR bands [81]. The shoulder band on the side of 1574 cm^{-1} was reduced as increasing the temperature, and nearly disappeared at 400°C. In addition, the band of 1458 cm^{-1} appeared at 300°C. These changes in the band at 1574 and 1458 cm^{-1} implied the formation of bicarbonates [82].

The in-situ DRIFTS spectra of γ-Al_2O_3 according to the temperature in the presence of plasma is indicated in Fig. 36.

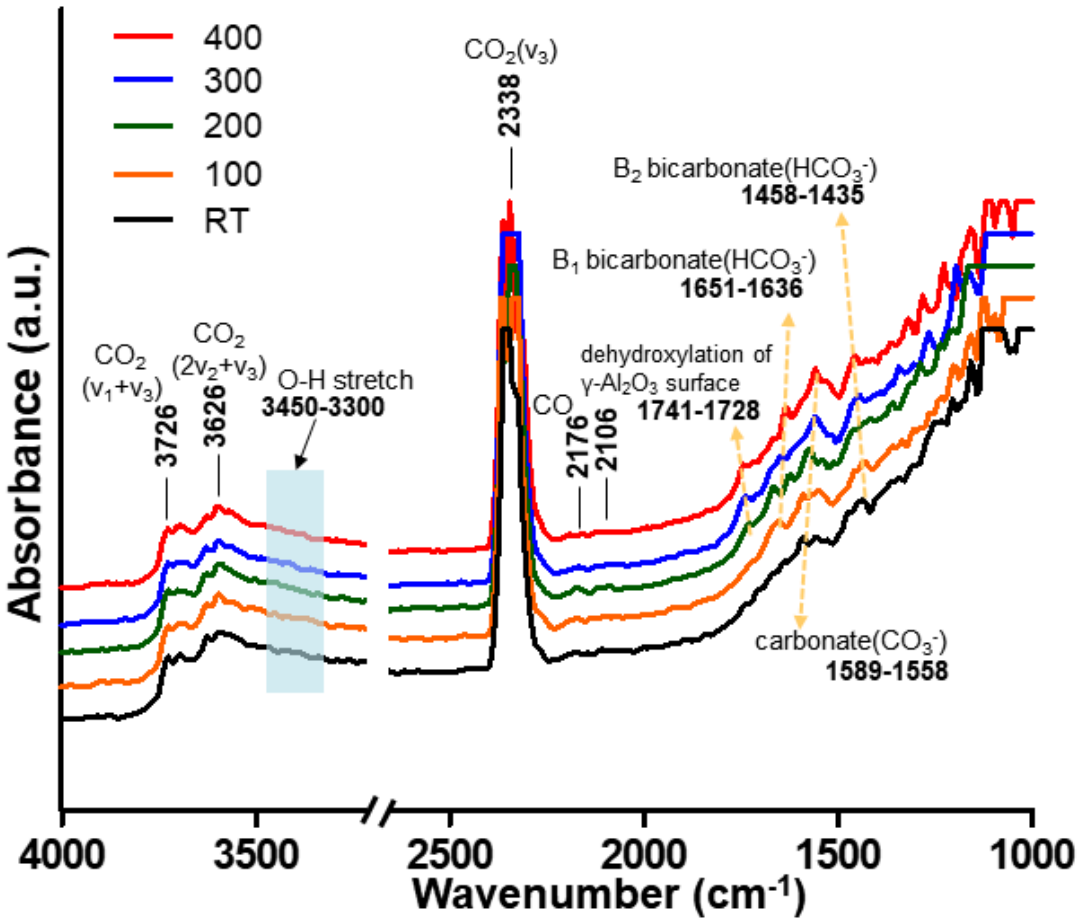

Fig. 36 IR spectra of γ-Al_2O_3 in the presence of plasma.

At the 1400-1800 cm^{-1}, the various changes of the IR spectrum are observed after the plasma on. Differently from the absence of plasma, the band of 1458 cm^{-1} corresponding to bicarbonate that appeared at high temperatures above 400℃ was observed at room temperature. At 300℃, the shoulder band on the side of the 1558 cm^{-1} was disappeared and the new band of 1636 cm^{-1} appeared. Besides, the new band of centered at 1651 cm^{-1} that appeared at 200℃ was red shifted to the centered at 1744 cm^{-1} as the temperature increase up to 400℃. The bands at around 1744 and 1636cm^{-1} are corresponding to conversion to different types of bicarbonate by plasma-excited CO_2.

The change of intensity of CO_2 and CO bands compare with room temperature depending on temperature was indicated in Fig. 37. The intensity of the CO_2 bands at 3726 and 3626 cm^{-1} was reduced by 5.56% and 6.25%, respectively, at 400℃. The intensity of the CO band at 2176 cm^{-1} was improved as 33.33% at 200℃.

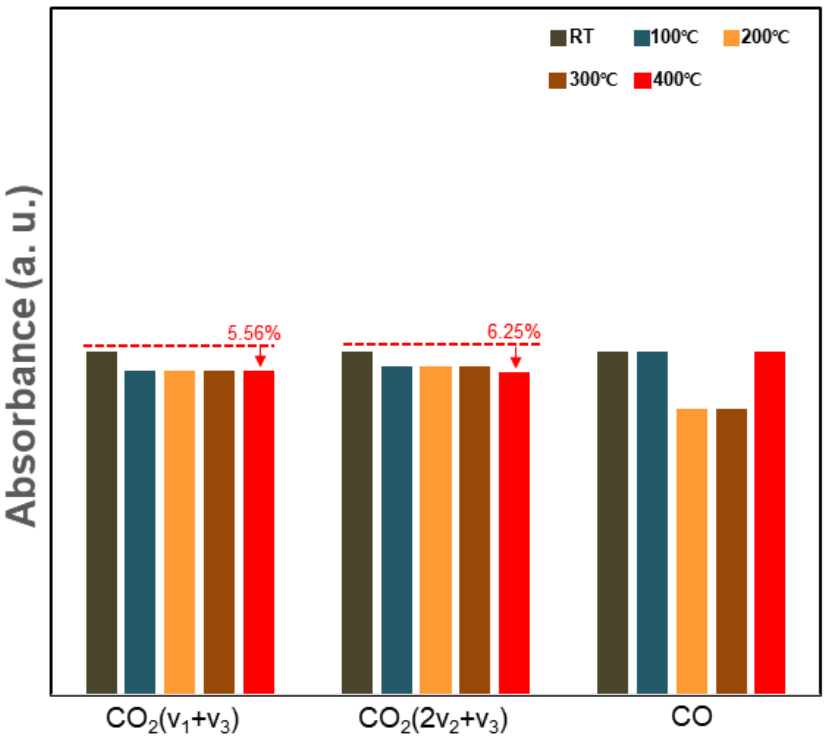

Fig. 37 The change of intensity of γ-Al_2O_3 depending on the temperature in the presence of plasma

The interaction of CO_2 with the Ce/Al_2O_3 catalyst was investigated. All samples were pretreated in the same method as Al_2O_3. As shown in Fig. 38, the IR features observed for Ce/Al_2O_3 catalyst represent adsorbed species similar to the ones that detected for the Al_2O_3 support, i.e., adsorbed CO_2 (3726, 3626, 2338 cm^{-1}) and carbonates (1582, 1535 cm^{-1}). However, at all temperatures, notable IR changes of CO_2 interaction with Ce particles were not observed, which means that the conversion and formation of carbonation had not

occurred. It is because of the large amount of Ce particles occupy a significant fraction of the surface and prevent the formation and conversion of carbonates on the alumina surface.

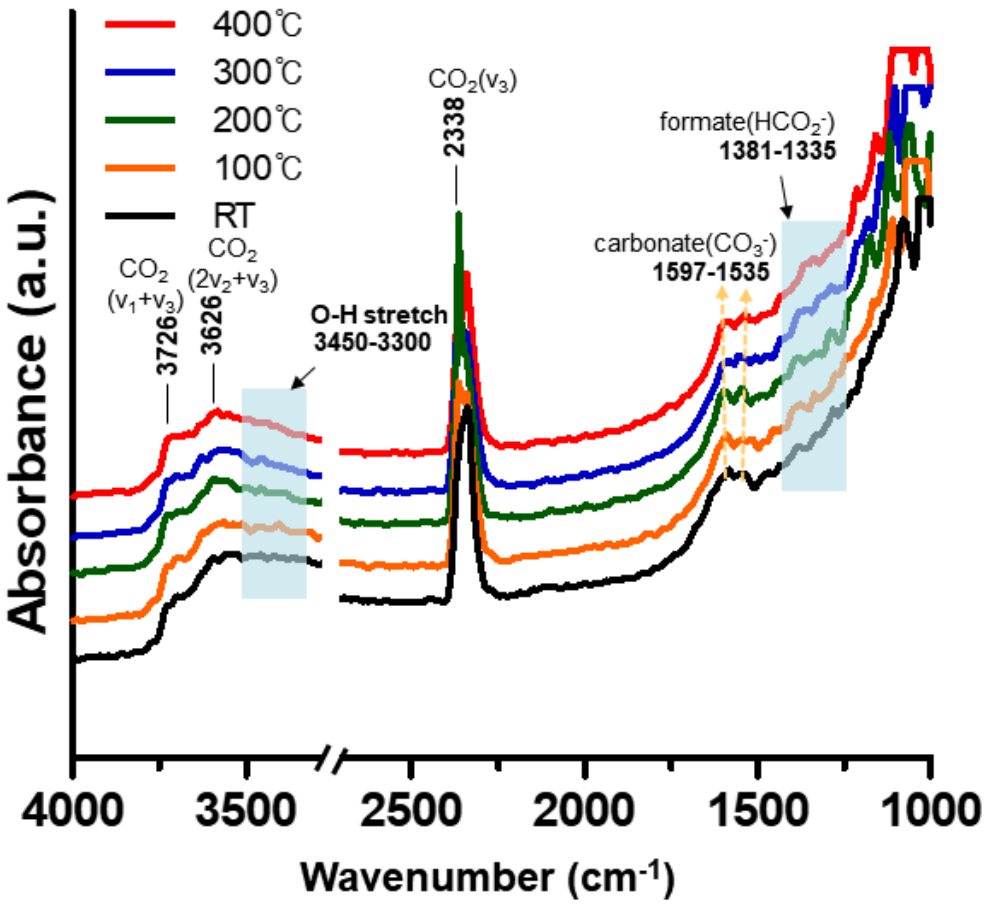

Fig. 38 IR spectra of Ce/Al_2O_3 in the absence of plasma.

In the in-situ DRIFTS spectra of Ce/Al_2O_3, depending on the temperature in the presence of plasma, the intensity change was indicated in Fig. 39. In the presence of plasma, we observed a remarkable change on the surface of Ce/Al_2O_3. The band at 1600-1500 cm^{-1} corresponding to carbonate were disappeared at 300℃, while the new band at 1373 and 1327 cm^{-1} were formed, which can be attributed to the formate species [83]. The cerium promoted catalyst can be an enhancement of the formation of intermediate formate species

[83-85].

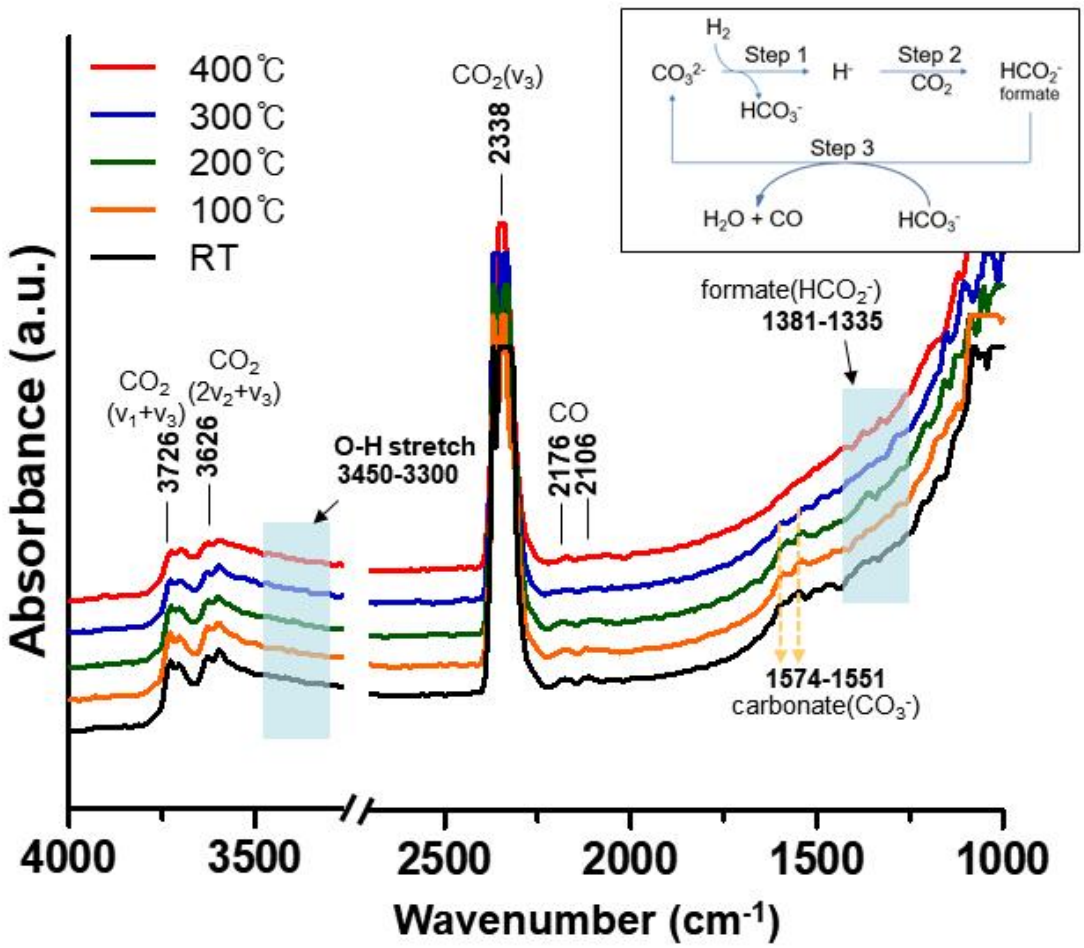

Fig. 39 IR spectra of Ce/Al_2O_3 in the presence of plasma.

The change of intensity of CO_2 and CO bands compare with a room temperature of Al_2O_3 depending on temperature was indicated in Fig. 40. The intensity of the CO_2 bands at 3726 and 3626 cm^{-1} was reduced by 27.78% and 39.58%, respectively, at 400℃. The intensity of the CO band at 2176 cm^{-1} was improved as 66.67% at 100-200℃. Consequently, doped Ce on the surface of Al_2O_3 prevents the formation of carbonate (bicarbonate), which becomes free and accessible for CO_2 adsorption. In addition, we

observed the new band attributed to the formate species, confirmed the cerium promoted catalyst can be an enhancement of the formation of intermediate formate species by the plasma-excited CO_2. Notably, as step 3 in Fig. 24, these formed intermediate species could be encouraged the generation of CO by the reaction of formate and bicarbonate.

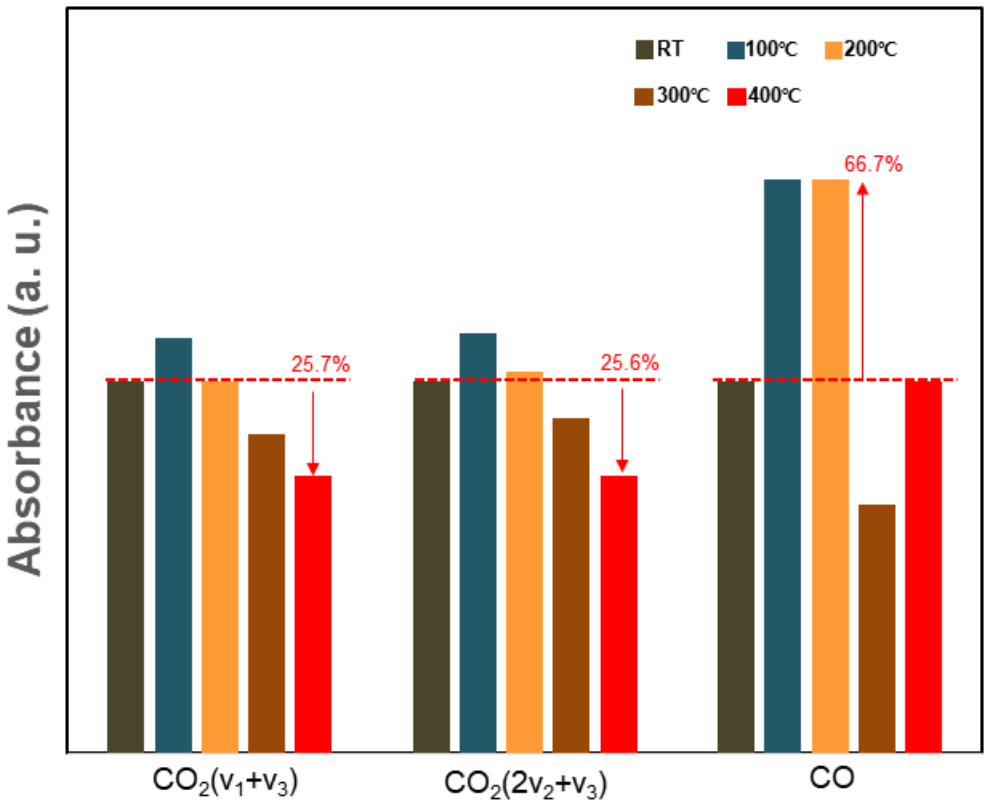

Fig. 40 The change of intensity of Ce/γ-Al_2O_3 depending on the temperature in the presence of plasma

Table 5 shows the compared recent study of the CO_2 decomposition and energy efficiency using different plasma systems. DBDs are among the most broadly studied for CO_2 conversion because of the merit of easy operation and it can provide reasonable conversions of up to 40%, but the energy efficiency remains too low as below 10 %. As reported of A. Zhou [53], a notable result was obtained highly CO_2 conversion of 52.1 %

in the ZrO_2 packed DBD reactor, but energy efficiency is too low as 7%. In DBDs, the main reaction of CO_2 splitting is dominated by electron-impact excitation followed by dissociation, not vibrational excitation, thus commonly energy efficiency shows limited below 10% [4, 23]. H. Zhang et al. [67] studied the conversion of CO_2 performed in a rotating gliding arc plasma. Notably, the effect of additive gases (N_2 and Ar) has been investigated on the reaction performance. They reported the enhanced CO_2 conversion when CO_2 was diluted with Ar or N_2, but the CO_2 conversion and energy efficiency are still too low as 4.4% and 10.5 %, respectively. T. Nunnally et al. [66] achieved a maximum energy efficiency of 35% in an atmospheric pressure GAP for CO_2 conversion. This result shows significantly better than other general thermal arcs, while the maximum CO_2 conversion is very low as 8.6%.

In this study, we achieved a reasonable value of CO_2 conversion and energy efficiency as 20.34% and 42.93%, respectively, in the arc reactor packed with Ce/Al_2O_3. CO_2 and He were injected as 800 mL/min and 2,500 mL/min, respectively, and the input power was supplied as 72.9W. From the DRIFTS experiment of the Ce/Al_2O_3 catalyst, the catalyst bed was heated to 200℃ due to the highest CO produce rate at 200℃, and we gained a high CO produce rate as 104.01 mL/min.

Table 6 Comparison of different plasma-catalyst system performance.

Type	**Arc plasma**	**GA**	**GAP**	**DBD**
Catalyst	Ce/Al_2O_3	-	-	ZrO_2
Gas mixture	24 Vol. % CO_2/He	30 Vol. % CO_2/He	CO_2	CO_2
Conversion (%)	20.34	4.4	5.1-8.6	52.1
Energy efficiency (%)	42.93	10.5	30-35	7.0
Reference	This work	[67]	[66]	[53]

Ⅴ. Metal fuel ignition system

5.1 Propellant studies for MAV

Although the use of a high oxidizer to fuel ratio (O/F) decreases the engine performance, a higher O/F ratio means that less mass is required to be brought from Earth. Thus, many researchers investigated the rocket system of high O/F to reduce the required rocket system mass. Among the several possible propellants for MAV, paraffin and hydroxyl-terminated polybutadiene (HTPB) were considered in many studies because that has been successfully used in large hybrid rocket engines [86-91].

Chandler et al. [80] studied the hybrid rocket for a MAV using a paraffin-based fuel and a mixture of nitrous oxide (N_2O) and oxygen (O_2) as an oxidizer. This propellant can good performance in a harsh low-temperature Mars environment. In addition, to increase the Isp The hybrid rocket system is possible to the reduction of mass over the baseline design up to 30% because it has a higher performance and does not require thermal conditioning. However, this propellant is to be brought from Earth.

G. A. Landis et al. [90] performed the design study of a hybrid rocket for MAV, using oxygen generated in-situ on Mars with HTPB. They considered additives to increase the specific energy of combustion such as aluminum (Al), lithium (Li), aluminum hydride (AlH_3), lithium-aluminum hydride ($LiAlH_4$), lithium borohydride ($LiBH_4$) and decaborane ($B_{10}H_{14}$). Although AlH_3, $LiAlH_4$, and $LiBH_4$ produce higher potential Isp, these additives required a lower O/F ratio. As a result, the mass of the propellant to bring from Earth increases. They analyzed performance for the LOX/HTPB-decaborane propellant at high O/F of 2.8 to minimize the weight of the propellant to be brought from Earth.

5.2 The technology of metal fuel ignition

In previous studies, they assume that CO_2 is the only available resource on Mars. As mentioned in chapter 1, however, the martian soil contained a lot of metals such as Mg, Al. In particular, it is well-known that aluminum is the use of additives to the fuel to increase the specific energy of combustion, it has a high energy density of 15.485 kJ/g

[92-98]. However, when almost metals come into contact with oxygen in the atmosphere, an oxide layer is formed on the surface of their particles. Particularly, aluminum oxide (Al_2O_3) has a melting point of >2,000°C and its structure is too dense for the oxidizing agent to contact with aluminum in the oxide layer [96]. As in show Fig. 41, the combustion of aluminum is subjected to a complicated ignition process as follows. First, aluminum in the oxide layer is melted, causing cracks generated on the oxide layer due to the thermal expansion of aluminum. However, the oxide layer is regenerated by a heterogeneous surface reaction taking place in the cracks generated at this time. As the process is repeated, when the particles reach the melting point of the oxide layer, the melted oxide layer forms a cap. Subsequently, the ignition process is finished and the combustion is initiated [105, 106]. This complex ignition mechanism of aluminum requires a lot of energy for the initial ignition, which reduces the efficiency of the entire propulsion system. In order to solve this problem, many researches have been conducted focusing on reducing the aluminum ignition temperature and accelerating the ignition process such as an additive coating with aluminum powders [101, 102] and a hydrogen torch ignition method [97].

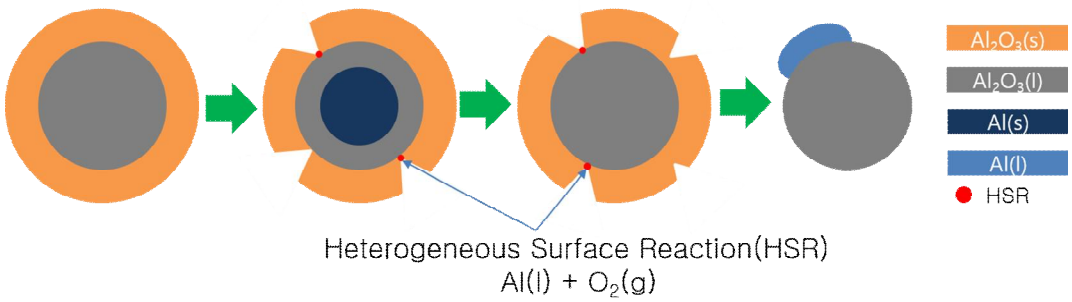

Fig. 41. Ignition process of aluminum particle

Li et al. [101] studied the ignition of aluminum powders with adding sodium borohydride ($NaBH_4$) by injecting steam at 500°C. When the steam was injected, $Na_2[Al_2O_3(OH)_2]\cdot 1.5H_2O$ was produced by reacting 2 moles of NaOH generated by $NaBH_4$ hydrolysis reaction with 1 mole of Al_2O_3 and 1.5 moles of H_2O. This reaction caused the

removal of the oxide layer on aluminum and then the aluminum was able to be ignited with steam at 500°C. Even though this mechanism was effective to reduce the ignition temperature, much energy was still needed to generate the steam of 500℃. In addition, $NaBH_4$ was decomposed thermally at 500°C before NaOH was reacted with Al_2O_3, making it difficult to meet the condition for the reaction of NaOH with Al_2O_3. As an alternative method in order to control the ignition temperature of aluminum, the aluminum particles can be coated with nickel to prevent the oxide layer from growing on the aluminum after their oxide layer was removed. It was reported that the energy generated from the enthalpy difference between the reactant and product was accumulated in the nickel-aluminum particles during the sintering reaction. The energy source in the particle was effective to reduce the ignition delay and the ignition temperature. Noh et al. [102] has conducted the nickel coating on the aluminum particles and disclosed that the ignition delay of aluminum combustion was shortened by 40% and the ignition temperature decreased down to 1,450°C because of the nickel-aluminum sintering reaction. However, the temperature higher than 1,000°C is still required and the nickel coating process makes it complicated and difficult the manufacturing process of the metal fuels. Miller et al. [103] suggested the hydrogen torch ignition method of spraying aluminum powders into a hydrogen/oxygen flame with a high temperature of 3,200°C. This method has the merit of using pure aluminum powders without any additives. In addition, the aluminum powders were possible to be ignited within 5 sec because the spark was used for the hydrogen ignition [104]. In recent, the hydrogen torch ignition method has been widely studied because of its simplicity and rapid ignition. However, a high-pressure storage tank for supplying the hydrogen is required, making it heavy and bulky the combustion system.

The conventional hydrogen torch ignition systems normally employed the liquefied or compressed hydrogen [105]. However, hydrogen needs excessive energy to be liquefied and suffers from boil-off during charge and storage [106]. The compressed hydrogen must be stored in a high pressure due to its low volumetric density, making it heavy the hydrogen tank. In order to solve the aforementioned problems, a hydrogen combustor using the solid-state $NaBH_4$ instead of the hydrogen storage tank was proposed for the ignition of aluminum powders in this study. The hydrogen was generated and auto-ignited by the thermal decomposition of $NaBH_4$. Finally, the ignition of aluminum powders was performed

using the proposed hydrogen combustor, which is simpler and lighter than conventional systems using the liquefied and compressed hydrogen because no high-pressure tank and gas lines for supplying hydrogen are required.

In the present study, the ignition of aluminum powders using the hydrogen combustor based on the solid $NaBH_4$ thermal decomposition was carried out. Characteristics of the hydrogen combustor were investigated by evaluating the hydrogen generation rate through the thermal decomposition of $NaBH_4$ as the air supply rate was varied. From the results, the optimum condition for the ignition of aluminum powders was determined. Based on the characteristics of $NaBH_4$ thermal decomposition, the aluminum ignition was carried out to verify the applicability of the proposed method for the ignition system of aluminum powders.

5.3 Design and Experimental

5.3.1 Concept of the proposed ignition system of aluminum powders

In this study, a solid $NaBH_4$-based hydrogen combustor was proposed for the ignition of aluminum powders. First, the $NaBH_4$ is thermally decomposed to generate hydrogen and then the hydrogen is ignited when it reaches the auto-ignition temperature. Next, aluminum powders are sprayed to the high-temperature hydrogen flame, resulting in the removal of aluminum oxide film. The aluminum powders whose oxide film is removed are ignited with air in the pre-combustion zone. Subsequently, the aluminum powders are combusted with oxidizer in the main combustion zone.

$NaBH_4$ has been widely used as a hydrogen source because of its high hydrogen storage density of 10.6% [107, 108]. The hydrogen can be generated from $NaBH_4$ by a hydrolysis [109] and a thermal decomposition [110]. However, the $NaBH_4$ hydrolysis requires the addition of H_2O as well as separate devices such as a pump and valve so it is not suitable for the ignition system. Other than the hydrolysis, the hydrogen can be extracted directly from the solid-state $NaBH_4$ by the thermal decomposition as expressed in Eq. 8. When $NaBH_4$ is thermally decomposed, solid phase byproducts are compounds of Na and B, whereas a gaseous product is only hydrogen [110].

$$NaBH_4 \rightarrow \Sigma solid(Na,\ B) + xH_2(x \leq 2) \quad (8)$$

Basically, $NaBH_4$ is thermally decomposed by heating up to its boiling point of 500°C. Pascal et al. [110] reported that the thermal decomposition of $NaBH_4$ was activated under the condition of 1 bar and 534±10°C. Subsequently, the hydrogen was released and immediately ignited because its auto-ignition temperature is 500℃. Therefore, a simple hydrogen combustor through the $NaBH_4$ thermal decomposition can be designed without separate devices for ignition. Table 6 shows properties of $NaBH_4$.

Table. 7 $NaBH_4$ properties

Melting point [℃]	**Boiling point [℃]**	**Thermal decomposition Temp. [℃]**	**H_2 storage density [wt.%]**	**$\triangle_f H$ [kJ/mol]**
400	500	534±10 (at 1bar)	10.6	-191 (T=300K)

5.3.2 Solid $NaBH_4$-based hydrogen combustor

Experimental setup for the ignition of aluminum powders assisted by the hydrogen combustion based on the $NaBH_4$ thermal decomposition is shown in Fig. 42. First, the $NaBH_4$-based hydrogen combustor was designed. After grinding the solid-state $NaBH_4$ to be powdered, the powders were pressed under the pressure of 26.8 N/mm^2, making a cylindrical grain of which the diameter and length were 21.8 and 30mm. After then, a hole of 13mm in diameter was made in the center to obtain a hollow grain. The prepared grain of 30 g was filled into the combustor and a SiN ceramic heater (FKK) was installed at the front of the grain for heating the $NaBH_4$ grain as shown in Fig. 42 (a). The heat flux of heater was controlled by adjusting an applied voltage through a voltage regulator. From the preliminary test, it was confirmed that the temperature was raised to 1,000°C within 5 sec by applying a power of 65 W [111].

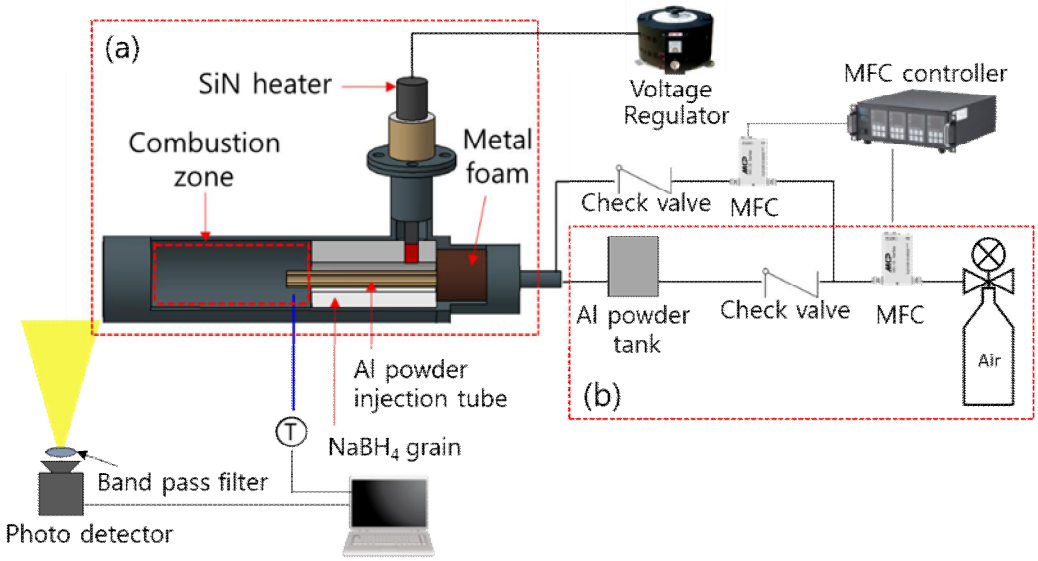

Fig. 42. Experiment setup for the ignition of aluminum powders assisted by the hydrogen combustion based on the $NaBH_4$ thermal decomposition, including (a) $NaBH_4$-based hydrogen combustor and (b) aluminum powder injector.

When the heater turned on, the grain was locally heated around the heater, at which the $NaBH_4$ thermal decomposition was initiated, generating hydrogen. The heater was heated up to 1000℃ within 5 sec but it was maintained for 25 sec at which the combustor temperature reached 500℃ because the heat should be propagated though the grain. The heater turned off after the hydrogen flame was generated. The hydrogen was auto-ignited immediately after generated but the equivalent ratio would be low (rich burn) and the flame was sustained on the inner surface of grain. The air as an oxidant was supplied to control the equivalent ratio and to move the flame into the combustion zone. The air supply rate was controlled by a mass flow controller (VIC-D220). A check valve was installed in the inlet of combustor to block the backflow due to the sudden increase of pressure in the combustor when the large amount of hydrogen was instantaneously generated by the $NaBH_4$ thermal decomposition. In addition, in order to prevent the backfire of hydrogen flame from propagating, a nickel foam having a pore diameter shorter than the hydrogen quenching distance was installed between the grains and check valve.

As aforementioned, the $NaBH_4$ thermal decomposition was initiated locally in the part of

grain contacting with the heater. After the hydrogen was ignited and the air was supplied, the $NaBH_4$ thermal decomposition was propagated into the entire region because of the heat of hydrogen combustion. Therefore, the air supply rate played a role to determine characteristics of $NaBH_4$ thermal decomposition. The temperature change in the combustor and the thermal decomposition time of $NaBH_4$ grain were measured according to the air supply rate in the range of 30-50 L/min. In order to calculate the thermal decomposition efficiency of $NaBH_4$, the undecomposed portion of $NaBH_4$ in the grain should be known but it was difficult to be separated from the grain residue after the thermal decomposition. Thus, the amount of hydrogen generation from the hydrolysis of grain residue was measured because the hydrogen must be generated as much as the undecomposed portion of $NaBH_4$ remained in the grain after the thermal decomposition. Fig. 43 shows the schematic of the hydrogen generator system for measured the undecomposed portion of $NaBH_4$ remained in the grain after the thermal decomposition. It was reported that 97% of $NaBH_4$ was converted into hydrogen and other byproducts by reacting with 3 M HCl solution [112]. A simple hydrolysis reactor was prepared to measure the amount of hydrogen generated from $NaBH_4$. After the thermal decomposition, the grain residues were packed into the reactor and 3 M HCl solution was injected using a syringe pump. The hydrogen generation rate was measured by a mass flow meter after removing moisture contained in the hydrogen gas. The thermal decomposition efficiency of $NaBH_4$ was calculated using Eq. 9.

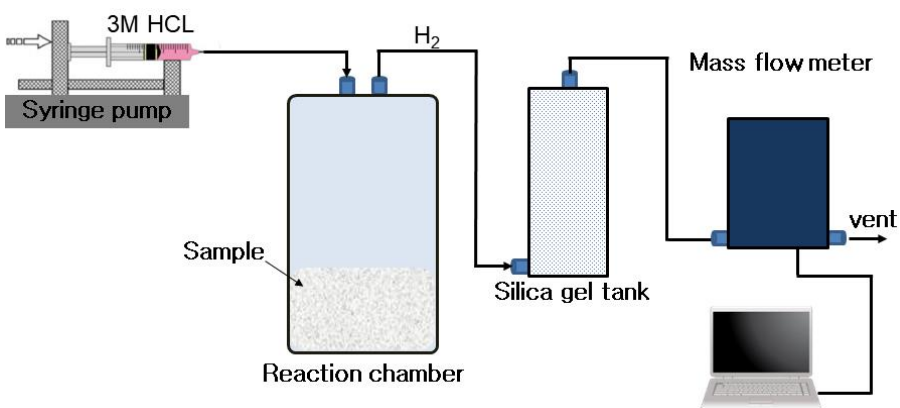

Fig. 43. Schematic of the hydrogen generator system

$$\eta_{td} = 1 - \frac{V_{grain\,residue}}{V_{fresh\,grain}} \tag{9}$$

where η_{td}, $V_{grain\ residue}$, and $V_{fresh\ grain}$ are the thermal decomposition efficiency of $NaBH_4$, the measured amount of hydrogen generated from the grain residue, and the theoretical amount of the hydrogen that can be generated from fresh $NaBH_4$ grain.

5.3.3 Aluminum powder injector

Aluminum powders should be injected at the constant rate into the hydrogen combustion zone for the stable ignition of aluminum powders. For this purpose, a powder injector with a rotating screw that is capable of uniformly spraying aluminum powders was developed as shown in Fig. 44.

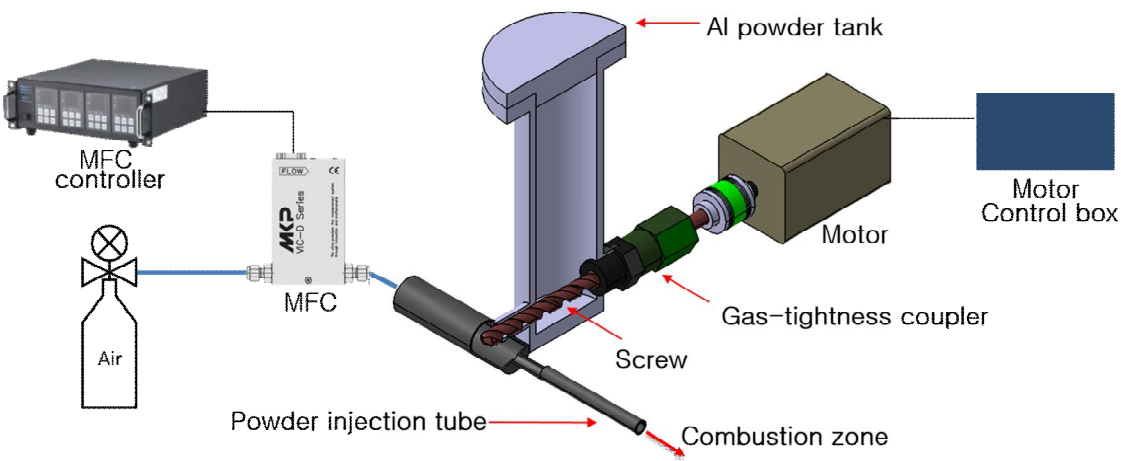

Fig. 44. Aluminum powder injector with a rotating screw

Generally, aluminum powders with a submicron particle size have been used because of its thin oxide layer that can be broken by applying a relatively low energy, but their handling and maintenance were dangerous due to its sensitivity even to atmospheric air. In this study, aluminum powders of 44 μm in the particle size (Duksan Pure Chemicals) were used taking the safety and easiness to handle into consideration. The powders were

filled in the powder chamber and transferred into the injection tube by rotating a screw. Then, air as a carrier gas was supplied into the injection tube so that the powders with the air were injected into the combustion zone. The screw with 9 mm in diameter and 10 mm in pitch was located in the lower end of the powder chamber, and the air supply rate was controlled by the mass flow controller. A motor was connected to the screw jointing a gas-tightness rotary coupler in between them. The powder injection rate was varied by controlling the rotating speed of screw and the air supply rate in the range of 20-60 rpm and 30-60 L/min, respectively, and was evaluated by measuring the weight of aluminum powders collected in the separate collector using a precision scale with resolution of 0.001g. The filter with a permeable pore size of 2.5 ㎛, which is smaller than the aluminum powder size of 44 ㎛, was installed in the collector so that all of aluminum powders was accumulated in the collector. The change in the weight of the collected powders was recoded at an interval of 5 sec.

5.3.4 Ignition of aluminum powders

Ignition of aluminum powders was performed by the $NaBH_4$-based hydrogen combustor. The ignition process mainly consists of the auto-ignition of hydrogen generated from the thermal decomposition of $NaBH_4$ and the injection of aluminum powders in the hydrogen flame. The developed aluminum powder injector was connected to the $NaBH_4$-based hydrogen combustor as shown in Fig. 42 (b). The powder injection tube was installed in the combustion zone of the $NaBH_4$-based hydrogen ignition system through the center hole of the grain. Thus, the aluminum powders were injected coaxially with the direction of hydrogen flame propagation to improve the combustion efficiency of the aluminum.

A temperature sensor was installed inside the combustor to measure the change in temperature when the aluminum powders was ignited. In addition, AlO species of the aluminum flame was detected using a photodiode (DET10A2, THORLABS). The AlO was a main intermediate species of the aluminum combustion that can be used to evaluate the characteristics of the ignition and combustion of aluminum. The characteristic spectrum of AlO was composed of overlapped peaks in the wavelength between 450 and 550 nm. In particular, the highest intensity of peak was observed at 486 nm [113]. The AlO spectra

were selectively detected by using a band pass filter.

5.3 Results and discussion

5.3.1 $NaBH_4$ thermal decomposition

The total thermal decomposition time of $NaBH_4$ and the temperature change of the combustor according to the air supply rate are shown in the Fig. 45. The surface temperature of the heater was raised up to 1,000°C within 5 sec for the rapid thermal decomposition of $NaBH_4$. The thermal decomposition was initiated from the $NaBH_4$ in contact with the surface of the heater, immediately generating the hydrogen gas. It was assumed that the $NaBH_4$ thermal decomposition was activated after the temperature increased higher than 500°C that is the thermal decomposition temperature of $NaBH_4$. Subsequently, the generated hydrogen was ignited without an ignition source because the auto-ignition temperature of hydrogen was 500°C.

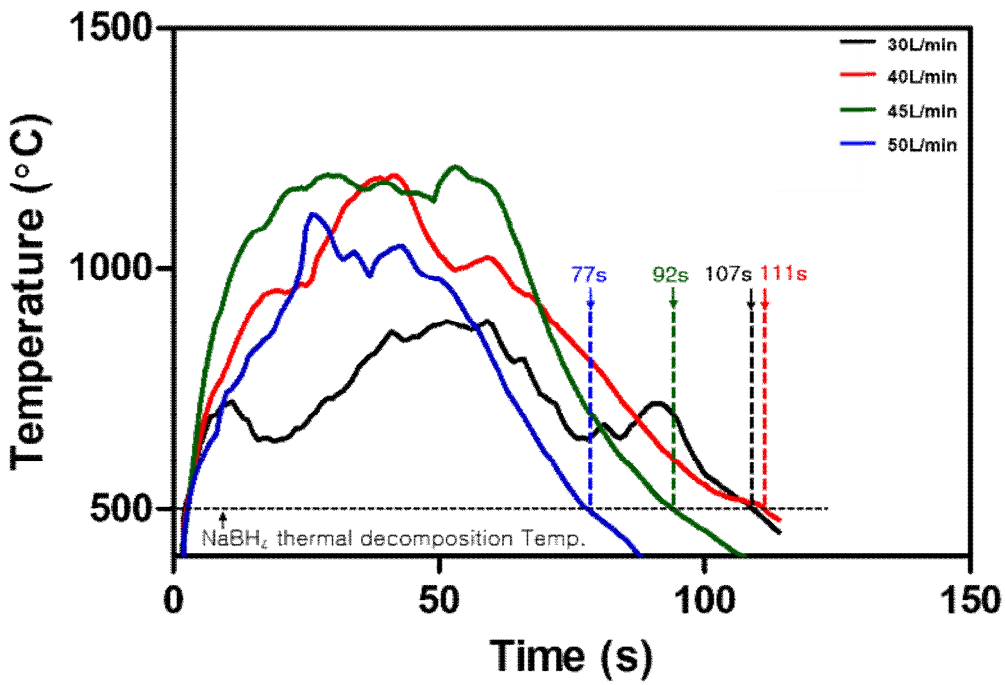

Fig. 45. Thermal decomposition time of $NaBH_4$ and the temperature change according to the air supply rate

As the hydrogen gas burned, the heat of combustion was propagated into the $NaBH_4$ grain so that the thermal decomposition of $NaBH_4$ was rapidly accelerated. Consequently, the hydrogen flame was formed in the combustion zone as shown in Fig. 42. The thermal decomposition time of $NaBH_4$ was dependent on the air supply rate. Thus, the temperature change inside the combustor as the time elapsed was measured according to the air supply rate in order to evaluate the performance of the $NaBH_4$-based hydrogen combustor. The total thermal decomposition time and the maximum temperature were presented in Table 8. Basically, the thermal decomposition time decreased as the air supply rate increased because the burning rate increased with the air supply rate. On the other hand, the maximum temperature increased with the air supply rate because the sufficient oxidant was diffused into the $NaBH_4$ grain. However, the temperature reached maximum at 45 L/min and was dropped at 50 L/min. It means that the air supply rate was faster than the regression rate of $NaBH_4$ grain.

Table 8 The total thermal decomposition time and the maximum temperature of the $NaBH_4$-based hydrogen combustor according to the air supply rate.

Air supply rate (L/min)	**Thermal decomposition time (sec)**	**Maximum temperature (℃)**
30	107	889.5
40	111	1053.7
45	92	1210.9
50	77	1114.9

The thermal decomposition efficiency of $NaBH_4$ can be calculated by dividing the actual amount of the hydrogen generated from the thermal decomposition of $NaBH_4$ with the theoretical one contained in the $NaBH_4$. However, it was difficult to measure the hydrogen generation rate because the hydrogen was burned immediately after generated. Thus, the thermal decomposition efficiency of $NaBH_4$ was calculated by Eq. 9. The each sample after the thermal decomposition at the different air supply rates was collected and the amount of hydrogen in the undecomposed $NaBH_4$ residue was measured by reacting with 3 M HCl solution. In the air supply rate of 30 L/min, the total amount of hydrogen contained in the sample of 10 g was 1.4 L and the theoretical amount of hydrogen in the $NaBH_4$ of 10 g was 26.0 L. Thus, the thermal decomposition efficiency was 95% from Eq. 9. In all cases, there was no big difference in the thermal decomposition efficiency as 95±0.5%. It means that the thermal decomposition efficiency was not dependent on the air supply rate.

The hydrogen generation rate was estimated to calculate the equivalence ratio according to the air supply rate. In 30 L/min, for example, the $NaBH_4$ of 30 g was decomposed for 107 sec and the total amount of hydrogen during the thermal decomposition would be 37.1 L as the thermal decomposition efficiency of 95% was applied. Therefore, the hydrogen generation rate was 20.8 L/min in average. Equally, the hydrogen generation rate for each air supply rate could be calculated. From the hydrogen generation rate and the air supply rate, the equivalence ratio of the hydrogen combustion using the thermal decomposition of $NaBH_4$ was obtained. The thermal decomposition time, hydrogen generation rate, and equivalence ratio of the solid $NaBH_4$-based combustor as a function of the air supply rate were presented in Fig. 46. The equivalence ratio was 1.21 in the air supply rate of 40 L/min. As the air supply rate increased from 40 L/min, the thermal decomposition time of $NaBH_4$ decreased, while the hydrogen generation rate increased with the equivalence ratio. For all of the air supply rate, the hydrogen combustion was occurred under the fuel rich condition.

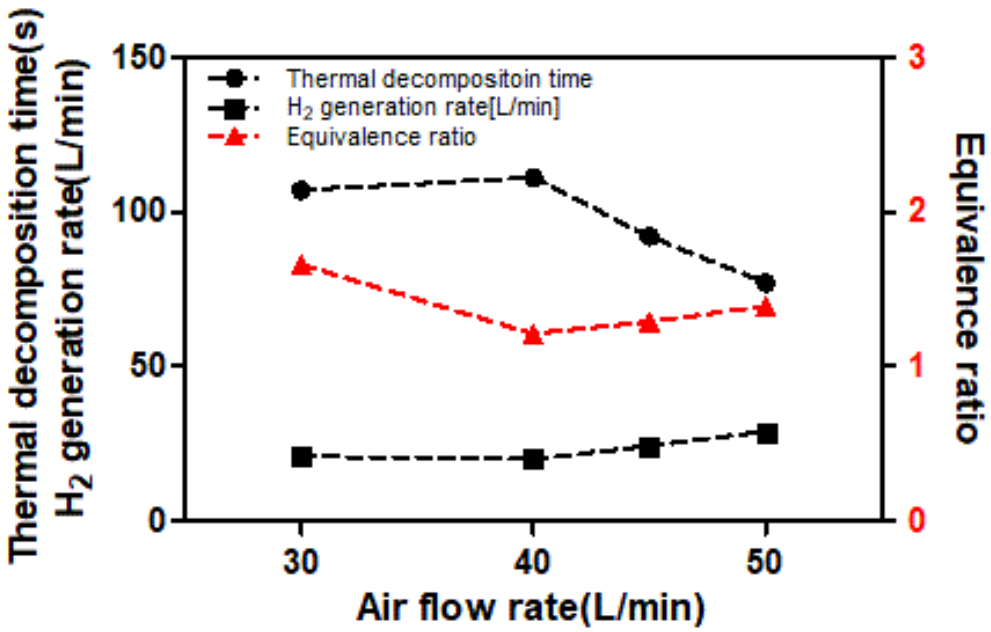

Fig. 46. Thermal decomposition time, hydrogen generation rate, and equivalence ratio of the solid NaBH4-based combustor as a function of the air supply rate (Thermal decomposition efficiency of $NaBH_4$ was assumed to 95%).

The pictures of the $NaBH_4$ grain before and after the thermal decomposition are shown in Fig. 47. The grain structure was not destroyed during the thermal decomposition. It means that the hydrogen was released the other byproducts remained in the grain.

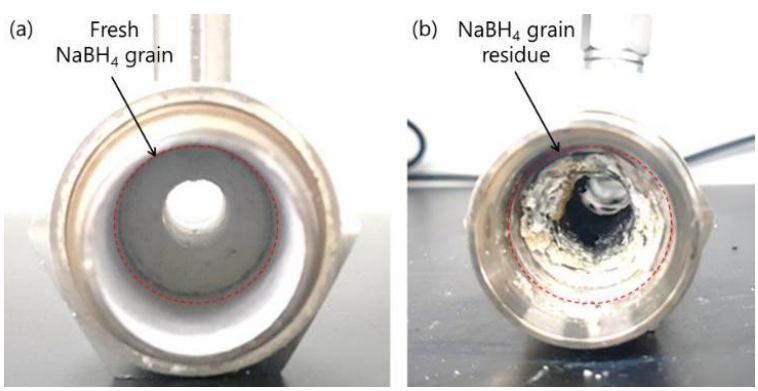

Fig. 47 Pictures of the $NaBH_4$ grain (a) before and (b) after the thermal decomposition.

5.4.2 Ignition of aluminum powders

Aluminum powders were sprayed into the combustion zone using the powder injector. The air of 5 L/min was supplied as a carrier gas to transport the aluminum powders. The equivalent ratio would be changed because aluminum powders with the additional air were injected to the hydrogen combustion zone where the equivalence ratio was 1.21. The powder injection rate was 0.849 g/min in the screw rotation speed of 20 rpm. Thus, the equivalence ratio of aluminum combustion was changed to 1.127 when the carrier gas of 5 L/min was supplied. The powder injection rate and the equivalence ratio of aluminum combustion according to the screw rotation speed are presented in Table 9. The powder injection rate was linearly increased with the screw rotation speed because the constant amount of powders was transferred by the screw rotation. The average amount of powders per revolution of the screw was 0.0289 g.

Table 9 Powder injection rate and the equivalence ratio of aluminum combustion according to the screw rotation speed.

Screw rotation speed (rpm)	Powder injection rate (g/min)	Equivalence ratio, ΦAl
20	0.849	1.127
40	0.920	1.133
60	1.268	1.158

※ For all cases, the air of 5 L/min was supplied as a carrier gas of aluminum powders.

The powder injection rate increased with the screw rotation speed, resulting in the increase of the equivalent ratio of aluminum combustion. For the ignition of aluminum

powders, the screw rotation speed of 60 rpm was selected because the equivalent ratio was close to the stoichiometric combustion. When the solid $NaBH_4$ was decomposed with the air supply rate of 40 L/min, the temperature in the combustion zone was maintained higher than 1,000°C because of the hydrogen combustion. In addition, it was confirmed that the equivalence ratio was 1.21. At this time, aluminum powders was injected with 1.268 g/min. The total air supply rate was changed to 45 L/min because the additional air was supplied as a carrier gas of aluminum powders. Thus, the final equivalence ratio was 1.158.

The ignition of aluminum powders was performed under the aforementioned condition. The $NaBH_4$ thermal decomposition was initiated and subsequently the hydrogen auto-ignition was occurred. After the hydrogen combustion was stabilized, aluminum powders were injected into the combustion zone using the powder injector. The pictures of the solid $NaBH_4$-based hydrogen combustion and the ignition of aluminum powders are shown in Fig. 48. The change of flame color could be observed before and after the injection of aluminum powders. At the hydrogen combustion in Fig. 48 (a), the flame color showed the strong yellow light, while after aluminum powders were injected, the length of flame became longer and the white light appeared at the center of the flame as shown in Fig. 48 (b).

The temperature change inside the combustion zone with and without the injection of aluminum powders, and the signal of AlO radicals from the photodiode during the combustion are shown in Fig. 49. After the $NaBH_4$ thermal decomposition was initiated, the temperature higher than 500°C was maintained by the hydrogen combustion for 111 sec. On the other hand, the combustion could be sustained by injecting aluminum powders for 157 sec. It means that the aluminum combustion was activated even after the $NaBH_4$ thermal decomposition was terminated. The result showed the temperature of aluminum combustion was lower than that of hydrogen combustion. However, it was because the thermocouple was installed in the exit of $NaBH_4$ grain as shown in Fig. 42. The temperature in the combustion zone was much higher when aluminum powders was injected because the flame color was much brighter than the hydrogen combustion as shown in Fig. 48.

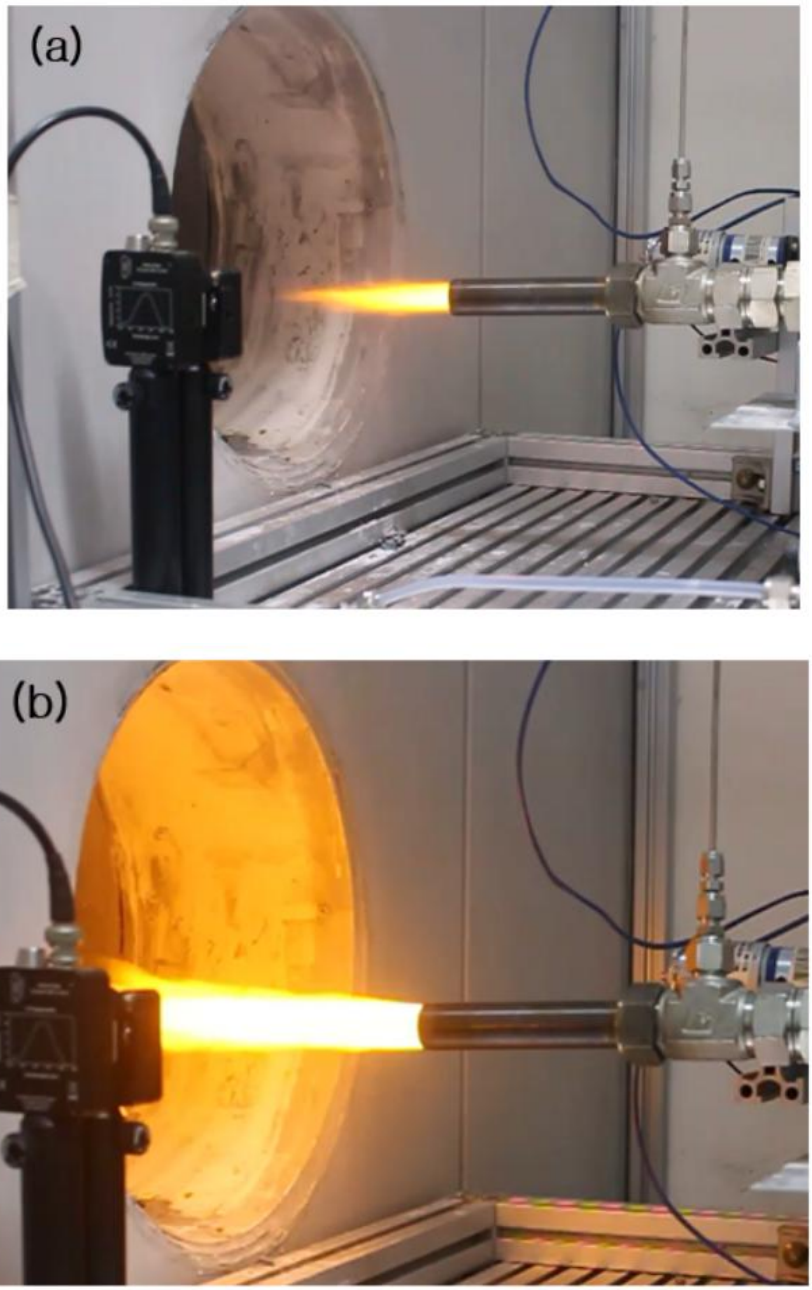

Fig. 48. Pictures of (a) solid $NaBH_4$-based hydrogen combustion and (b) ignition of aluminum powders. The flame color was changed by injecting aluminum powders in the combustion zone.

In addition, it was confirmed that the signal of AlO radicals was detected when the aluminum powders was injected. Consequently, the ignition of aluminum powders was successfully performed by the hydrogen combustor using $NaBH_4$ thermal decomposition.

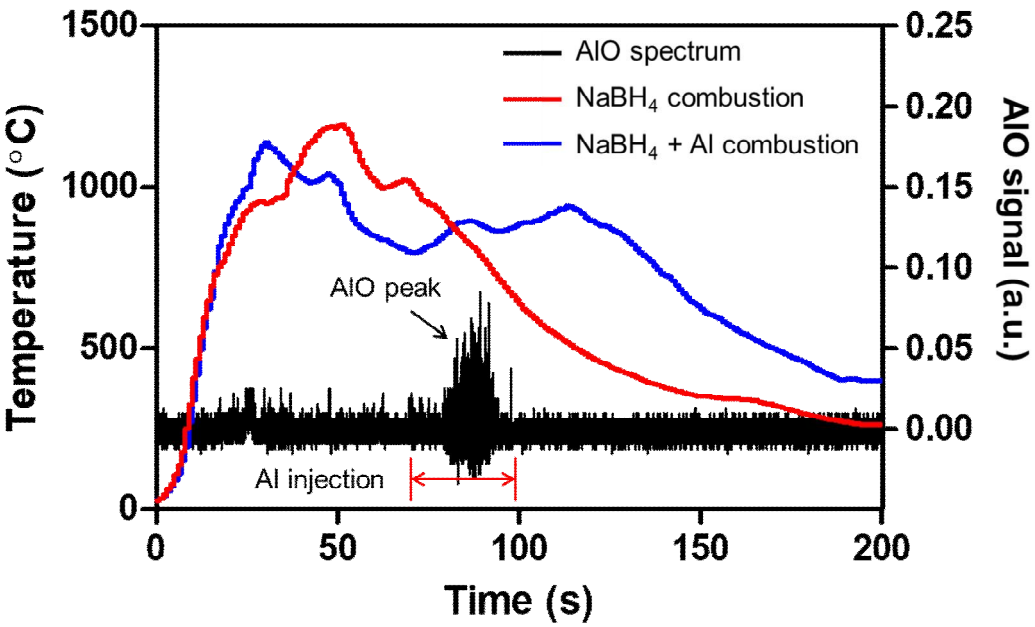

Fig. 49 Temperature change inside the combustion zone with and without the injection of aluminum powders.

Ⅵ Conclusion

The humans, for a long time, had looked forward to analyzing a sample of Mars to understand the chemical make-up and potential life forms that can exist on a planet that is potentially habitable by humans. If the next Mars investigation is performed by the two-way mission, it will enable tremendous scientific discoveries. The next step of Mars exploration has to bring samples to Earth for detailed analysis in sophisticated laboratories. However, to returning the Martian sample, it is required that the propulsion system with a comparatively large velocity change capability due to the relatively deep Martian gravity well. Therefore, a significant amount of propellant will be required but bringing that mass from Earth would be impractical and grossly inefficient. Manufacturing in-situ propellant using the martian resource would be far more practical. In this study, we investigated the utilization of Mars resources for the production of field propulsion agent.

First, we performed the plasma-assisted CO_2 adsorption with CaO using low current under 100 mA for high energy efficiency. The mechanism of the plasma-assisted CO_2 adsorption was investigated by in-situ DRIFTS spectroscopy. We confirmed that the CO_2 band was significantly reduced by up to 28.09% 33.33% at 500℃, after introduced the plasma, which it was improved more than a factor of 3 compared to without plasma. Also, reaction of $Ca(OH)_2$ and CO_2 has occurred at 200℃ in the presence of plasma. The formed water, at this time, led to the formation of $Ca(HCO_3)_2$ reacted with $CaCO_3$ and CO_2. Plasma has enabled to increase of CO_2 adsorption rates by promoting various reactions on the surface of CaO as well as carbonator reaction. Besides, most CO_2 adsorbed on the CaO surface by plasma was desorbed at under 500℃.

Second, to improve the CO_2 conversion and energy efficiency, we have investigated the interaction of CO_2 with the catalyst in the presence of plasma via in-situ DRIFTS spectroscopy. It is observed that the formation of bicarbonate at higher than 200℃ on the surface of Al_2O_3, and conversion to different types of bicarbonate by plasma-excited CO_2. Alumina supported Ce catalyst with metal loadings of 10 wt% has not occurred of the conversion and formation of carbonate because of the large amount of Ce particles occupy a significant fraction of the surface and prevent the formation and conversion of carbonates

on the alumina surface. In addition, we observed the new band attributed to the formate species, confirmed the cerium promoted catalyst can be an enhancement of the formation of intermediate formate species by the plasma-excited CO_2. Notably, these formed intermediate species could be encouraged the generation of CO by the reaction of formate and bicarbonate.

Last, an auto-ignited hydrogen combustor using the $NaBH_4$ thermal decomposition was developed to make it compact and lightweight the ignition system of aluminum powders. The $NaBH_4$ was a superior hydrogen source because of its high hydrogen storage density. In addition, the $NaBH_4$ thermal decomposition was activated at the temperature close to the auto-ignition point of hydrogen. Thus, when the solid $NaBH_4$ grain was heated higher than 500℃, the $NaBH_4$ thermal decomposition was initiated and hydrogen was ignited simultaneously as generated. The ignition system of aluminum powders using the solid $NaBH_4$-based hydrogen combustor combined with the powder injector with the rotating screw. The $NaBH_4$ grain of 30 g was prepared and heated up to 500°C to activate the thermal decomposition only using the electric power of 65 W for 10 sec. As the $NaBH_4$ was decomposed, the hydrogen was generated and immediately auto-ignited. The characteristics of $NaBH_4$ thermal decomposition was dependent on the air supply rate. In the air supply rate of 40 L/min, the thermal decomposition time was 111 sec and the hydrogen generation rate was 20.1 L/min. When the hydrogen combustion was stabilized, aluminum powders were injected by 1.268 g/min into the combustion zone using the powder injector with 5 L/min of air as a carrier gas. The equivalence ratio was 1.158 considering both the generated hydrogen and aluminum powders. Finally, the ignition of aluminum powders was successfully performed by the solid NaBH4-based hydrogen combustor and was validated by using a photodetector equipped with a 486 nm filter for AlO radical detection.

Reference

1. O. L. Vaisberg, The solar wind interaction with Mars: a review of results from previous Soviet missions to Mars, Advances in space research, Vol. 12, No. 9, pp. 137-161, 1992.
2. J.G Trotignon, M Parrot, J.C Cerisier, M Menvielle, W.I Axford, M Paetzold, R warnant, A.W Wernik, The plasma environment of Mars: from the shocked solar wind down to the ionosphere, Planetary and space science, Vol. 48, No. 12-14, pp. 1181-1191, 2000.
3. W. C.Goss, The Mariner spacecraft star sensors, Applied optics, Vol. 9, No. 5, pp. 1056-1067, 1970.
4. “Mars Mariner 4 mission”, retrieved 23 September 2019, from https://www.nasa.gov/image-feature/mariner-4-image-of-mars
5. Leighton, Robert B., Murray, Bruce C., Sharp, Robert P., Denton Allen, J., Sloan, Richard K., Mariner Ⅳ Photography of Mars: initial results, Science, Volume 149, No. 3684, pp. 627-630, 1965
6. “Mars Mariner 6”, retrieved 23 September 2019, from https://mars.nasa.gov/mars-exploration/missions/mariner-6-7
7. Merton E. Davies, Coordinates of features on the mariner 6 and 7 pictures of Mars, Icarus, Vol. 17, No. 1, pp. 116-167, 1972.
8. Deborah S. Bass, Kenneth E. Herkenhoff, David A. Paige, Variability of Mars’ north polar water ice cap: Ⅰ. Analysis of Mariner 9 and Viking orbiter imaging data, Icarus, Vol. 144. No. 2, pp. 382-396, 2000.
9. Chaikin, A. L., Maxwell, T. A., El-Bax, F., Temporal changes in the cerberus region of Mars: Mariner 9 and Viking comparisons, Icarus, Vol. 45m No. 1, pp. 167-178, 1981.
10. Y. Moudden, J. C. McConnell, S. R. Beagley, M. A. Lopez-Valverde, M. Lopez-Puertas, Meteorological results from the global Mars multiscale model at the viking 1 lander site, Advances in Space Research, Vol. 36, No. 11, pp. 2169-2175, 2005.

11. “Mars Viking mission”, retrieved 23 September 2019, from https://nssdc.gsfc.nasa.gov/planetary/viking.html
12. P. withers, M. C. Towner, B. Hathi, J. C. Zarnecki, Analysis of entry accelerometer data: a case study of Mars Pathfinder, Planetary and space science, Vol. 51, No. 9-10, pp. 541-561, 2003.
13. Anthony J. Spear, Low cost approach to Mars Pathfinder, Acta Astronautica, Vol. 37, pp. 131-139, 1995.
14. “Mars pathfinder”, retrieved 23 September 2019, from https://mars.nasa.gov/mars-exploration/missions/pathfinder/
15. P. Withers, M. D. Smith, Atmospheric entry profiles from th Mars exploration rovers Sprit and Opportunity, Icarus, Vol. 185, No. 1, pp. 133-142, 2006.
16. Mariek E. Schmidt, Christian M. Schrader, Timothy J. McCoy, The primary fO2 of basalts examined by the Sprit rover in Gusev Crater, Mars: evidence for multiple redox states in the martian interior, Earth and planetary science letters, Vol. 384, pp. 198-208, 2013.
17. P. Withers, M. D. Smith, Atmospheric entry profiles from th Mars exploration rovers Sprit and Opportunity, Icarus, Vol. 185, No. 1, pp. 133-142, 2006.
18. C.D. Edwards, Jr., B. Arnold, R. Depaula, G. Kazz, C. Lee, G. Noreen, Relay communications strategies for Mars exploration through 2020, Acta astronautica, Vol. 59, No. 1-5, pp. 310, 318, 2006.
19. S.J. VanBommel, R. Gellert, J. A. Berger, A. S. Yen, N. I. Boyd, Mars science laboratory alpha particle x-ray spectrometer trace elements: situational sensitivity to Co, Ni, Cu, Zn, Ga, Ge, and Br, Acta astronautica, Vol. 165, pp. 32-42, 2019.
20. B. L. Jolliff, D. W. Mittlefehldt, W. H. Farrand, A. H. Knoll, S. M. McLennan, R. Gellert, Mars exploration rover Opportunity: water and other volatiles on Ancient Mars, Volatiles in the Martian crust, pp. 285-328, 2019.
21. NewScientist, Time’s up for Mars rover Opportunity, Vol. 241, No. 3218, pp. 12, 2019.
22. T. A. Livengood, T. Kostiuk, T. Hewagama, R. L. Smith, K. E. Fast, J. N. Annen, J. D. Delgado, Evidence for diurnally varying enrichment of heavy oxygen in Mars atmosphere, Icarus, Vol. 335, 113387, 2020.

23. Alexandra Witze, Mars rover detects ‘excitingly huge’ methane spike, Nature, 24 June 2019.
24. “Mars InSight mission”, retrieved 23 September 2019, from https://mars.nasa.gov/insight/
25. S. Reershemius, M. Fittock, T. L. Hudson, K. Sasaki, M. Scharringhausen, T. Spohn, T. Sprowitz, T. Wippermann, Structure development of the HP^3 instrument support system for the Mars mission InSight, Acta astronautica, Vol. 164, pp. 9-22, 2019.
26. M. A. Trinidad, E. Zabrensky, A. Sengupta, Mars ascent vehicle system studies and baseline conceptual design, 2012 IEEE Aerospace conference, Big Sky, MT, USA, March 2012.
27. Adrien J. Boiron and Brian J. Cantwell, Hybrid rocket propulsion and in-situ propellant production for future Mars missions, 49th AIAA/ASME/ SAE/ASEE Joint Propulsion Conference, AIAA2013-3899, San Jose, CA, July 2013.
28. G. Chen, N. Britun, T. Godfroid, M. P. Delplancke-Ogletree and R. Synders, Role of plasma catalysis in the microwave plasma-assisted conversion of CO_2
29. Baozhong Zhu, Fan Li, Yunlan Sun, Qichang Wang, Yuxin Wu, Zicheng Zhu, “The effects of additives on the combustion characteristics of aluminum powder in steam, RCS Advances, Vol. 7, pp. 5725-5732, 2017.
30. W. Yang, W. Shi, C. Chen, T. Zhang, J. Liu, Z. Wang, J. Zhou, “Efficiency analysis of a novel electricity and heat co-generation system in the basis of aluminum-water reaction”, Int. J. Hydrogen Energy, Vol. 42, pp. 3598-3604, 2017.
31. F. Franzoni, M. Milani, L. Montorsi, V. Golovitchev, Combined hydrogen production and power generation from aluminum combustion with water: Analysis of the concept, Int. J. Hydrogen Energy, Vol. 35, pp. 1548-1559, 2010.
32. A. fridman, Plasma chemistry, Cambridge university press, 2008.
33. L. F. Spencer, The study of CO_2 conversion in a microwave plasma/catalyst system, Ph. D. Dissertation, University of Michgan, U.S.A., 2012.
34. S. XU, Plasma-assisted conversion of CO_2, Ph. D. Dissertation, School of chemical engineering and analytical sciences, The university of Manchester, U. K., 2017.

35. I. Adamovich, S. D. Baalrud, A. Bogaerts, P. J. Bruggeman, M. Cappelli, V. Colombo, U. Czarnetzki, U. Ebert, J. G. Eden, P. Favia, D. B. Graves, S. Hamaguchi, G. Hieftje, M. Hori, I. D. Kaganovich, U. Kortshagen, M. J. Kushner, N. J. Mason, S. Mazouffre, S. M. Thagard, H-R. Metelmann, A. Mizuno, E. Moreau, A. B. Murphy, B. A. Niemira, G. S. Oehrlein, Z. Lj Petrovic, L. C. Pitchford, Y-K. Pu, S. Rauf, O. Sakai, S. Samukawa, S. Starikovskaia, J. Tennyson, K. Terashima, M. M. Turner, M. C. M van de Sanden and A. Vardelle, The 2017 plasma roadmap: low temperature plasma science and technology, J. Phys. D: Appl. Phys., Vol. 50, 323001, 2017.
36. B. Ashford, X. Tu, Non-thermal plasma technology for the conversion of CO_2, Current opinion in green and sustainable chemistry, Vol. 3, pp. 45-49, 2017.
37. A. Bogaerts, E. Neyts, R. Gijbels, J.J.A.M. Mullen, van der, Gas discharge plasmas and their applications, Spectrochimica Acta Part B: Atomic Spectroscopy, Vol. 57, No. 4, pp. 609-658, 2002.
38. U. Kogelschatz, Dielectric-barrier discharges: their history, discharge physics, and industrial applications, Plasma chemistry and plasma processing, Vol. 23, Nol. 1, pp. 1-46, 2003.
39. A Fridman, A Chirokov and A Gutsol, Non-thermal atmospheric pressure discharges, Journal of physics D: Applied physics, Vol. 38, No. 2, R1-R24, 2005.
40. C. Tendero, C. Tixier, P. Tristant, J. Desmaison and P. Leprince, Atmospheric pressure plasmas: A review, Spectrochimica Acta Part B: Atomic Spectroscopy, Vol. 61, No. 1, pp. 2-30, 2006.
41. St. Kolev and A. Bogaerts, A 2D model for a gliding arc discharge, Plasma sources science and technology, Vol. 24, No.1, 2015.
42. S. Xu, F. Song. X. Yang, Y. Zhong, Y. Gao, Experimental Study on the Influence of an Extension Tube on the Evolution Process and Characteristic Parameters of a Gliding Arc, Applied sciences, Vol. 9, No. 7, 1347, 2019.
43. A. Risacher, S. Larigaldie, G. Bobillot, J. Marcellin and L. Picard, Active stabilization of low-current arc discharges in atmospheric-pressure air, Plasma sources science and technology, Vol. 16, No. 1, pp. 200-209, 2007.
44. J. R. Roth, Industrial Plasma Engineering vol 1:Principles, CRC Press, 1995.

45. R. Snoeckx, A. Bogaerts, Plasma technology - a novel solution for CO_2 conversion?, Chem. Soc., Vol. 46, 5805, 2017.

46. G. Chen, V. Georgieva, T. Godfroid, R. Snyders, M. Delplancke-Ogletree, Plamsa assisted catalytic decomposition of CO_2, Applied catalysis B: Environmental, Vol. 190, pp. 115-124, 2016.

47. G. Chen, T. Godfroid, N. Britun, V. Georgieva, M. Delplancke-Ogletree, R. Snyders, Plasma-catalytic conversion of CO2 and CO_2/H_2O in a surface-wave sustained microwave discharge, Applied Catalysis B:Environmental, Vol. 214, pp. 114-125, 2017.

48. Y. Qin, G. Niu, X. Wang, D. Luo, Y. Duan, Status of CO_2 conversion using microwave plasma, Journal of CO_2 utilization, Vol. 28, pp. 283-291, 2018.

49. W. Bongers, H. Bouwmeester, B. Wolf, F. Peeters, S. Welzel, D. Bekerom, N. Harder, A. Goede, M. Graswinckel, P. W. Groen, J. Kopecki, M. Leins, G. rooij, A. Schulz, M. Walker, R. Sanden, Plasma-driven dissociation of CO2 for fuel synthesis, Plasma processes and polymers, Vol. 14, No. 6, 1600126, 2017.

50. G. Chen, L. Wang, T. Godfroid, R. Snyders, Progress in Plasma-Assisted Catalysis for Carbon Dioxide Reduction, Plasma Chemistry and Gas Conversion, Nikolay Britun and Tiago Silva, IntechOpen, DOI: 10.5772/intechopen.80798, 2018.

51. L. Li, H. Zhang, X. Li, X. Kong, R. Xu, K. tay, X. Tu, Plasma-assisted CO_2 conversion in a gliding arc discharge: Improving performance by optimizing the reactor design, Journal of CO_2 Utilization, Vol. 29. pp. 269-303, 2019

52. K. V. Laer, A. Bogaerts, Improving the conversion and energy efficiency of carbon dioxide splitting in a zirconia-packed dielectric barrier discharge reactor, Energy technology, Vol. 3, No. 10, pp. 1038-1044, 2015.

53. A. Zhou, D. Chen, C. Ma, F. Yu, B. Dai, DBD plasma-ZrO_2 catalytic decomposition of CO_2 at low temperatures, Catalysts, 2018, 8(7), 256; https://doi.org/10.3390/catal8070256.

54. R. Aerts, W. Somers, A. Bogaerts, Carbon dioxide splitting in a dielectric barrier discharge plasma: A combined experimental and computational study, CHEMSUSCHEM, Vol. 8, No. 4, pp. 702-716, 2015.

55. M. Ramakers, I. Michielsen, R. Aerts, V. Meynen, A. Bogaerts, Effect of argon or helium on the CO_2 conversion in a dielectric barrier discharge, Plasma process and polymers, Vol. 12, No. 8, pp. 755-763, 2015.
56. X. Duan, Z. Hu, Y. Li, B. Wang, Effect of dielectric packing materials on the decomposition of carbon dioxide using DBD micro plasma reactor, American Institute of Chemical Engineers Journal, Vol. 61, No. 3, pp. 898-903, 2015.
57. A. Zhou, D. Chen, C. Ma, F. Yu and B. Dai, DBD plasma-ZrO2 catalytic decomposition of CO2 at low temperatures, Catalysts, Vol. 8(7), 256, 2018.
58. A. Ozkan, A. Bogaerts, F. Reniers, Routes to increase the conversion and the energy efficiency in the splitting of CO_2 by a dielectric barrier discharge, J. phys. D:Appl. Phys., Vol. 50, 084004, 2017.
59. D. Mei, X. Zhu, Y. L. He, J. D. Yan, X. Tu, Plasma-assisted conversion of CO_2 in a dielectric barrier discharge reactor: understanding the effect of packing materials, Plasma sources science and technology, Vol. 24, 015011, 2015.
60. Q. Yu, M. Kong, T. Liu, J. Fei, X. Zheng, Characteristics of the decomposition of CO2 in a dielectric packed-bed plasma reactor, Plasma chemistry and plasma processing, Vol. 32, No. 1, pp. 153-163, 2012.
61. T. Kozak, A. Bogaerts, Evaluation of the energy efficiency of CO_2 conversion inmicrowave discharges using a reaction kinetics model, Plasma sources science and technology, Vol. 24, No. 1, 015024, 2014.
62. W. Bongers, H. Bouwmeester, B. Wolf, F. Peeters, S. Welzel, D. van den Bekerom, N. den Harder, A. Goede, M. Graswinckel, P. W. Groen, J. Kopecki, M. Leins, G. van Rooij, A. Schulz, M. Walker and R. van de Sanden, Plasma-driven dissociation of CO_2 for fuel synthesis, Plasma processes polymers, Vol. 14, No. 6, e1600126, 2017.
63. N. Britun, T. Silva, G. Chen, T. Godfroid, J. Mullen, R. Snyders, Plasma-assisted CO2 conversion: optimizing performance via microwave power modulation, Journal of physics D: Applied physics, Vol. 51, 144002, 2018.
64. D. Czylkowski, B. Hrycak, M. Jasinski, M. Dors, J. Mizeraczyk, Microwave plasma-based method of hydrogen production via combined steam reforming of methane, Energy, Vol. 113, No. 15, pp. 653-661, 2016.

65. G. Chen, V. Georgieva, T. Godfroid, R. Snyders, M.-P. Delplancke-Ogletree, Plasma assisted catalytic decomposition of CO2, Appl. Catal. B-Environ. 190 (2016) 115.124.

66. T. Nunnally, K Gutsol, A. Rabinovich, A. Fridman, A. Gutsol, A. Kemoun, Dissociation of CO2 in a low current gliding arc plasmatron, Journal of physics D: applied physics, Vol. 44, No. 27, 274009, 2011.

67. H. Zhang, L. Li, X. Li, W. Wang, J. Yan, X. Tu, Warm plasma activation of CO2 in a rotating gliding arc discharge reactor, Journal of CO2 utilization, Vol. 27. pp. 472-479, 2018.

68. M. Ramaker, G. Trenchev, S. Heijkers, W. Wang, A. Bogaerts, Gliding arc plasmatron: providing an alternative method for carbon dioxide conversion, CHEMSUSCHEM, Vol. 10, No. 13, pp. 2642-2652, 2017.

69. D. H. Lee, K. T. Kim, M. S. Cha, Y. H. Song, Optimization scheme of a rotating gliding arc reactor for partial oxidation of methane, P. Combustion Institute, Vol. 31, pp. 3343-3351, 2007.

70. W. Wang, D. Mei, X. Tu, A. Bogaerts, Gliding arc plasma for CO_2 conversion: better insights by a combined experimental and modelling approach, Chemical engineering journal, Vol. 330, pp. 11-25, 2017.

71. A. Indarto, D. R. Yang, J. W. Choi, H. Lee, H. K. Song, Gliding arc plasma processing of CO_2 conversion, Journal of hazardous materials, Vol. 146, pp. 309-315, 2007.

72. J. Mohammad, Application of Vibrational Spectroscopy in Organic Electronics, 2017.

73. P. R. Griffiths, J. A. De Haseth, J. D. Winefordner, Fourier transform infrared spectrometry, 2nd edition, Wiley-blackwell, 2007.

74. F. Azzolina-Jury, F. Thibault-starzyk, Mechanism of low pressure plasma-assisted CO_2 hydrogenation over Ni-USY by microsecond time-resolved FTIR spectroscopy, Topics in catalysis, Vol. 60, pp. 1709-1721, 2017.

75. T. T. Belete, M. C. M van de Sanden, M. A. Gleeson, Effect of transition metal dopants on the calcination of $CaCO_3$ under Ar, H_2O and H_2, Journal of CO_2 utilization, Vol. 31, pp. 152-166, 2019.

76. T. T. Belete, Evaluation of (plasma-assisted) decomposition of transition metals doped CaCO3 for CO2 capture and conversion, Ph. D. Dissertation, Eindhoven university of technology, Netherlands, 2019.

77. A. M. Kalinkin, E. V. Kalinkina, O. A. Zalkind, T. I. Makarova, Chemical interaction of calcium oxide and calcium hydroxide with CO2 during mechanical activation, Inorganic materials, Vol. 31, No. 10, pp. 1073-1079, 2005.

78. J. D. Rodriguez-Blanco, S. Shaw, L. G. Benning, The kinetics and mechanisms of amorphous calcium carbonate (ACC) crystallization to calcite, via vaterite, Nanoscale, Vol. 3, pp. 265-271, 2011.

79. A. Roy, J. Bhattacharya, Microwave-assisted synthesis and characterization of CaO nanoparticles, International journal of nanoscience, Vol. 10, No. 3, pp. 413-418, 2011.

80. R. Philipp, Kaoru Fujimoto, FTIR spectroscopic study of CO2 adsorption/desorption on MgO/CaO catalysts, J. Phys. Chem. Vol. 96, pp. 9035, 9038, 1992.

81. K. Fottinger, W. Emhofer, D. Lennon, G. Rupprechter, Adsorption and reaction of CO on (Pd-)Al_2O_3 and (Pd-)ZrO_2: vibrational spectroscopy of carbonate formation, Topics in catalysis, Vol. 60, No. 19-20, pp. 1722-1734, 2017.

82. J. Szanyi, J. H. Kwak, Dissecting the steps of CO_2 reduction: 1. the interaction of CO and CO_2 with ɣ-Al_2O_3: an in situ FTIR study, Phys, Chem. Chem. Phys., Vol. 16, 15117, 2014.

83. W. Gac, W. Zawadzki, M. Rotko, G. Slowik, M. Greluk, CO_2 methanation in the presence of Ce-promoted alumina supported nickel catalysts: H_2S deactivation studies, Topics in catalysis, Vol. 62, pp. 524-534, 2019.

84. P. G. Lustemberg, M. V. Bosco, A. Bonivardi, H. F. Busnengo, M. V. G. Pirovano, Insights into the nature of formate species in the decomposition and reaction of methanol over cerium oxide surfaces: a combined infrared spectroscopy and density functional theory study, The journal of physical chemistry C, Vol. 119, No. 37, pp. 21452-21464, 2015.

85. A. Banerjee, M. W. Kanan, Carbonate-promoted hydrogenation of carbon dioxide to multicarbon carboxylates, ACS central science, Vol. 4, pp. 606-613, 2018.

86. R. H. Frisbee, Mass and power estimates for Mars in-situ propellant production systems, Paper presented at the 23rd AIAA/ASME/SAE/ASEE Joint Propulsion Conference and Exhibit, California, USA, AIAA 87-1900, June 29-July 2, 1987.
87. A. A. Chandler, B. J. Cantwell, G. S. Hubbard, A two-stage, single port hybrid propulsion system for a Mars ascent vechile, 46th AIAA Joint Propulsion Conference and Exhibit, Nashville, TN, U.S.A., AIAA-2010-6635, July 2010.
88. A. A. Chandler, C. Gatto, B. Nakazono, K. Grayson, D. Vaughan, Hybrid propulsion in-situ resource utilization test facility, development, 50th AIAA Joint Propulsion Conference and Exhibit, Cleveland, OH, U.S.A., AIAA-2014-3866, July 2014.
89. E. Jens, B. J. Cantwell, G. S. Hubbard, Hybrid rocket propulsion systems for outer planet exploration missions, Acta astronautica, Vol. 128, pp. 119-130, 2016.
90. G. A. Landis, S. R. Oleson, T. W. Packard, D. L. Linne, J. M. Woytach, M. C. Martini, J. Fittje, J. Gyekenyesi, A. J. Colozza, J. Fincannon, K. M. Bury, H. Dominguez, R. Jones, D. Smith, S. G. Miller, D. Vento, Design study of a Mars ascent vehicle for sample return using in-situ generated propellant, 10th Symposium on space resource utilization, Grapevine, Texas, U.S.A., AIAA-2017-0424, January 2017.
91. A. Okninski, On use of hybrid rocket propulsion for suborbital vehicles, Acta astronautica, Vol. 145, pp. 1-10, 2018.
92. Timothy F. Miller, Jeremy L. Walter, Daniel H. Kiely, A Next-Generation AUV Energy System Based on Aluminum-seawater Combustion, Proceeding of the 2002 Workshop on Autonomous Underwater Vehicles, June 2002.
93. LiYa Huang, ZhiXun Xia, JianXin Hu, QianWen Zhe, Performance study of a water ramjet engine, Science China Technological Sciences, Vo. 54, pp. 877-882, 2011.
94. Gabriel D. Roy, Advances in Chemical Propulsion: Science to Technology, CRC Press, 2001.
95. G.A. Risha, S.F. Son, R.A. Yetter, V. Yang, B.C. Tappan, Combustion of nano-aluminum and liquid water, Proceedings of the Combustion Institute, Vol. 31, pp. 2029-2036, 2007.

96. F. Franzoni, M. Milani, L. Montorsi, V. Golovitchev, Combined hydrogen production and power generation from aluminum combustion with water: Analysis of the concept, Int. J. Hydrogen Energy, Vol. 35, pp. 1548-1559, 2010.

97. Baozhong Zhu, Fan Li, Yunlan Sun, Qichang Wang, Yuxin Wu, Zicheng Zhu, The effects of additives on the combustion characteristics of aluminum powder in steam, RCS Advances, Vol. 7, pp. 5725-5732, 2017.

98. W. Yang, W. Shi, C. Chen, T. Zhang, J. Liu, Z. Wang, J. Zhou, Efficiency analysis of a novel electricity and heat co-generation system in the basis of aluminum-water reaction, Int. J. Hydrogen Energy, Vol. 42, pp. 3598-3604, 2017.

99. Amy Corcoran, Stefano Mercati, Hongqi Nie, Massimo Milani, Luca Montorsi, Edward L. Dreizin, Combustion of fine aluminum and magnesium powders in water, Combustion and flame, Vol. 160, pp. 2242-2250, 2013.

100. I. Glassman, Metal combustion processes, American rocket society preprint, 938-59, New York, 1959.

101. Fan Li, Baozhong Zhu, Yunlan Sun, Wei Tao, Hydrogen generation by means of the combustion of aluminum powder/sodium borohydride in steam, Int. J. of Hydrogen Energy, Vol. 42, pp. 3804-3812, 2017.

102. S. Lee, K. Noh, W. Yoon, Experimental studies on the ignition characteristics of nickel-coated aluminum powder with size distribution and oxidizer conditions, Journal of the Korean Society of Propulsion Engineers, pp. 250-255, 2015.

103. Timothy F. Miller, John D. Herr, Green rocket propulsion by reaction of Al and Mg powders and water, 40th AIAA Joint Propulsion Conference and Exhibit, Fort Lauderdale, Florida, U.S.A., AIAA2004-4037, July 2004.

104. M. B. Sun, C. Gong, S. P. Zhang, J. H. Liang, W. D. Liu, Z. G. Wang, Spark ignition process in a scramjet combustor fueled by hydrogen and equipped with multi-cavities at Mach 4 flight condition, Experimental Thermal and Fluid Science, Vol. 43, pp. 90-96, 2012.

105. B. Hardy, D. Tamburello, C. Corgnale, Hydrogen storage adsorbent systems acceptability envelope, Int. J. Hydrogen Energy, Vol. 43, pp. 19525-19539, 2018.

106. A. Nakano, Te. Maeda, H. Ito, M. Masuda, Y. Kawakami, M. Tange, T. Takahashi, K. Nishida, Study on absorption/desorption characteristics of a metal

hydride tank for boil-off gas from liquid hydrogen, Int. J. Hydrogen Energy, Vol. 37, pp. 5056-5062, 2012.

107. Ju-hyeong Sim, Taegyu Kim, Accelerated hydrolysis of solid-state $NaBH_4$ by injecting NaHCO3 solution for hydrogen generation, Applied Energy, Vol. 160, pp. 999-1006, 2015.
108. M. Bhouri, M. Linder, I. Burger, Metal hydride reactor for dual use: Hydrogen storage and cold production, Int. J. Hydrogen Energy, Vol. 43, pp. 23357-23371, 2018.
109. J. Kim, T. Kim, Compact PEM fuel cell system combined with all-in-one hydrogen generator using chemical hydride as a hydrogen source," Applied energy, Vol. 160, pp. 945-953, 2015.
110. Pascal Martelli, Riccarda Caputo, Arndt Remhof, Philippe Mauron, Andreas Borgschulte, Andreas Zuttel, Stability and Decomposition of $NaBH_4$, The Journal of Physical Chemistry C, Vol. 114, pp. 7173-7177, 2010.
111. FKK Corporation, FKK PH catalog, 2018
112. C. J. Lee, T. Kim, Hydrogen supply system employing direct decomposition of solid-state NaBH4, Int. J. Hydrogen, Vol. 40(5), pp. 2274-82, 2015.
113. J.C. Melcher, R. L. Burton and H. Krier, Combustion of aluminum particles in solid rocket motor flows, 35th AIAA Joint Propulsion Conference and Exhibit, Los Angeles, California, U.S.A., AIAA-99-2630, June 1999.